Pontifícia Universidade Católica
do Rio de Janeiro

Karen Stephanie Ninanya de la Cruz

Numerical implementation of an elasto-viscoplastic constitutive model for prediction of the mechanical behavior of rock salt

Dissertação de Mestrado

Dissertation presented to the Programa de Pós–graduação em Engenharia Civil of PUC-Rio in partial fulfillment of the requirements for the degree of Mestre em Engenharia Civil.

Advisor: Prof. Celso Romanel

Rio de Janeiro
July 2020

Pontifícia Universidade Católica
do Rio de Janeiro

Karen Stephanie Ninanya de la Cruz

Numerical implementation of an elasto-viscoplastic constitutive model for prediction of the mechanical behavior of rock salt

Dissertation presented to the Programa de Pós–graduação em Engenharia Civil of PUC-Rio in partial fulfillment of the requirements for the degree of Mestre em Engenharia Civil. Approved by the Examination Committee.

Prof. Celso Romanel
Advisor
Departamento de Engenharia Civil e Ambiental – PUC-Rio

Profa. Christianne de Lyra Nogueira
Departamento de Engenharia de Minas – UFOP

Profa. Deane Mesquita Roehl
Departamento de Engenharia Civil e Ambiental – PUC-Rio

Rio de Janeiro, July 31st, 2020

Karen Stephanie Ninanya de la Cruz

Majored in Civil Engineering by the Ricardo Palma University (Lima, Peru) in 2016.

Bibliographic data

Ninanya de la Cruz, Karen Stephanie

Numerical implementation of an elasto-viscoplastic constitutive model for prediction of the mechanical behavior of rock salt / Karen Stephanie Ninanya de la Cruz; advisor: Celso Romanel.– Rio de Janeiro: PUC-Rio, Departamento de Engenharia Civil e Ambiental, 2020.

96 f: il.; 29,7 cm

Dissertação (mestrado) - Pontifícia Universidade Católica do Rio de Janeiro, Departamento de Engenharia Civil e Ambiental.

Inclui bibliografia

1. Engenharia Civil – Teses. 2. Rock salt; 3. Creep; 4. Elasto-viscoplastic model. I. Romanel, Celso. II. Pontifícia Universidade Católica do Rio de Janeiro. Departamento de Engenharia Civil e Ambiental. III. Título.

CDD: 624

To my parents, for their support
and encouragement.

Acknowledgments

I would like to first thank my advisor, Prof. Celso Romanel, for his support and orientation during the elaboration of this dissertation.

Then I wish to thank my parents, for their love and for encouraging me to reach my goals;

My brother David, for his guidance and support in each challenge I had;

My brother Anthony, for making me a better person;

Jackeline, her friendship and help throughout this master's program;

Juan, for always caring about me;

The FAPERJ, for the financial support;

The professors of the department of Civil Engineering at PUC-Rio, for their commitment and the lessons taught;

This study was financed in part by the Coordenação de Aperfeiçoamento de Pessoal de Nível Superior - Brasil (CAPES) - Finance Code 001

Abstract

Ninanya De la Cruz, Karen Stephanie; Romanel, Celso (Advisor). **Numerical implementation of an elasto-viscoplastic constitutive model for prediction of the mechanical behavior of rock salt**. Rio de Janeiro, 2020. 96p. Dissertação de Mestrado – Departamento de Engenharia Civil e Ambiental, Pontifícia Universidade Católica do Rio de Janeiro.

Since oil exploration is reaching several kilometers below seafloor, an adequate numerical simulation for prediction of rock behavior prior to drilling is becoming increasingly important for the oil industry due to the high operating costs to ensure well stability. One of the typical problems that oil engineers face is the instability of wells in evaporitic rocks, which are often subject to excessive deformation and have time-dependent mechanical behavior characteristics. Huge oil reserves that were found around the world in evaporitic reservoirs encouraged engineers to further investigate this mechanical time-dependent response (creep). On the other hand, the concentration of stresses around the well can make it an unviable engineering project. Destabilization due to large deformations may be involved, leading to problems such as collapse and well closure. Thus, in order to study the stability of the boreholes and design an appropriate oil production system, creep must be properly considered in the expected behavior of the material. In this research, the equations that define the elasto-viscoplastic model of Sterpi and Gioda (2007) will be implemented in the computer program FLAC 3D - Itasca, code based on the finite difference method. The implementation procedure consists of generating a Dynamic Link Library (DLL) written in C++ programming language and integrating the stress along a strain increment by using an explicit integration algorithm. The elasto-viscoplastic model has been validated with experimental results from triaxial creep tests in salt rocks available in the literature, indicating a successful implementation. Finally, a numerical simulation in FLAC 3D considering the model of Sterpi and Gioda is performed in order to study a pre-salt wellbore closure.

Keywords

Rock salt; creep; elasto-viscoplastic model.

Resumo

Ninanya de la Cruz, Karen Stephanie; Romanel, Celso. **Implementação numérica de um modelo constitutivo elasto-viscoplástico para previsão do comportamento mecânico de sal**. Rio de Janeiro, 2020. 96p. Dissertação de Mestrado – Departamento de Engenharia Civil e Ambiental, Pontifícia Universidade Católica do Rio de Janeiro.

Sendo a exploração de petróleo cada vez mais profunda, atingindo vários quilômetros abaixo dos leitos marítimos, uma simulação numérica adequada para prever o comportamento de rochas antes da perfuração está se tornando cada vez mais importante para a indústria de petróleo, devido aos altos custos operacionais para garantir a estabilidade do poço. Um dos problemas típicos que os engenheiros de petróleo enfrentam é a instabilidade de poços em rochas evaporíticas, que geralmente são sujeitas a deformações excessivas e possuem características de comportamento mecânico dependentes do tempo. Grandes reservas de petróleo que foram encontradas ao redor do mundo em rochas evaporíticas encorajaram aos engenheiros a investigar mais profundamente essa resposta mecânica dependente do tempo (*creep*). Por outro lado, a concentração de tensões em torno dos furos pode torná-lo um projeto de engenharia inviável. A desestabilização devido a grandes deformações pode levar a problemas como colapso e fechamento do poço. Assim, para estudar a estabilidade de poços e projetar um sistema de produção de petróleo adequado, a influência do *creep* deve ser considerada adequadamente no comportamento esperado do material. Nesta pesquisa, as equações que definem o modelo elásto-viscoplástico de Sterpi e Gioda (2007) são implementadas no programa computacional FLAC 3D - ITASCA, código baseado no método das diferenças finitas. O procedimento de implementação consiste em gerar uma DLL (*Dynamic Link Library*) escrita em linguagem de programação C++ e integrar as tensões ao longo de um incremento de deformações usando um algoritmo de integração explícito. O modelo elásto-viscoplástico foi validado com resultados experimentais envolvendo rochas salinas disponíveis na literatura. Finalmente, é realizada uma simulação numérica com o programa FLAC 3D, considerando o modelo de Sterpi e Gioda, com o objetivo de estudar o fechamento de um poço no pré-sal brasileiro.

Palavras-chave

Sal; fluência; modelo elasto-viscoplástico.

Table of Contents

List of Figures

List of Tables

List of Simbols

a	variable related to the elasto-viscoelastic model
A	variable related to the viscoelastic model
b	variable related to the elasto-viscoelastic model
B	variable related to the viscoelastic model
B^e	Elastic bulk moduli
C	constant related to the dislocation glide
C^{vp}	viscoplastic cohesion
D_s	self-diffusion coefficient
D_v	diffusion coefficient
$\dot{e}_{IJ}^c$	deviatoric creep strain rate tensor
e_{ij}	deviatoric strain tensor
$\dot{e}_{IJ}^K$	deviatoric kelvin strain rate tensor
$\bar{e}_{ij}^K$	average deviatoric kelvin strain tensor
$e_{ij}^{K,N}$	new deviatoric kelvin strain tensor
$e_{ij}^{K,O}$	old deviatoric kelvin strain tensor
$\dot{e}_{ij}^{vpd}$	deviatoric viscoplastic strain rate tensor of the viscoplastic dashpot
$\dot{e}_{IJ}^{vp}$	deviatoric viscoplastic strain rate tensor
f	yield function
F	constant related to the dislocation glide
F^{vp}	viscoplastic yield function
g	potential function
G^e	elastic shear moduli
G^K	Kelvin shear modulus
G^M	Maxwell shear modulus
J_p	first limit of the second invariant of the deviatoric creep strain
J_r	second limit of the second invariant of the deviatoric creep strain
J_2^{cr}	second invariant of the deviatoric creep strain
J_2^{evp}	second invariant of the deviatoric viscoplastic strain
k	Boltzmann's coefficient
L_k	grain diameter
n	constant related to the dislocation climb

P_1	constant related to the Burger's model
P_2	constant related to the Burger's model
q_1	constant related to the Burger's model
q_2	constant related to the Burger's model
Q_{eff}	effective activated energy
Q^{vp}	viscoplastic potential function
r_1	constant related to the Burger's model
r_2	constant related to the Burger's model
R	universal gas constant
S_{ij}	deviatoric stress tensor
$\dot{S}_{ij}$	deviatoric stress rate tensor
S_{ij}	deviatoric stress tensor
$\bar{S}_{ij}$	average deviatoric stress tensor
S_{ij}^N	new deviatoric stress tensor
S_{ij}^O	old deviatoric stress tensor
S_{IJ}^{vpd}	deviatoric viscoplastic stress rate tensor carried by the viscoplastic dashpot
T	temperature
v_p	P-wave velocity
v_s	S-wave velocity
W	constant related to the dislocation climb
Z	constant related to the Burger's model
δ_{ij}	kronecker's delta
$\triangle e_{ij}^K$	deviatoric kelvin strain variation tensor
$\triangle t$	timestep
$\triangle e_{ij}^{vp}$	deviatoric viscoplastic strain variation tensor
$\triangle e_{ij}$	deviatoric strain variation tensor
η^K	Kelvin viscosity coefficient
η^M	Maxwell viscosity coefficient
$\dot{\lambda}$	viscoplastic multiplier
ϕ^{vp}	viscoplastic friction angle
ψ^{vp}	viscoplastic dilation angle
Ω	atomic volume

ρ	density
σ_{eq}	deviatoric stress
σ'_{ij}	effective stress
σ_m	hydrostatic stress tensor
$\dot{\sigma}_m$	hydrostatic stress rate tensor
$\sigma_i^{vp} j$	viscoplastic stress tensor
σ_1^{vp}	major principal viscoplastic stress
σ_3^{vp}	minor principal viscoplastic stress
ε	total strain
ε^e	instantaneous elastic strain
$\dot{\varepsilon}_{ij}^e$	elastic strain rate
ε_{ij}^p	plastic strain
$\dot{\varepsilon}_{ij}$	total strain rate
$\dot{\varepsilon}_s$	stationary strain creep rate
ε^K	kelvin strain
ε_{vol}	volumetric strain
ε_{ij}^{vp}	viscoplastic strain
$\dot{\varepsilon}_{ij}^{vp}$	viscoplastic strain rate
ε_1	axial strain
ε_3	lateral strain

1 Introduction

1.1 Background

The study of mechanical properties of evaporitic rocks has been given a high priority in oil industry in the last years. The sealing properties regarding low porosity and permeability in comparison with other geomaterials, and large deformation absorption potential without fracturing have turned evaporites into object of broad investments in research due to their capacity as a repository for hydrocarbons.

Exploration of these sources makes industries invest in the development of techniques and methodologies that guarantee stability when drilling offshore basins which involve the presence of evaporitic rocks at several depths. Furthermore, offshore drilling is an expensive and complex oil exploration activity that requires of a study before starting drilling operations. Huge economic losses, expensive loss of time and even the borehole collapse can be serious consequences of wellbore instability.

The occurrence of large salt deposits develops all over the world, especially the Golf of Mexico, the sedimentary basins in the coastal areas of the South Atlantic in Brazil and Africa (Gravina, 1997 (1)). In a Brazilian context, offshore basins such as Santos and Campos account with the presence of thick evaporitic rock layers and are some of the most significant and explored in the last decades.

Evaporitic rock deformation presents a dependence with time behavior known as creep. This subject is a challenge for researches that look for an appropriate constitutive model capable of describing such relation in order to predict rock salt behavior which might be started within minutes of excavating and even last up to several years. A basic task in mathematical description of time-dependent deformation of a certain material is to define deformations as a function of time, stress and temperature (Tomanovic, 2006 (2)). Nevertheless, since the change in temperature for fundamental needs when building most rock structures and underground openings is limited, the effect of temperature in rock mechanics is often neglected (Fahimifar et al., 2015 (3)).

1.2 Previous works

Along the last years, several works related to the implementation of constitutive models and their applicability to geomechanical underground problems associated to the time dependent behavior of rock salt have been developed at the Pontifical Catholic University of Rio de Janeiro. Among the authors of these investigations, Botelho, 2008 (4), Poiate, 2012 (5) and Firme, 2013 (6) are summarized below.

The first work to mention is from Botelho, 2008 (4). His investigation studies the mechanical behavior of rock salt in wellbores. Through a finite element numerical analysis (plane strain and axisymmetric analysis), this thesis study displacements, strains and stresses developed on the wellbore face of different possible scenarios. Finally, this study concludes that the higher the mud weight is, the lower displacements and deformations will be due to the fact that a lower difference between horizontal stresses in situ and pressure on the wall will exist.

Another great contribution was provided by Poiate, 2012 (5). His investigation focused in the study and comprehension of rock salt such as halite, carnallite, anhydrite and tachyhydrite and elaboration of a parametric study through numerical simulation of wellbores in rock salt formations in a finite element code. In addition, this work provides methodologies for numerical simulation of wellbores located in rock salt areas (wellbore perforation, construction and operation).

On the other hand, Firme, 2013 (6) studied three different constitutive models (Power law, Double-mechanism and Multi-mechanism model), which include creep response, for salt rock through geomechanical simulations in a software based on the finite element method. Since two of the constitutive models investigated were not available in the used software, Firme, 2013 (6) implemented them by generating subroutines. Furthermore, it was simulated typical geomechanical situations that involve salt rock by use of these three constitutive models declared above. This work emphasizes the capacity of the Multi-mechanism model in providing accuracy results when reproducing triaxial creep test and simulating a wellbore closure.

1.3 Motivation and objectives

In an attempt to perform a successful drilling project in evaporitic rock layers, it is of highly importance to conduct a previous numerical prediction of the structural behavior of the well during the drilling of rock salt employing an adequate and reliable constitutive model. Furthermore, due to the limited information of geomechanical properties of evaporitic rocks and even constitutive models capable of predicting their creep behavior, the implementation of an elasto-viscoplastic model in a computational program is an enormous contribution to the oil industry. In that regard, the main objective of this dissertation is to describe the gradual evolution of wellbore closure over time employing an elasto-viscoplastic model with the potential of describing not only the primary and secondary creep stage, but also the tertiary and even instantaneous response of evaporitic rocks.

As a first specific objective, this research aims to implement an elasto-viscoplastic model in the finite different code FLAC 3D by generating a Dynamic Link Library (DLL) written in C++ programming language and integrating the stress along a strain increment by using an explicit integration algorithm. Secondly, the validation of the implemented model is conducted through a comparison between numerical results obtained by use of the model in a software based on the finite element method and the obtained in this research (FLAC 3D). Thirdly, this

project seeks to determine and calibrate parameters associated to the elasto-viscoplastic model for the halite rock and reproduce triaxial creep tests presented in the literature. Finally, in this research it is analyzed the evolution of deformations on rock salt layers when performing a single and multistage drilling procedure.

1.4 Layout of the dissertation

This dissertation covers six chapters based on the incremental work achieved. The content in chapter one describes the introduction to the dissertation including research motivation, objectives achieved and thesis outline.

The second chapter comprehends the appropriate theoretical background and literature review of evaporitic rock for a better understanding of this research. Description and importance of the physical properties of salt rocks are mentioned as well as the description of wellbores in evaporitic rock formations.

The third chapter describes the time-dependent theoretical models such as empirical, rheological and the elasto-viscoplastic model that have been developed over time.

The fourth chapter comprises the elasto-viscoplastic model description, its incremental formulation and the implementation procedure that includes the numerical integration algorithm to be implemented in FLAC 3D.

The fifth chapter consists on the validation of the implemented elasto-viscoplastic model through the comparison of two groups of experimental results available in the literature with computed results. The first validation is based on an uniaxial creep test on schist rock and the second one comprises the parameters calculation and calibration for halite rock based on triaxial creep test results.

The sixth chapter presents a tunneling problem in which deformations around the excavation are evaluated and compared with results provided in the literature. Furthermore, it is discussed the numerical analysis evolution of a pre-salt wellbore closure in a pure halite layer with time by use of the elasto-viscoplastic model implemented in FLAC 3D considering a single and multistage of drilling procedure.

The last chapter states the conclusions by specifying a brief summary of the major findings and accomplishments attained in this thesis and some suggestions for future work.

2 Literature Review

2.1 Introduction

The study of evaporitic rocks behavior has became a priority for oil industry because of their capacity as a repository for hydrocarbons in an environment that lacks oxygen. The challenge relies on the creep response of evaporite when performing operational phases in opening such as galleries and boreholes at several depths. The deeper the repository is found, the earlier and more intense the troubles caused by salt creep will be evident (Gravina, 1997 (1)). Therefore, it is of great importance to determine the creep behavior with sufficient accuracy in order to provide reliable calculations, especially in soft rocks (Hunsche and Hampel, 1999 (7)).

Evaporite basins always favor the formation and preservation of hydrocarbons on large scale. Due to this fact, most crude oil reserves in carbonates are covered by evaporite (Weeks, 1958 (8)).

2.2 Evaporitic rocks

Evaporites are sedimentary rocks most known as rock salts, which are formed by evaporation of water in areas of a high concentration solution of salt. Calcite, gypsum, anhydrite, halite, sylvite, carnallite, polyhalite, kainite and kieserite are some of the rock salts variation found around the world; nevertheless the most common evaporitic rock is halite.

2.2.1 Micro-structure of rock salts

Natural rock salt is a polycrystalline material in which each crystal grain of salt is made of several smaller parts known as sub-grains (Hunsche and Hampel, 1999 (7)). The grain size may range from less than 1 mm to several dm and be connected to each other via grain boundaries (i.e. high-angle boundaries) while the sub-grains are distinguished from each other by sub-grain boundaries (i.e. low angle boundaries) (Khaledi, 2018 (9)).

Rock salt mechanical properties are influenced by imperfections or disturbance in the regular arrangement of their atoms known as lattice. Depending on their dimensions, these lattice defects can be classified into point (0-dimensional), line (1-dimensional), planar (2-dimensional), and bulk (3-dimensional) defects (Fig. 2.1).

Point defects do not have spatial extension in any dimension and are referred to the lack or existence of atoms around a single lattice structure whereas in line defects, edge and screw dislocations are their basic types caused by the one dimensional disruptions of the lattice symmetry over lattice planes in one direction. Moreover, planar defects take place in two spatial directions over lattice planes of the rock salt. Grain boundaries and external surfaces are examples of planar defects. Regarding bulk defects, pores and micro-cracks are involved with this imperfection as a result of a three dimensional disorder in the lattice volume.

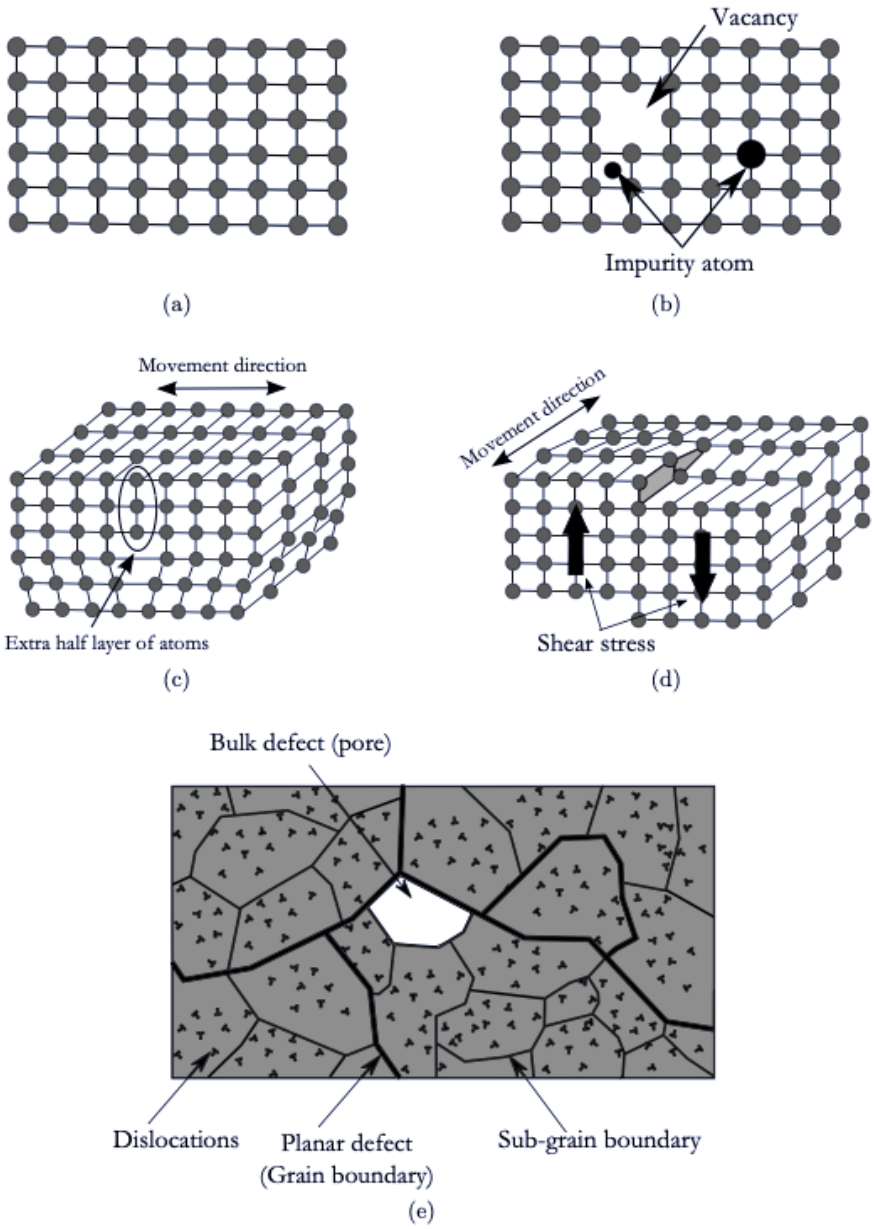

Figure 2.1: Schematic representation of (a) ideal crystal; (b) point defects; (c) linear defect, edge dislocation; (d) linear defect, screw dislocation; (e) planar defect (e.g. grain boundary) and bulk defect (e.g pores) (Khaledi, 2018 (9)).

2.2.1.1 Deformation map

Creep mechanism of evaporitic rocks are present once stress and temperature are imposed on rock salts and can be represented through a deformation map that relates normalized shear stress and homologous temperature. Deformation maps for creep mechanism of rock salt have been based on experimental observations and introduced by researches over the years to describe the deformation of rock salt at a micromechanics level. The first contribution was carried out by Heard, 1972 (10), presenting a deformation map for halite rock.

In fig. 2.2, it is illustrated the deformation-mechanism map for natural rock salt from the Waste Isolation Pilot Plant (WIPP) site located in New Mexico

constructed by Munson, 1979 (11) through the use of theoretical and experimental results. The five relevant mechanisms identified are: defect-less flow, dislocation glide, dislocation climb creep, diffusional creep and an undefined mechanism, which mainly differs in the factor that controls steady state creep (level of stress and temperature).

2.2.1.2 Dislocation Glide

Dislocation glide effect is present when rock salt is subjected to a high stress level and low temperature. The deformation is a consequence of the dislocation in which crystal grains block each other increasing the hardening and strength as well as the dislocation density (Jeremic, 1994 (12)).

Jeremic, 1994 (12) presents a general deformation law developed by several authors that confirms its validity for a temperature between 23 °C and 400 °C according to their experimental investigations.

$$\dot{\varepsilon}_s = C \times exp\left(\frac{-Q_{eff}T}{R}\right) sinh(F\sigma) \tag{2-1}$$

where $\dot{\varepsilon}_s$ is the stationary strain creep rate, C and F are constants, Q_{eff} is the effective activated energy, R is the universal gas constant, T is temperature and σ is the stress.

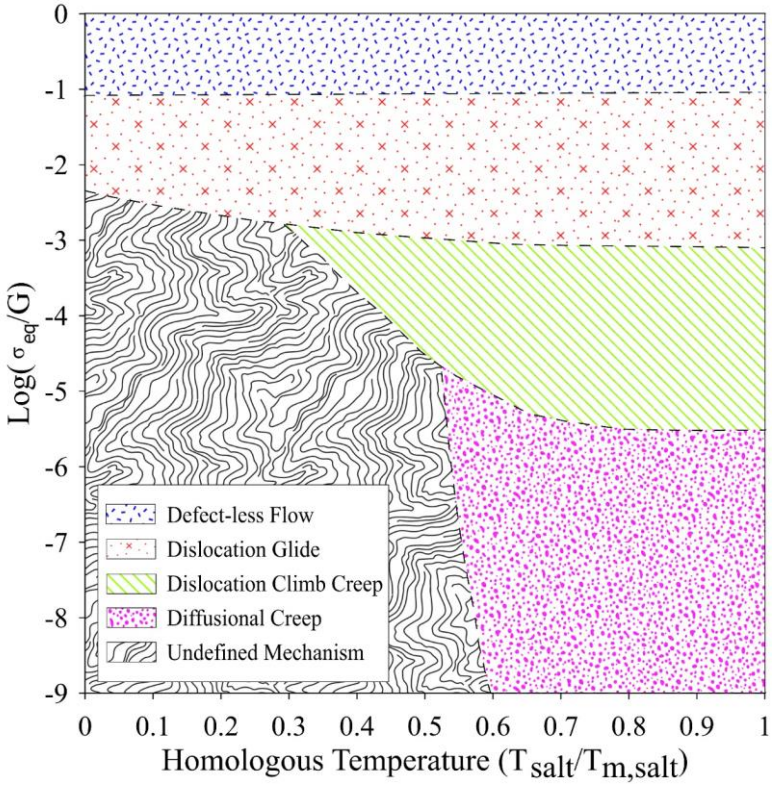

Figure 2.2: Munson's mechanism map, adapted from Munson, 1979 (11).

2.2.1.3 Dislocation Climb

Dislocation climb or polygonization is an important mechanism of deformation that takes places when the dislocation glide area has a contant temperature and stresses below 16 MPa. This mechanism aligns dislocation

themselves and forms small angle grain boundaries arising subgrains with little or no tendency to deform or change in size during secondary creep (Jeremic, 1994 (12)). A dynamic equilibrium between the formation and destruction of subgrain boundaries is reached at secondary creep stage after the adjustment of the stationary subgrain density or the stationary average dislocation density that occurs at the primary creep stage.

According to Jeremic, 1994 (12), authors suggest that dislocation climb is not affected by a temperature below 100 °C.

$$\dot{\varepsilon}_s = W \times exp\left(\frac{Q_{eff}T}{R}\right)\sigma^n \tag{2-2}$$

where W and n are constants. Besides, n values are between 4 and 7.

2.2.1.4 Diffusion Creep

Diffusion creep occurs by the decrease of temperature and deformation rate. Experimental investigations data shows that diffusion creep dominates for stress values between 0.1 and 0.5 MPa (Jeremic, 1994 (12)).

The empiric law of Nabarro-Hering creep ($apud$ Jeremic, 1994 (12)) regards a diffusion creep which is presented in the following equation assumes transport and deposition of atoms in the free space of the single crystal or crystal boundaries.

$$\dot{\varepsilon} = \left(\frac{D_s\Omega\sigma T}{k}\right)L_k^{-2} \tag{2-3}$$

where D_s is the self-diffusion coefficient, Ω is the atomic volume, k is the Boltzmann's coefficient and L_k is the grain diameter.

2.2.1.5 Grain Boundaries Glide

For average grain diameters larger than average distance traveled by dislocations, deformation in the process of dislocation creep and polygonization are not affected by grain boundaries. During poligonization the conditions are satisfied when the grain diameter is larger than the subgrain diameter of up to 0.3 mm; therefore, natural rock salt fulfill this requirement since it usually presents a grain diameter of about 1 cm (Jeremic, 1994 (12)).

The deformation law for grain boundaries glide takes place under small grains and stresses and is similar to the diffusion creep at elevated temperatures.

$$\dot{\varepsilon} = D_v\left(\frac{\sigma}{L_k}\right) \tag{2-4}$$

where D_v is the diffusion coefficient.

2.2.2 Macroscopic behavior of rock salt

Rock salt behavior is subject of research in the last decades since it plays an important role in oil industry. Researchers have focused mainly on the observation and interpretation of rock salt response under different thermo-mechanical

conditions.

2.2.2.1 Elastic behavior

Over the year rock salt has been treated as an isotropic material; for instance, Wawersik et al., 1980 (13) performed a hydrostatic test in order to study the isotropic behavior of rock salt, which resulted in a volumetric strain equal to 3 times the axial and the lateral strains ($\varepsilon_{vol} = 3\varepsilon_1 = 3\varepsilon_3$). The conclusion of the computed results regarding axial and lateral strains indicates that the rock salt is mechanically isotropic prior to testing; therefore, the instantaneous elastic and reversible response can be described by the Hooke's law.

The elastic parameters, shear (G^e) and bulk (B^e) moduli can be determined through a dynamic or static method. The static method involves the calculation of the elastic parameters and their variations through the slopes of the stress-strain curves during unloading/reloading cycles. In concordance with the dynamic method, the measured travel time of the longitudinal P-wave and the transverse S-wave propagating through the rock salt sample define the elastic parameters by using the following equations (Matei and Cristescu, 2000 (14)):

$$B^e = \rho\left(v_p^2 - \frac{4}{3}v_s^2\right) \tag{2-5}$$

$$G^e = \rho v_s^2 \tag{2-6}$$

where ρ is the salt density; v_p and v_s denote the velocity of the P- and S-waves, respectively.

According to Matei and Cristescu, 2000 (14) static and dynamic methods do not necessary provide the same values for the elastic parameters. Generally, the advantages of dynamic methods over static methods regarding elastic parameters estimation on rocks can be summarized in the following aspects: relatively lower cost, faster execution speed, non-destructive nature of the methodology and less geometric requirements in sample preparation. Regarding dynamic test disadvantages, the following aspects can be mentioned: dynamic tests do not directly provide the elastic parameters of the materials as they are used in stress and deformation studies, the permanent record of the test is not easily obtained, requires great theoretical knowledge and experience on the part of the laboratory technician.

On the other hand, independent relation between the elastic parameters and the confining pressure has been reported by Hansen et al., 1984 (15) and Höfer and Thoma, 1968 (16) when obtaining results from reloading/unloading cycles in the stress-strain curves; nevertheless, this dependency is a subject which requires additional further research. Furthermore, the influence of temperature and pressure in elastic parameters was also studied. Whereas Wawersik et al., 1980 (16) reported that the pressure and the temperature do not alter the shear and bulk moduli, Sriapai et al., 2012 (17) concluded that elastic parameters decrease linearly with increasing temperature.

2.2.2.2 Long-term behavior in creep test

A time-dependent deformation most known as "creep" is described by rock salt samples once they are subjected to a constant load. In Fig. 2.3, it is shown the typical axial strain and axial strain rate development for rock salt during a creep test. It is also observed the three creep phases that rock salt experiment in a long-term.

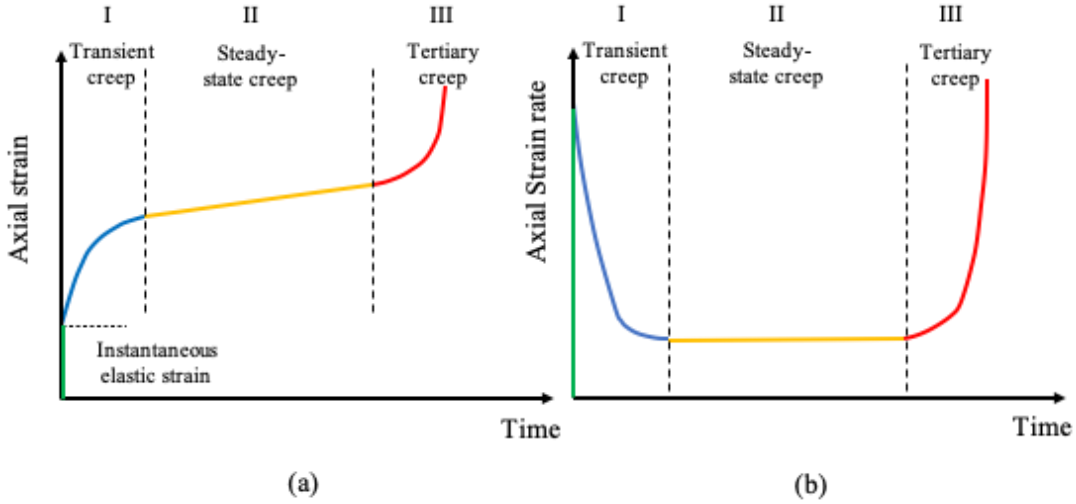

Figure 2.3: Typical rock salt responses observed in long-term creep tests: (a) axial strain vs. time and (b) axial strain rate vs. time.

Transient or primary creep occurs immediately after the instantaneous response with creep strains rates that reduces due to the strain hardening. Steady-state, stationary or secondary creep takes place once the creep strain rate approaches to a constant value. The final stage, accelerated or tertiary creep, reveals a rapid increment in creep strain rate due to the crack growth and the damage propagation. A more detailed description is specified in the following chapter.

2.2.2.3 Long-term failure

The long-term failure or creep rupture takes place when rock salt damage reaches to a certain threshold known as "dilatancy boundary" or "long-term failure boundary". When the stress state is in the compressibility zone (i.e., below the dilatancy boundary), a time-dependent ductile deformation without any visible macroscopic cracking is observed; therefore, critical conditions such as crack propagation and brittle failure do not occur below the dilatancy boundary (Khaledi, 2018 (9)). On the other hand, in the dilatancy zone, the deformation mechanism are dominated by the inter-crystalline micro-cracking, grain rotation and inter-granular slip resulting in the increment of the rock salt sample volume (dilatancy). In dilation behavior, according to Van Sambeek et al., 1993 (18), the volume increase observed in laboratory creep and quasi-static tests on salt core can be attributed to microcraking that causes an increase in permeability and the interconnected porosity. Although finding the dilatancy boundary may represent a challenge, it should be object of study due to the great influence in long-term projects that

involve rock salts.

2.3 Rock salt importance

Evaporites are clearly important from an economic point of view. Besides of the fact that halite, the commonly consumed salt, is one of the most important evaporitic minerals for humans, they are associated with large oil accumulation due to their role as a sealing rock for oil reservoir.

Petroleum in the liquid state is an oily substance and flammable with the characteristic smell and color variance between black and light brown. It is composed of a mixture of organic chemical composts (hydrocarbons), (Thomas, 2001 (19)). The state of the petroleum depends on its molecule size since the presence in their majority of little molecules indicates petroleum in physical and gaseous state whereas a mixture with larger molecules state a physical and liquid state.

Furthermore, the occurrence of oil in significant quantities in a sedimentary basin involves the existence of large volumes of organic matter accumulated when depositing certain sedimentary rocks that are called source rocks, which requires to be submitted to adequate temperatures and pressure in order to generate petroleum (Milani et al., 2000 (20)).

After the oil generation in source rocks, the space/volume they start to occupy is larger than the original; therefore, source rocks becomes supersaturated and the excessive pressure causes fractures, allowing the expulsion of fluids to lower pressure zones. The migration of petroleum fluid away from the source rocks through different routes in the subsurface ends once they arrive into a place with porous space and an adequate permeability to store and drain oil in economical quantities (reservoir rock). Having met generation, migration and reservoir condition, in order to allow the accumulation of oil, there is the need to find a waterproofing situation that prevents them from escaping. Normally, this condition is provided by the seal or cap rock, located above the reservoir rocks, which prevent the escape of fluids, trapping them and thus forming an oil accumulation (Milani et al., 2000 (20)). Fig. 2.4 illustrates the migration of petroleum from source to reservoir rock as well as the cap rock.

Evaporites present seal rocks characteristics since they are practically impermeable; therefore, their importance in oil industry relays on the fact that evaporites help to create sealing barriers for hydrocarbons, enabling their accumulation. In addition to the accumulation of hydrocarbons, the sealing characteristic of these rocks makes their use interesting for the storage of gas and atomic waste in saline caves (Botelho, 2008, (4)). As result of evaporites applications, oil industry has focused and invested on the study of the behavior of these evaporitic rocks.

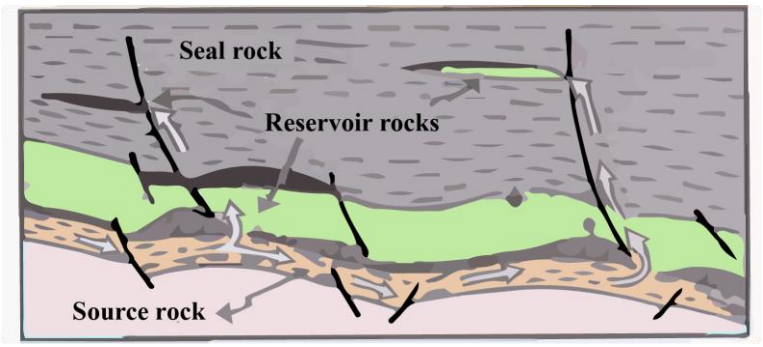

Figure 2.4: Spatial relationships between generating rocks, reservoir and sealants, modified from Thomas, 2001 (19).

Since environments where the rate of evaporation exceeds the rate of precipitation or other water arrivals are regions for evaporitic deposits, continental and marine environments from deserts to hypersaline seas, are the possible regions in the world to find evaporitic rocks. There are significant deposits in the deep waters of the Gulf of Mexico and in offshore regions of West Africa, in Brazil, in the South of the North Sea and the Middle East (Botelho, 2008, (4)). According to PETROBRAS, oil exploration and production activity in Brazil is one of the major components of investments in order to develop, produce and incorporate oil reserves in a safe and profitable way. In Fig. 2.5 is shown the location of onshore and offshore basins in Brazil. The two important basins in Brazil are Campos and Santos Basin. While Campos Basin is the most prolific offshore basin in oil production at present, Santos Basin is one of the most promising offshore exploration sites in the world (PETROBRAS, 2019). Furthermore, most of the Brazilian production is from pre-salt reservoirs, which are among the most significant in the world in the last decade.

2.4 Wellbore in evaporite formations

Guaranteeing the wellbore stability during drilling is a key concern in oil industry. Stuck pipe as a consequence of large borehole deformation and even worse the breakout or hole closure because of compressive and shear rock failure are involved with wellbore instability (Dusseault, 1994 (21)).

Since the rock strength is in equilibrium with the in-situ rock stress before the drilling process, a discontinuity of stresses in the formation is generated when the rock salt around the wellbore is removed. The drilling is followed by the injection of a drilling-fluid pressure into the well in order to replace part of the canceled horizontal stress. Due to the fact that the casing takes a certain operational time, stability must be ensured on the wellbore by preventing its excessive deformation and ruptures.

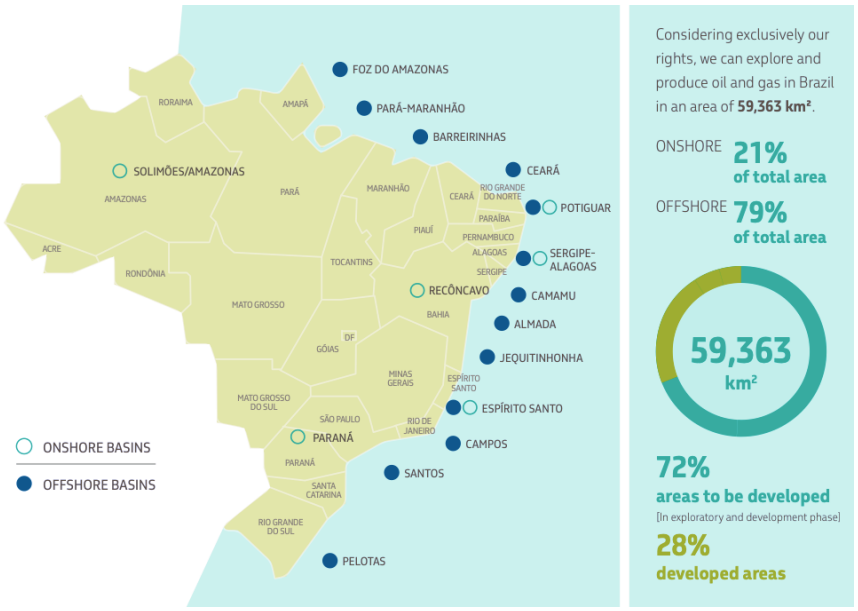

Figure 2.5: Location of onshore and offshore basins in Brazil, PETROBRAS, 2019.

Fig. 2.6 presents operational drilling problems in evaporite formations. The creep behavior of rock salt is an important factor that can cause the well to close even before drilling completion operations are finished. Wellbore instability can be chemically or mechanically induced. Firstly, the common chemically-induced instability in salt formations is leaching, which may create large cavities around the wellbore and contaminate the drilling fluid to the extent that it must be completely replaced, and wellbore enlargement as a result from salt dissolution (Xu, 2007 (22)).

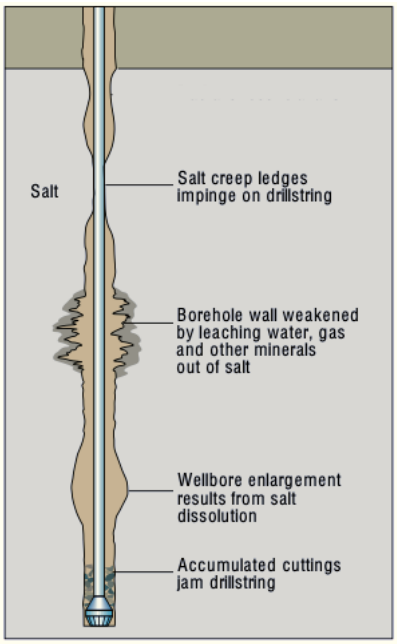

Figure 2.6: Potential drilling problems in evaporites, adapted from Farmer et al., 1996 (2.3).

In addition, saline rocks are highly soluble materials, which contribute to the formation of cavities and caves along the well (Firme, 2013 (5)). Secondly, as stated previously, in-situ stress state of equilibrium in rock salt formation at depth are disturbed when drilling; therefore, if the drilling-fluid pressure does not bring the altered stresses to the original state, the mechanically-induced instabilities can develop. Furthermore, the mud weight of the injected drilling-fluid need to be the necessary as to generate the pressure that carries some of the load, reduces the stress on the formation at the borehole wall and avoids failure; on the contrary, an over estimated mud weight may result in the formation splitting in a tensile fracture causing lost circulation (Xu, 2007 (22)). In addition, a low mud weight may allow creep to impinge on the drillstring.

In evaporites family, rock salt mobility can vary according to their depositional environment. While bischofite and carnalite are the most mobile, halite is slow-moving and anhydrite and dolomite are essentially immobile (Amer et al., 2016 (24)). According to Gamboa et al., 2008 (25), rock salt with low mobility (e.g. halite) is an ideal formation for drilling because the salt is homogeneous, has low porosity, high fracture gradient (pressure required to induce fractures in a rock at a given depth) and, in general, present a good penetration rate. On the other hand, irregular wellbore sections are obtained in situations where halite and anhydrite layers are intercalated since halite tends to form cavities and anhydrite, according to Giambastiani, 2005 (26), is an evaporitic rock with negligible dissolution and creep behavior for geomechanical purposes.

Besides, casing failures in salt zones is another subject of interest in oil engineering. Probably, casing collapse is the main concern related to the development of the Pre-salt areas, which demands the construction of wells with preserved structural integrity for at least 25 years (Beltrão et al., 2009 (27)).

According to Beltrão et al., 2009 (27), a successful well construction of a well is ensured by the achievement of proper cement fill on the annular space; on the contrary, bending of the casing can occur as salt flow tends to close the borehole, see Fig. 2.7 (a). Moreover, the pipe can flatten in case cement placements results in only a partial sheath around the casing as specified in Fig. 2.7 (b).

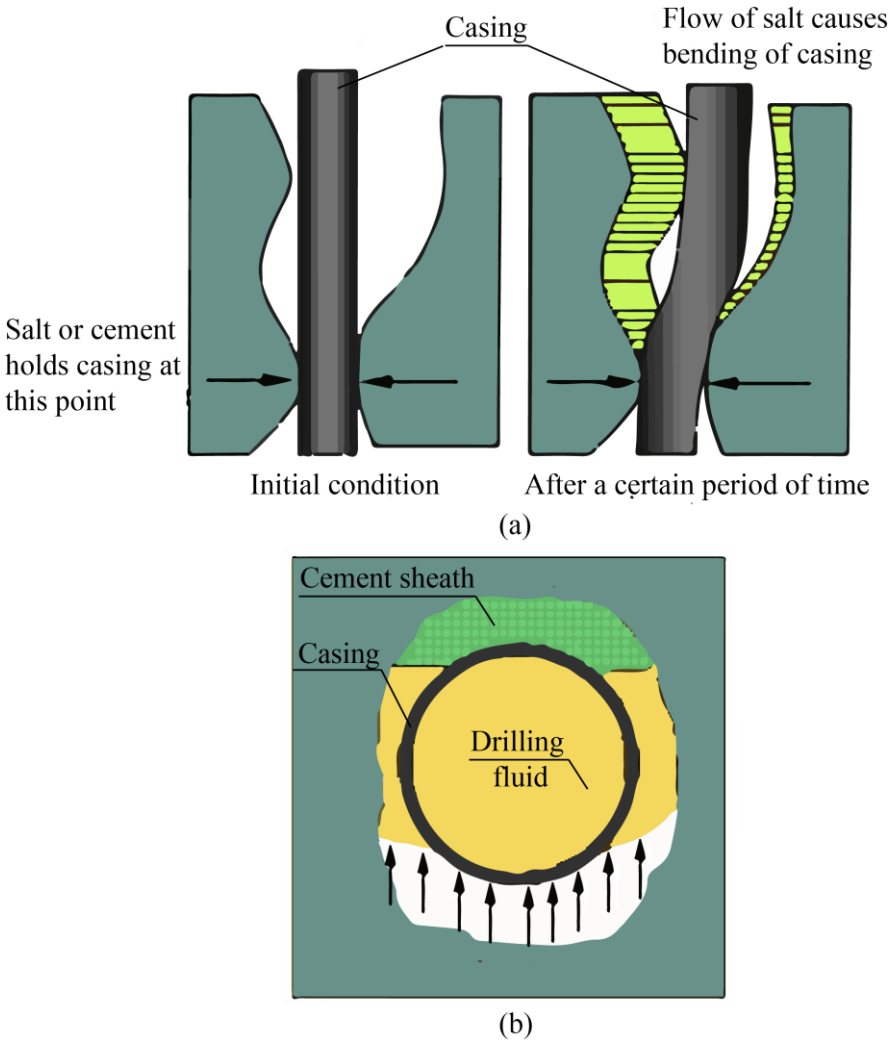

Figure 2.7: (a) Bending of casing and (b) Nonuniform load casing caused by salt movement, adapted from Cheatham et al., 1964 (28).

3 Time dependent behavior

3.1 Introduction

The mechanical behavior of evaporites has been a priority for many decades for oil industry due to the fact that most of the geomechanical problems are involved with the time-dependent behavior of rock salt. Moreover, modeling evaporites is a challenge for engineers since a knowledge of their time dependent behavior gives an understanding of the movements of salt rocks surrounding an excavation prior a fracture. An ideal model is defined by the quality of the input parameters, which sometimes are uncertain, and its ability to validate laboratory test. There are an abundance of numerical models developed to describe evaporites time dependent behavior, which are described in this chapter.

3.2 Time dependent behavior

One of the most important properties of geomaterials, such as rock and soil, to take into account in geotechnical challenges is the time-dependent behavior, which is mainly related to the effects of viscous properties of materials. Strain rate, creep and relaxation are the principal time-dependent effects, being all manifestations of the time-dependent nature of microcrack development (Hudson and Harrison, 2000 (29)). It is shown in Fig. 3.1 a rock sample experimenting compression by a contiguous element (spring), which is observed specifically in underground excavation where the stiffness of the rock mass is the responsible of loading the adjacent element of rock. It is graphically observed the stress-strain path for two of the main effects mentioned above.

Creep is the deformation over time of the material, being significant at a constant stress (line AC) and stress relaxation refers to the time-dependent reduction in stress at a constant strain (line AR). Moreover, line AK represents the combination of both (creep and relaxation), when the rock experiments a time-dependent unloading along the stiffness line of the loading configuration. Depending on whether the control variable is stress or strain, the rock will be continually creeping or relaxing, respectively, during generation of the complete stress-strain curve (Hudson and Harrison, 2000 (29)).

3.2.1 Creep

As it was mentioned, creep is just one aspect of the time-dependent behavior of rocks emerging as a result of underground excavation, geological processes and even natural conditions, being of considerable help in evaluating long-term stability of rock engineering structures. Creep is defined as the time-dependent deformation of rock subjected to a stress that is less than the short-term strength of the rock. Creep strain can seldom be recovered fully when stresses are removed, thus it is largely plastic deformation (Hudson and Harrison, 2000 (29)).

It is know that creep tests are carried out for a short limited time in comparison with the very long creep time of in situ rock. Even so, the short-term

testing of the rock will be of assistance for the long-term deformation and strength behavior of in situ rock.

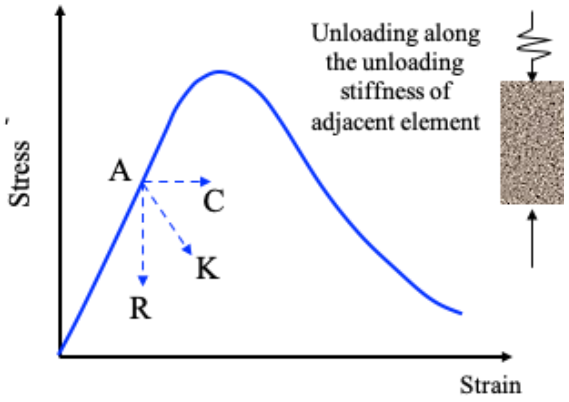

Figure 3.1: Creep, stress relaxation and time dependent unloading along the stiffness of the adjacent element. Adapted from Hagros et al., 2008 (30)

The idealized curve of creep deformation for a rock subjected to a constant stress over time and high enough as to take the rock sample through all creep stages sketched in Fig. 3.2 can in principle, according to Jaeger et al., 2007 (31), be represented by an equation of the form:

$$\varepsilon = \varepsilon_e + \varepsilon_1(t) + V(t) + \varepsilon_3(t) \qquad (3\text{-}1)$$

where ε_e is the instantaneous elastic strain, $\varepsilon_1(t)$ is the primary or transient creep, $V(t)$ is the secondary or steady-state creep, and $\varepsilon_3(t)$ is the tertiary or accelerating creep.

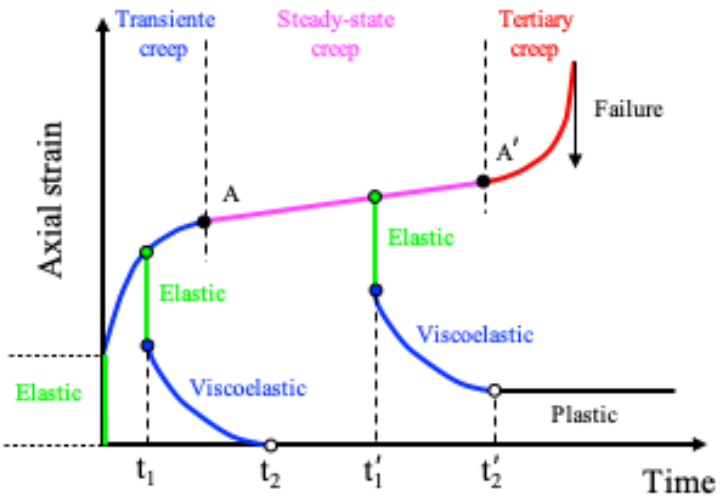

Figure 3.2: Conventional interpretation of creep stages behavior.

Moreover, in Fig. 3.2, it is observed the development of the creep deformation because of the application of a long-term stress. At the beginning of

the curve, the instantaneous elastic strain occurs immediately as the stress is applied to the rock sample, then, as the stress is kept constant the rate of strain decreases (primary creep). The transition to the secondary creep occurs at the moment the creep curve approaches a constant strain rate. At the end of this stage, the material rapidly fails as the strain rate starts to accelerate (tertiary creep).

It is worth to mention again that the stress applied to the rock sample has to represent a high fraction of the short-term strength in order to ensure the steady-state creep stage, and consequently the accelerating creep.

On the other hand, creep deformation path for different types of rocks is not developed in the same way. Creep in hard brittle rocks is rare as deformation rate is extremely slow and hard rock shows creep behavior appreciably only at elevated temperatures and pressures generally not encountered in engineering structures. Soft rocks, contrarily, creep mostly at the room temperature, atmospheric pressure and deviatoric stress range normally encountered in engineering structures (Ghosh and Rao, 2015 (32)), see Fig. 3.3.

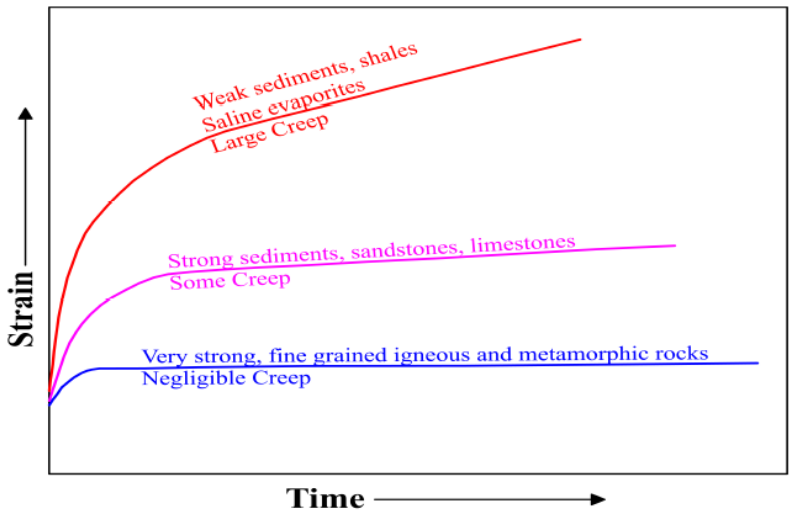

Figure 3.3: Comparative creep characteristics for the same stress level in different types of rock, adapted from Ghosh and Rao, 2015 (32).

3.2.2 Stress relaxation

According to Hudson and Harrison, 2000 (29), stress relaxation is defined as decreasing stress at constant strain. Peng and Podnieks, 1972 (33) define relaxation as the time-dependent behavior of stress within a stressed elastic body, which was demonstrated by holding deformation constant in the conventional strength test. Peng and Podnieks, 1972 (33) performed relaxation test on tuff rock samples in order to study relaxation behavior. Basically, the test consists of holding at constant deformation the specimens for five minutes in different stages along the complete stress-strain curve. As a result, it was observed that stresses do not drop when the rock sample was under below stress levels where the stress-strain curve deviates from linearity or below the crack damage threshold. Furthermore, at the

moment of the stress-strain curve deviates a small stress drop was noticeable and its magnitude increased as the stress level incremented. Peng and Podnieks, 1972 (33) concluded stress relaxation is directly associated with crack formation and propagation. On the other hand, in the stress-strain curve before deviates, stress relaxation was not observed because the surfaces of the microcracks in that region were too small.

In later studies of Peng, 1973 (34), it was mentioned that since in a relaxation test the deformation is held constant, no external energy is established on the specimen and when cracks begins, the load-bearing capacity of the specimen decay reducing the applied stress immediately in order to maintain the strain constant.

In accordance with Paraskevopoulou et al., 2017 (35), relaxation behavior consists of three stages as illustrated in Fig. 3.4. These stages can be noted through stress relaxation-time and radial strain-time curves, although a slight delay from stage to stage is observed when comparing these two curves.

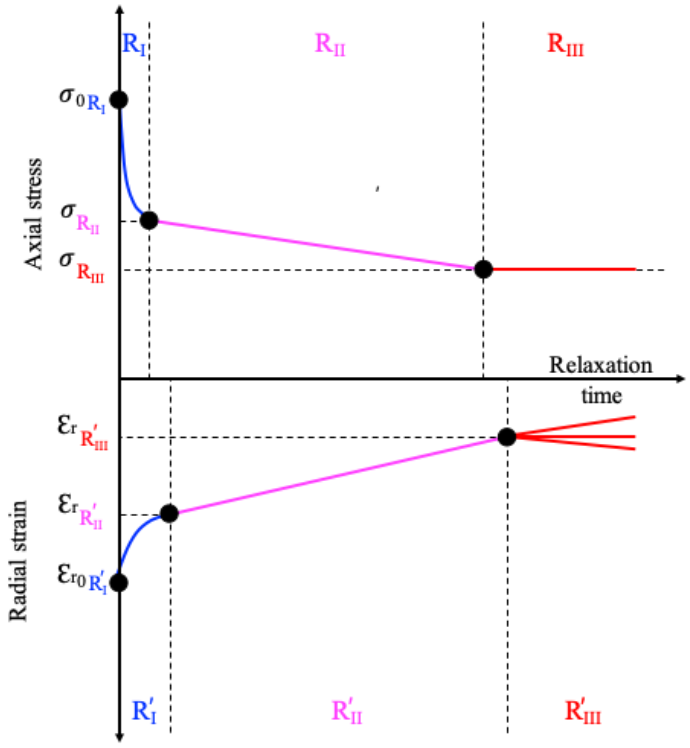

Figure 3.4: Three stages of the relaxation stress process during a relaxation test (Paraskevopoulou et al., 2017 (35)).

The first stage of stress relaxation (R_I) is manifested at the moment that stress lowers with a decreasing rate due to the constant deformation. When the stress begins to decrease with a constant rate, the second stage of stress relaxation (R_{II}) is reached and continues until the stress relaxation can not be measured because of the achieving of stress-time curve as an asymptote, indicating the development of

the third stage (R_{III}).

Besides, the third stage of stress relaxation does not always result in a asymptote in the radial strain-time curve, as Fig. 3.4 shows. Paraskevopoulou et al., 2017 (35) mention that combination of three-dimensional visco-elastic response and crack behavior during stable propagation with a constant axial strain are possibly associated to the different development of the third stage relaxation.

Paraskevopoulou et al., 2017 (35) also describe the percentages of the total stress relaxation (R_T) that corresponds to each stage. While the first stage of the stress relaxation represent the 55% to 95% of the total stress relaxation, the second an third stage can just be part of the 5% to 45%.

3.3 Time dependent theoretical modeling

A vast variety of models have been proposed over the years to describe the time dependent behavior of rocks based on experimental data from field and laboratory test. Basically, according to the literature, constitutive models can be divided into three major approaches: empirical models, rheological models and elasto-viscoplastic models.

3.3.1 Empirical models

Empirical models are obtained by formulating mathematical expressions of a small number of parameters according to experimental results. Empirical laws usually give a good approximation of transient and steady state creep contributing in this way to geotechnical engineering problems since assumed boundary conditions correspond to the presented in the test (Gioda, 1981 (36)). Moreover, due to the fact that tertiary creep can not be expressed with a simple equation based on tests that last very short periods of time in comparison with the reached in a real geotechnical engineering problem, the validation and suitability of these empirical models in the long term prediction are dubious (Xu et al., 2018 (37)).

The empirical models most often used are such as the power law, the exponential law and the hyperbolic law. As reported by Phienwej et al., 2007 (38), time-dependent behavior of most rocks is found to be adequately described by the power law (Obert, 1965 (39), Singh, 1975 (40), de Orellana, 1996 (41)); nevertheless, for faulted rocks, the exponential law and the hyperbolic law are more commonly used (Semple et al., 1973 (42), Febres-Cordero and Mesri, 1974 (43), Mesri et al., 1981 (44), Lin and Wang, 1998 (45)).

In Brazilian rock salt mechanics, the constitutive equation of the double deformation mechanism (Dusseault et al., 1987 (46)) has been widely used although this model simulates the steady-state creep rate, but does not account for the transient creep (Firme et al., 2018 (47)).

3.3.2 Rheological models

Rheological models are composed of three primary one-dimensional mechanical elements (Hooke spring, Newton damper and St. Venant slipping element) attached to each other in different configurations (parallel, series or a

combination of both) and constitutive rules (linear or nonlinear). The spring element is described by a constant stiffness modulus or a stress- or strain-dependent modulus (nonlinear elasticity) representing elastic deformations that are fully recovered after removing the applied stress, the dashpot is the creep strain element producing unrecoverable deformation with time and the slider simulates plastic strain when the stress equals or exceeds the yield stress (Hudson, 1993 (48)).

The mechanical elements make it possible to stablish: elastoplastic, viscoplastic, viscoelastic and visco-elasto-plastic models. Viscoelastic models correspond to the rheological models conformed by springs (elastic element) and dashpots (viscous element) without presence of sliders (plastic element). The three basic viscoelastic models are the Kelvin-Voight's, Maxwell's and Burger's models which differ mainly in the way the mechanical elements are connected. These basic rheological models (Fig. 3.5) just describe approximately the strain-stress-time relationship of rock; therefore, a model capable of reproducing the real time dependent behavior of rocks requires a large number of mechanical elements that result in a complicated mathematical expression having a large number of parameters that are not so simple to determine (Kaiser, 1979 (49)).

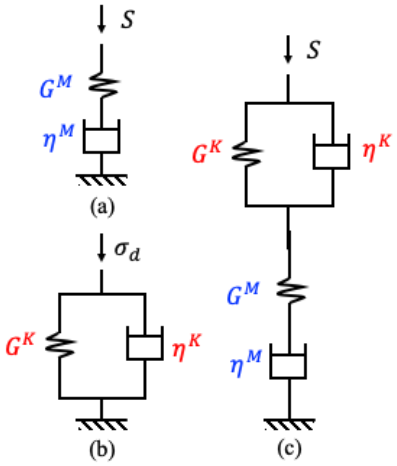

Figure 3.5: Viscoelastic rheological models:(a) Maxwell's, (b) Kelvin-Voight's and (c) Burger's models.

3.3.2.1 Maxwell's model

Maxwell's model is composed of a linear spring and a linear damper element in series. The governing constitutive differential equation for this model is expressed as follows:

$$\dot{\varepsilon} = \frac{\dot{S}}{G^M} + \frac{S}{\eta^M} \tag{3-2}$$

where S and $\dot{S}$ is the deviatoric stress and deviatoric stress rate, $\dot{\varepsilon}$ is the strain rate, G^M is the maxwell shear modulus and η^M is the maxwell viscosity coefficient.

Maxwell's model can develop: the secondary state of creep (see Eq. 3-3)

superimposed on the instantaneous elastic strain and also the stress relaxation effect (see Eq. 3-4).

$$\varepsilon_{(t)} = \frac{S}{G^M} + \frac{S}{\eta^M} t \tag{3-3}$$

$$S = G^M \varepsilon e^{-\frac{G^M}{\eta^M} t} \tag{3-4}$$

in which ε is the reached strain in a time t.

3.3.2.2 Kelvin-Voight's model

Kelvin-Voight's model is composed of a linear spring and a linear damper element in parallel where the strain experienced by the spring is the same as that experienced by the dashpot. The differential equation for this model is expressed as follows:

$$S = G^K \varepsilon + \eta^K \dot{\varepsilon} \tag{3-5}$$

where η^K is the kelvin viscosity coefficient and G^K is the kelvin shear modulus.

Kelvin-Voight's model is deficient as a model for creep behavior because it does not exhibit an instantaneous strain (Jaeger et al., 2007 (31)) and just reproduces an asymptotic exponential response at a constant stress which corresponds to the primary state of creep (see Eq. 3-3). Besides, because in a stress relaxation the stress is taken up by the spring and will continue over time constant, this viscoelastic model is unable to describe the relaxation stress effect.

$$\varepsilon = \frac{S}{G^K}\left(1 - e^{-\frac{G^K}{\eta^K} t}\right) \tag{3-6}$$

3.3.2.3 Burger's model

Burger's model is characterized by describing instantaneous strain, transient and steady-state creep. This model results from a serial combination of the Kelvin-Voight's model, considering the kelvin shear modulus (G^K) and the viscosity coefficient of kelvin (η^K) as its parameters, with Maxwell's model, assuming the maxwell shear modulus (G^M) and the viscosity coefficient of maxwell (η^M) as its parameters. The governing equation for this model is expressed as follows:

$$\eta^K \ddot{\varepsilon} + G^K \dot{\varepsilon} = \frac{\eta^K}{G^M} \ddot{S} + \left[1 + \frac{G^K}{G^M} + \frac{\eta^K}{\eta^M}\right] \dot{S} + \frac{G^K}{\eta^M} \ddot{S} \tag{3-7}$$

The strain response of this model for a creep test is basically the sum of Kelvin and Maxwell models strains responses as showed in Eq. 3-8 and the formulation for a stress relaxation test considering $P_1 = \left(\frac{\eta^K}{G^K} + \frac{\eta^M}{G^K} + \frac{\eta^M}{G^M}\right)$, $P_2 = \frac{\eta^K \eta^M}{G^K G^M}$, $q_1 = \eta^M$ and $q_2 = \frac{\eta^K \eta^M}{G^K}$ as constants, see Eq. 3-9.

$$\varepsilon = \frac{S}{G^M} + \frac{S}{G^K}\left[1 - e^{-\frac{G^K}{\eta^K}t}\right] + \frac{S}{\eta^M}t \tag{3-8}$$

$$S = \frac{\varepsilon}{Z}[(q_1 - q_2 r_1)e^{-r_1 t} - (q_1 - q_2 r_2)e^{-r_2 t}] \tag{3-9}$$

where $Z = \sqrt{P_1^2 + 4P_2}$, $r_1 = \frac{P_1 - Z}{2P_2}$ and $r_2 = \frac{P_1 + Z}{2P_2}$.

3.3.3 Elasto-viscoplastic models

Elasto-viscoplastic models are three dimensional constitutive models that are characterized by describing not only the time dependent behavior but also the inviscid or time independent response. These models can be divided into three categories: nonstationary flow surface (NSFS) theory, overstress theory and others.

3.3.3.1 Nonstationary flow surface theory

The NSFS theory is based on the concepts of inviscid elastoplasticity and a result of its further development (Liingaard et al., 2004 (50)), where the yield condition definition is the fundamental difference. The classical theory of plasticity indicates that under a constant plastic strain the yield condition remains invariable over the time and consequently the yield surface can be regarded as stationary. So, for an isotropic hardening material the yield condition is expressed as follows:

$$f(\sigma'_{ij}, \varepsilon_{ij}^p) = 0 \tag{3-10}$$

where σ'_{ij} is the effective stress and ε_{ij}^p is the plastic strain.

On the other hand, the nonstationary flow surface theory which is extended from the yield surface so as to depend on time by letting it include a variable describing the time dependent alteration of the yielding property of materials in addition to the stress and internal variables (Hashiguchi and Okayasu (51)). The time dependent yield condition for the NSFS theory is stated as follows:

$$f(\sigma'_{ij}, \varepsilon_{ij}^{vp}, \beta) = 0 \tag{3-11}$$

in which ε_{ij}^{vp} is the viscoplastic strain and β is the time-dependent function.

In the NSFS theory, elastic strains are developed when the stress state lies inside the flow surface $(f < 0)$ and in case the stress state lies on or within this surface an elastoviscoplastic state is reached producing elastic and viscoplastic strains. In addition, due to the inclusion of a time-dependent function (β) in the yield condition $(f = 0)$ it is possible to reproduce the flow surface in a stress space with different stress states (A, A_1, A_2), see Fig. 3.6.

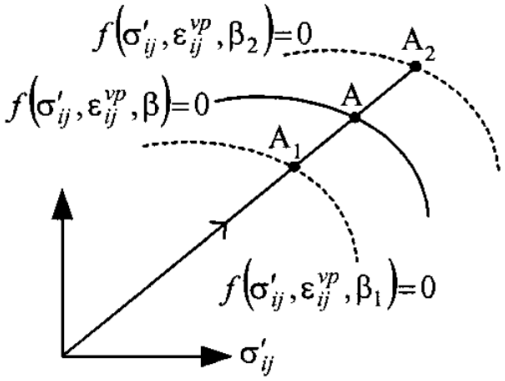

Figure 3.6: Loading path and yield surfaces for an elastoviscoplastic material (Liingaard et al., 2004 (50)).

3.3.3.2 Overstress theory

The overstress theory was developed by Perzyna, 1963 (52) and is a three-dimensional extension constitutive model of the one-dimensional Bingham's rheological model (consisted of a parallel unit of dashpot and slider connected in series with a linear spring mechanical element).

Perzyna's overstress theory follows the traditional yield surface associated with time-independent plasticity in the elastic zone (no viscous strains occur within the static yield surface), i.e elastic strains are time independent whereas the inelastic strains are time dependent describing combined viscous and plastic effects (Liingaard et al., 2004 (50)). The total strain rate can be expressed as follows:

$$\dot{\varepsilon}_{ij} = \dot{\varepsilon}^{e}_{ij} + \dot{\varepsilon}^{vp}_{ij} \tag{3-12}$$

Here, $\dot{\varepsilon}_{ij}$ is the total strain rate tensor and the superscripts e and vp indicate the elastic and viscoplastic components that obey the generalized Hooke's law and flow rule, respectively.

$$\dot{\varepsilon}^{vp}_{ij} = \dot{\lambda}(F)\frac{\partial g}{\partial \sigma'_{ij}} \tag{3-13}$$

where $\dot{\lambda}(F)$ is the viscoplastic scalar multiplier and a function of the overstress (F), g is the potential function and σ'_{ij} is the effective stress state tensor.

According to Perzyna, 1963 (52), the overstress function (F) is defined as the distance in stress space between the rate sensitive loading surface denominated as the dynamic loading surface or dynamic yield surface (f_d) and the static behavior of the material represented by the static yield surface, i.e the time independent plasticity yield surface (f_s), as showed in fig. 3.7.

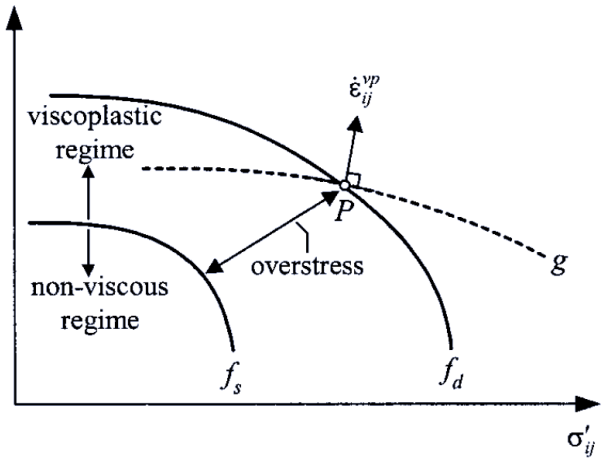

Figure 3.7: Static (f_s) and dynamic (f_d) loading surfaces, elastic and visco-plastic regimes in Perzyna's model (Liingaard et al., 2004 (50)).

In short, the difference between the overstress and classic plasticity theory lies on the assumptions for inelastic strains. The overstress theory involves that inelastic strains are related to only the current stress point and not to the stress history while the classic plasticity theory, to the stress rate.

4 Model description and numerical implementation

4.1 Introduction

An elasto-viscoplastic three-dimensional model proposed by Sterpi and and Gioda, 2007 (53) is implemented in the numerical finite difference code FLAC 3D using an explicit algorithm, which is based on the centered finite difference method varying in time and written in C++ programming language in order to generate a dynamic link library (DLL). This elasto-viscoplastic model adopts a Mohr-Coulomb type surface for the viscoplastic yield condition with a non-associated flow rule and proved successful in simulating the primary, secondary and tertiary creep stage of a rock.

4.2 Sterpi and Gioda model framework

The EVP model developed by Sterpi and and Gioda, 2007 (53) is based in Gioda, 1981 (36) and Gioda and Cividini, 1996 (54) research. At first, Gioda, 1981 (36) presented a simple deviatoric rheological model for a pure shear stress state as showed in Fig. 4.1. This rheological model consists of a visco-elastic Kelvin unit accounting for primary creep connected in series with a visco-plastic Bingham model, in which the frictional component is governed by the classical Drucker and Prager yield condition with associated flow rule, accounting for secondary creep. The tertiary creep is reached by decreasing the rheological model viscosity with increasing shear stresses and creep strains.

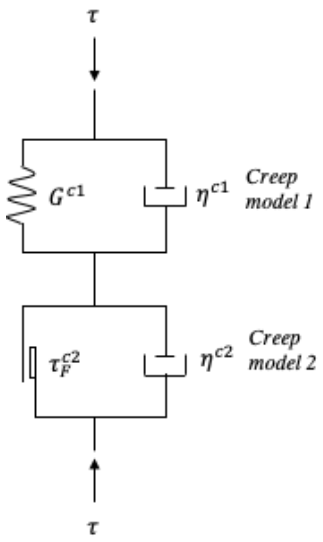

Figure 4.1: Gioda, 1981 (36) deviatoric rheological model.

Then, Cividini, 1996 (54) assumed a different law governing the variation of the rheological model viscosity in order to develop the tertiary creep in reference with the previous work. In this regard, the shear strength $(\phi,\ c)$ and viscosity (η) parameters of the Bingham unit depend on a scalar measure of the irreversible deformation represented by the square root of the second invariant of the deviatoric

creep strain (J_2^{cr}). According to Cividini, 1996 (54), the parameters of the constitutive model keep their peak values until the deviatoric deformation reaches a first limit value (J_p). Immediately, a linear reduction of the parameters takes place with increasing the second invariant of the deviatoric creep strain, leading to their residual values when a second limit (J_r) is reached, as illustrated in Fig. 4.2.

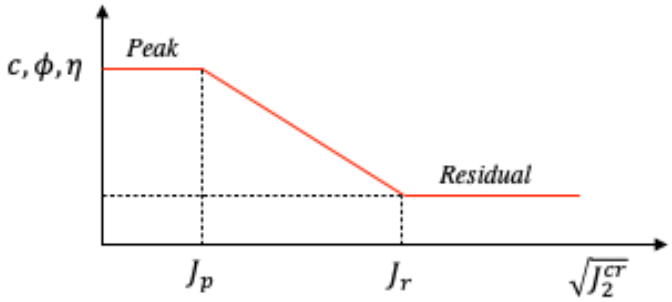

Figure 4.2: Variation of the parameters of the visco-plastic model with deviatoric plastic strains, Cividini, 1996 (54).

In a following approach, Sterpi and and Gioda, 2007 (53) exposed an elasto-viscoplastic model composed of three terms, in which this work is based on, as specified in Fig. 4.3. Basically, this model is based on Perzyna's viscoplastic theory (Perzyna, 1966 (55)) and consists of an elastic element represented by the shear (G^e) and bulk modulus (B^e) that involve a reversible, deviatoric and volumetric response, a visco-elastic Kelvin unit defined by a deviatoric dashpot and a elastic mechanical element with the deviatoric parameters of kelvin viscosity coefficient (η^K) and shear modulus (G^K) neglecting the volumetric behavior of rock mass, and the visco-plastic Bingham unit comprised of a dashpot viscous element characterized by the viscosity coefficient (η^{vp}) assuming only deviatoric stress and a plastic slider that introduces the visco-plastic limit envelope $(F^{vp} = 0)$ through the cohesion (C^{vp}), friction angle (ϕ^{vp}) and dilation (ψ^{vp}) viscoplastic parameters.

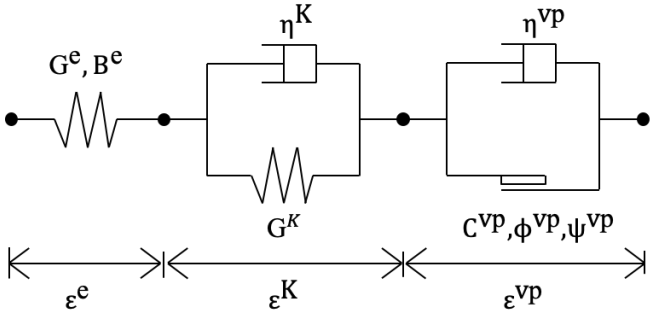

Figure 4.3: Elasto-viscoplastic model of Sterpi and and Gioda, 2007 (53) with associated parameters.

The independent strain represented by a linear spring follows the Hook's law to reproduce the instantaneous elastic strains (ε^e). Under a deviatoric constant stress below the visco-plastic yield surface, only reversible visco-elastic strains (ε^K) and primary creep are reached, Fig. 4.4 (a). At overcoming that threshold, irreversible visco-plastic strain (ε^{vp}) are manifested accounting for secondary creep as long as the parameters are constant, see Fig. 4.4 (b). Tertiary creep takes place when the square root of the second invariant of the deviatoric viscoplastic strains (Eq. 4-1), which depends on the deviatoric strain tensor, attains a particular level that actives a law governing the variation of the mechanical parameters shown in Fig. 4.5 from their peak (maximum) to their residual (minimum) values (softening behavior).

$$J_2^{e^{vp}} = \frac{1}{2} e_{ij} e_{ij} \tag{4-1}$$

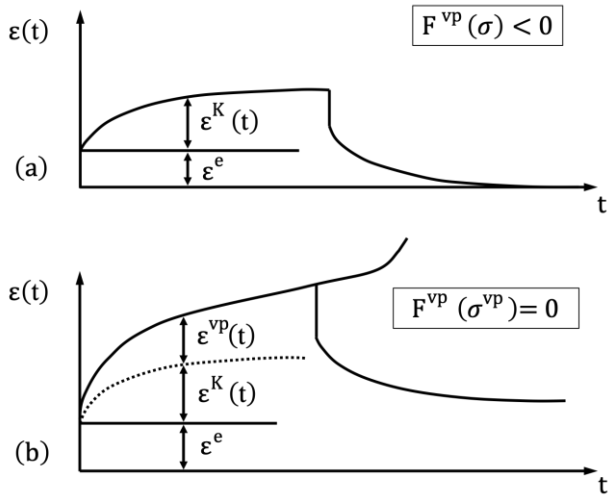

Figure 4.4: Creep strain associated with a constant deviatoric stress in loading and unloading paths: (a) primary creep and (b) secondary and tertiary creep (Sterpi and and Gioda, 2007 (53)).

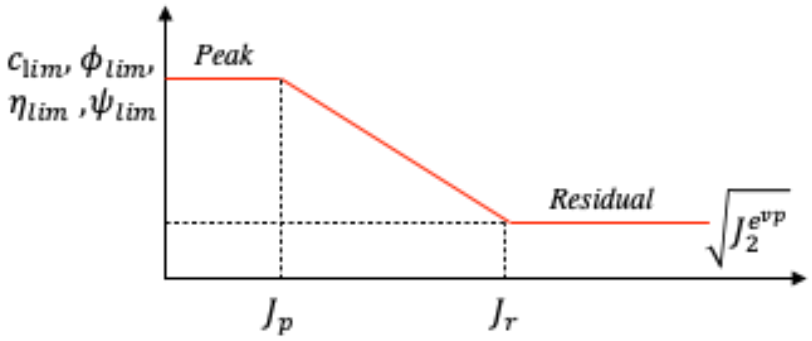

Figure 4.5: Variation of the visco-plastic parameters with the 2nd invariant of deviatoric visco-plastic strains (Sterpi and and Gioda, 2007 (53)).

Then, the total strain tensor (ε_{ij}) in the elasto-viscoplastic model is decomposed in three parts as follows:

$$\varepsilon_{ij} = \varepsilon_{ij}^{e} + \varepsilon_{ij}^{K} + \varepsilon_{ij}^{vp} \tag{4-2}$$

In order to reduce the constitutive relations of the elasto-viscoplastic model it is convenient to express these responses in terms of volumetric and deviatoric components of stress (σ_{ij}) and strain (ε_{ij}) tensor. A

$$\sigma_{ij} = \sigma_m \delta_{ij} + S_{ij} \tag{4-3}$$

$$\varepsilon_{ij} = \frac{\varepsilon_{vol}}{3}\delta_{ij} + e_{ij} \tag{4-4}$$

Here, σ_m refers to hydrostatic tensor of stress, ε_v refers to volumetric tensor of strain, S_{ij} and e_{ij} refer to deviatoric tensor of stress and strain and δ_{ij} refers to the Kronecker's delta equivalent to 1 $(i = j)$ or 0 $(i \neq j)$.

4.2.1 Instantaneous behavior

Sterpi and and Gioda, 2007 (53) elasto-viscoplastic model uses a linear elastic response to describe the instantaneous behavior of the rock mass, which corresponds to the first element presented in Fig. 4.3. The elastic part of the deformation follows the Hooke's law, which can be expressed in the next incremental form:

$$\dot{\varepsilon}_{ij}^{e} = \frac{\dot{\sigma}_m}{3B^e}\delta_{ij} + \frac{\dot{S}_{ij}}{2G^e} \tag{4-5}$$

4.2.2 Time dependent behavior

The deviatoric creep behavior of the elasto-viscoplastic model conformed by the viscoelastic Kelvin and viscoplastic Bingham unit describes the following deviatoric creep strain rate tensor $(\dot{e}_{ij}^{c})$.

$$\dot{e}_{ij}^{c} = \dot{e}_{ij}^{K} + \dot{e}_{ij}^{vp} \tag{4-6}$$

where $\dot{e}_{ij}^{K}$ is the deviatoric strain rate tensor developed by the Kelvin element and $\dot{e}_{ij}^{vp}$ is the reproduced by the viscoplastic unit.

4.2.2.1 Viscoelastic Kelvin unit response

For the Kelvin model, deviatoric stress S_{ji} and deviatoric strain e_{ij}^{K} have the following relation:

$$S_{ij} = 2\eta^{K}\dot{e}_{ij}^{K} + 2G^{K}e_{ij}^{K} \tag{4-7}$$

By writing Eq. 4-7 in the form of finite increments:

$$\bar{S}_{ij}\Delta t = 2\eta^{K}\Delta e_{ij}^{K} + 2G^{K}\bar{e}_{ij}^{K}\Delta t \tag{4-8}$$

where $\triangle e_{ij}^{K} = e_{ij}^{K,N} - e_{ij}^{K,O}$, $\bar{S}_{ij} = (S_{ij}^{N} + S_{ij}^{O})/2$ and $\bar{e}_{ij}^{K} = (e_{ij}^{K,N} + e_{ij}^{K,O})/2$, among which $\bar{S}_{ij}$ and $\bar{e}_{ij}^{K}$ refer to the average deviatoric stress and strain

of the Kelvin model, respectively. Then, S_{ij}^{N} refers to the new deviatoric stress tensor (step $i+1$) and S_{ij}^{O} to the previous one (step i); $e_{ij}^{K,N}$ and $e_{ij}^{K,O}$ refer to the new deviatoric strain tensor (step $i+1$) and to the previous one (step i), respectively.

By replacing the definitions of variation and average deviatoric stress and strains in Eq. 4-8, the updated new deviatoric strain expression in the Kelvin model can be as follows.

$$e_{ij}^{K,N} = \frac{1}{A}\left[\left(S_{ij}^{N} + S_{ij}^{O}\right)\frac{\Delta t}{4\eta^{K}} + Be_{ij}^{K,O}\right] \tag{4-9}$$

where $A = 1 + G^{K}\Delta t/(2\eta^{K})$ and $B = 1 - G^{K}\Delta t/(2\eta^{K})$.

4.2.2.2 Viscoplastic softening unit response

The viscoplastic unit, as already mentioned, is composed of a viscoplastic dashpot and slider element, both in parallel describing equal deviatoric strain rates.

$$\dot{e}_{ij}^{vpd} = \dot{e}_{ij}^{vp} \tag{4-10}$$

Here, $\dot{e}_{ij}^{vpd}$ and $\dot{e}_{ij}^{vp}$ refer to the deviatoric strain rate tensor contributed in the viscoplastic dashpot and the viscoplastic slider element, respectively. Regarding the viscous element, the governing constitutive relation is given in the next formulation.

$$S_{ij}^{vpd} = 2\eta^{vp}\dot{e}_{ij}^{vpd} \tag{4-11}$$

where S_{ij}^{vpd} is the portion of deviatoric stress carried by the viscoplastic dashpot, which can be obtained through the stress equilibrium for the viscoplastic unit.

$$\sigma_{ij} = \sigma_{ij}^{vp} + S_{ij}^{vpd} \tag{4-12}$$

Here, σ_{ij} is the total stress tensor and σ_{ij}^{vp} is the stress tensor carried by the plastic slider, which carries the entire hydrostatic stress (σ_m).

On the other hand, in the viscoplastic slider, a Mohr-Coulomb type surface is adopted for the visco-plastic yield condition, with the following non-associated flow rule.

$$\dot{\varepsilon}_{ij}^{vp} = \dot{\lambda}\frac{\partial Q^{vp}}{\partial \sigma_{ij}^{vp}} \tag{4-13}$$

in which $\dot{\lambda}$ is the viscoplastic multiplier and Q^{vp} is the viscoplastic potential function. The yield criterion and potential functions are described as follows.

$$F^{vp} = \sigma_1^{vp} - \sigma_3^{vp}\frac{1+sin\phi^{vp}}{1-sin\phi^{vp}} + 2C^{vp}\sqrt{\frac{1+sin\phi^{vp}}{1-sin\phi^{vp}}} \tag{4-14}$$

$$Q^{vp} = \sigma_1^{vp} - \sigma_3^{vp}\frac{1+sin\psi^{vp}}{1-sin\psi^{vp}} + 2C^{vp}\sqrt{\frac{1+sin\psi^{vp}}{1-sin\psi^{vp}}} \tag{4-15}$$

4.2.3 Viscoplastic multiplier

As specified before, each part of the elasto-viscoplastic model is connected in series; therefore, the incremental form of the deviatoric strains are summed up.

$$\triangle e_{ij} = \triangle e_{ij}^{e} + \triangle e_{ij}^{K} + \triangle e_{ij}^{vp} \tag{4-16}$$

The incremental deviatoric elastic strain (e_{IJ}^{e}) can be related to the incremental deviatoric stress $(\triangle S_{ij})$ as follows:

$$\triangle S_{ij} = 2G^{e} \triangle e_{ij}^{e} \tag{4-17}$$

Moreover, when combining Eq. 4-9 with Eq. 4-17 and Eq. 4-16 the new deviatoric stress can be reproduced as the following equation.

$$S_{ij}^{N} = \frac{1}{a}\left[\triangle e_{ij} - \triangle e_{ij}^{vp} - \left(\frac{B}{A}-1\right)e_{ij}^{K,O} + bS_{ij}^{O}\right] \tag{4-18}$$

where $a = \frac{1}{G^{e}} + \frac{\triangle t}{4\eta^{K}A}$ and $b = \frac{1}{G^{e}} - \frac{\triangle t}{4\eta^{K}A}$

On the other hand, the viscoplastic unit is governed by the deviatoric strain relation specified in Eq. 4-10, which can be developed as follows:

$$\dot{\lambda}\frac{\partial Q^{vp}}{\partial \sigma_{ij}^{vp}} - \frac{\dot{\varepsilon}_{vol}^{vp}}{3}\delta_{ij} = \frac{S_{ij}^{vpd}}{2\eta^{vp}} \tag{4-19}$$

By replacing the S_{ij}^{vpd} of Eq. 4-12 in Eq. 4-19, the stress components carried by the slider can be written as:

$$\begin{aligned}
\sigma_1^{vp} &= \sigma_1 - 2\eta^{vp}\dot{\lambda}\left(\frac{2}{3} + \frac{N_{(\psi^{vp})}}{3}\right) \\
\sigma_2^{vp} &= \sigma_2 - 2\eta^{vp}\dot{\lambda}\left(-\frac{1}{3} + \frac{N_{(\psi^{vp})}}{3}\right) \\
\sigma_3^{vp} &= \sigma_3 - 2\eta^{vp}\dot{\lambda}\left(-\frac{1}{3} - \frac{2N_{(\psi^{vp})}}{3}\right)
\end{aligned} \tag{4-20}$$

where $N_{(\psi^{vp})} = \frac{1+sin\psi^{vp}}{1-sin\psi^{vp}}$.

The viscoplastic multiplier is obtained by substituting Eq. 4-20 in the yield criterion function solving it for $F^{vp} = 0$.

$$\dot{\lambda} = \frac{\sigma_1(1-sin\phi^{vp}) - \sigma_3(1+sin\phi^{vp}) + 2C^{vp}cos\phi^{vp}}{\frac{2}{3}\eta^{vp}\left[3 + 3N_{(\psi^{vp})} + N_{(\psi^{vp})}sin\phi^{vp} - sin\phi^{vp}\right]} \tag{4-21}$$

4.3 Background of FLAC 3D

The commercial code FLAC 3D (Fast Lagrangian Analysis of Continua in 3 Dimensions) is a computational tool based on an explicit finite volume scheme

that relies on three following different approaches in order to find a numerical solution: finite volume approach, which is considered when first-order space and time derivatives are approximated by finite volumes; discrete-model approach, which is considered when the continuous medium is represented by a discrete model conformed by nodes and zones in which boundary conditions, such as applied and interactive forces, are located in the nodes; and the dynamic-solution approach, which involves using the inertial terms in the equations of motion during the analysis in order to reach the equilibrium state od the system. In this chapter, a numerical background is described in order to understand the solution method used in FLAC 3D; the grid discretization procedure and some aspects regarding creep behavior is addressed as well. Finally, the numerical integration algorithm followed during the implementation of the Sterpi and Gioda model is described.

4.3.1 Mathematical description

The general principles (definition of strain, laws of motion), and the constitutive equations that define the idealized material are taken into account to drive the mechanism of the medium. The established geometries and properties with the specified boundary and initial condition involve a set of partial differential equations that relate mechanical (stress) and kinematic (strain rate, velocity) variables.

4.3.1.1 Explicit dynamic solution scheme

All the approaches FLAC 3D is based on are considered in a calculation sequence adopted to find the numerical solution, see Fig. 4.6. This procedure is characterized as an explicit, dynamic solution scheme since an explicit finite volume approximation is used to derive new velocities and displacements on the basis of the equations of motion.

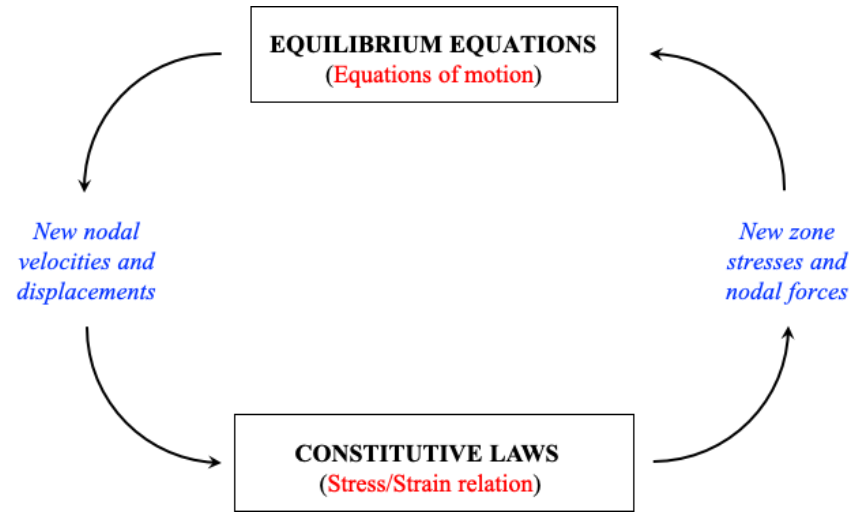

Figure 4.6: Explicit calculation cycle.

Generally, the procedure starts with the computing of nodal forces from applied loads, stresses and body forces. External work rate is equalized to internal

work rate. Internal work rate considers strain rate and stress while external work rate nodal velocities and body forces (gravitational force). Then, new nodal velocities and displacements are obtained. Consequently, the strain rate tensor of each element is determined. Finally, new stresses are obtained through a constitutive law.

The scheme allows to physically isolate field quantities such as forces, stresses, velocities or displacements at each zone in the model from the rest of them during a calculation step. This allows to reduce computational costs when finding the numerical solution, resulting in an important advantage over other types of solution scheme.

4.3.1.2 Equations of motion and equilibrium

The solution of a continuum medium problem in FLAC 3D requires of the Cauchy's equations of motion (4-22), which establish a new field of nodal velocities that vary linearly over a time interval.

$$\sigma_{ij,j} + \rho b_i = \rho \frac{dv_i}{dt} \tag{4-22}$$

where $\sigma_{ij,j}$ is the partial derivatice of the stress tensor with respect to x_j (position vector), ρ is the mass-per-unit volume of the medium, $[b]$ is the body force per unit mass, and $\frac{d[v]}{dt}$ is the material derivative of the velocity (acceleration). For a fixed time, Eq. 4-22 can be rewritten as the following expression.

$$\sigma_{ij,j} + \rho B_i = 0 \tag{4-23}$$

$$B_i = \rho \left(b_i - \frac{dv_i}{dt} \right) \tag{4-24}$$

where B_i represent the boy forces.

Besides, in an infinitesimal time (dt), when the medium particles move with velocity, an infinitesimal strain derived by the translation $v_i dt$ is experienced in the medium; therefore, the component of the strain rate tensor in function of the velocity gradient is expressed as follows:

$$\dot{\varepsilon}_{ij} = \frac{1}{2}(v_{i,j} + v_{j,i}) \tag{4-25}$$

4.3.2 Numerical formulation

The representative discrete model reaches equilibrium conditions when the sum of the nodal contributions $[P]$ (concentrated forces and applied loads) and the statically equivalent forces $-[f]$ are equal to zero at each node. In order to express this condition numerically, Newton's law is presented:

$$F_i^{<l>} = M^{<l>} \left(\frac{dv_i}{dt} \right)^{<l>} \qquad l = 1, n_n \tag{4-26}$$

where the superscript $< l >$ refers to a node in the global node numbering, meaning that a variable with the superscript $< l >$ is related to the value of the

variable at node $< l >$; v refers to nodal velocities, n_n refers the total number of nodes involved in the representative model, $M^{<l>}$ is the nodal mass and $F^{<l>}$ is the out-of-balance force, which is based on the nodal formulation of the equations of motion that Itasca – FLAC 3D (2017) provided:

$$F_i^{<l>} = \left[\left[\frac{T_i}{3} + \frac{\rho b_i V}{4}\right]\right]^{<l>} + P_i^{<l>} \tag{4-27}$$

where ρ is the mass per unit volume of the medium, b_i is the body force per unit mass, V is the element volume, P_i is the nodal contributions of applied loads and concentrated forces and T_i is a vector defined as:

$$T_i^{<l>} = \sigma_{ij} n_j^{<l>} S^{<l>} \tag{4-28}$$

where σ is the stress tensor, n is the unit vector normal to each face of the element and S represents the surface of the element face. Itasca – FLAC 3D (2017) rewrote equation 4-26 as a system of ordinary differential equations in order to solve it by an explicit finite difference formulation in time:

$$\frac{dv_i}{dt}^{<l>} = \frac{1}{M^{<l>}} F_i^{<l>}\left(t, \{v_i^{<1>}, v_i^{<2>}, v_i^{<3>}, \ldots, v_i^{<p>}\}^{<l>}, k\right); \qquad l = 1, n_n \tag{4-29}$$

where k is a parameter that takes into account the history of loading, the symbol $\{\}^{<l>}$ refers to the subset of nodal velocity values involved in the analysis at global node l. Thus, the derivative $(dv_i/dt)^{<l>}$ is calculated using central finite differences obtaining the following expression:

$$v_i^{<l>}\left(t + \frac{\Delta t}{2}\right) = v_i^{<l>}\left(t - \frac{\Delta t}{2}\right)$$

$$+ \frac{\Delta t}{M^{<l>}} F_i^{<l>}\left(t, \{v_i^{<1>}, v_i^{<2>}, v_i^{<3>}, \ldots, v_i^{<p>}\}^{<l>}, k\right) \tag{4-30}$$

Nodal velocities are obtained using the previous recurrence relation, whereas the node location is similarly obtained by using the central difference approximation:

$$x_i^{<l>}(t + \Delta t) = x_i^{<l>}(t) + \Delta t v_i^{<l>}\left(t + \frac{\Delta t}{2}\right) \tag{4-12}$$

Finally, the nodal displacements are obtained under the following relation:

$$u_i^{<l>}(t + \Delta t) = u_i^{<l>}(t) + \Delta t v_i^{<l>}\left(t + \frac{\Delta t}{2}\right) \tag{4-32}$$

where,

$$u_i^{<l>}(0) = 0 \tag{4-33}$$

Considering a known velocity field, the components of the strain-rate tensor can be computed after applying a finite volume approximation to space derivatives. Itasca – FLAC 3D (2017) derived the following definition of the strain-rate tensor $\dot{\varepsilon}_{ij}$ in terms of the node velocities:

$$\dot{\varepsilon}_{ij} = -\frac{1}{6V}\sum_{l=1}^{4}\left(v_i^l n_j^{(l)} + v_j^l n_i^{(l)}\right)S^{(l)} \tag{4-34}$$

where V is the element volume, S is the element surface, n refers to the unit vector normal to the respective face and v represents the nodal velocities. Based on the type of grid, a discretization procedure is applied in order to obtain the strain-rate tensor of the zone. On the other hand, the stress tensor components can be obtained from a known strain-rate tensor and the incremental form of the adopted constitutive model.

4.3.3 Grid discretization

In FLAC 3D, a continuous medium is represented by a discrete model that is conformed by nodes and zones in order to approach a numerical solution. There are four typical zone shapes: brick, wedge, pyramid and tetrahedron. In FLAC 3D, mixed discretization technique is used to overcome overly stiff elements and to give zones more volumetric flexibility. A zone corresponds to an assembly of two overlapped set of tetrahedra (n_t). In FLAC 3D brick, wedge, pyramid and tetrahedron are assembly of ten, six, four, and two tetrahedrons, respectively. By default, hexahedral zones are adopted; however, tetrahedral zones may be used as well. Based on the type of zone, a different discretization technique is taken into account to calculate the strain-rate and stress tensors.

4.3.3.1 Mixed discretization for a hexahedral grid

In the case of adopting a hexahedral grid, the continuous medium is discretized into sets of tetrahedra that conform a coarser grid of hexahedral zones. Specifically, one hexahedral zone is conformed by two overlays of five tetrahedral elements each as shown in Fig. 4.7 in order to ensure symmetric response under symmetric loading; however, calculations can be done considering one overlay as well. This technique was initially introduced by Marti and Cundall, 1982 (56) and based on determining the first invariant of the strain-rate tensor of the zone by calculating the volumetric average value over all the tetrahedra involved.

The mixed discretization technique is applied for the case of a hexahedral grid, where each tetrahedron that conforms a hexahedral zone is locally labeled with a superscript l and analyzed in order to determine the strain-rate tensor components of the zone. Thus, the strain-rate tensor of a tetrahedron is initially estimated and separated as follows:

$$\dot{\varepsilon}_{ij}^{[l]} = \dot{e}_{ij}^{[l]} + \frac{\dot{\varepsilon}^{[l]}}{3}\delta_{ij} \tag{4-35}$$

where $\dot{\varepsilon}^{[l]}$ is the strain-rate first invariant and $\dot{e}_{ij}^{[l]}$ is the deviatoric strain-rate tensor. Then, a strain-rate first invariant corresponding to the hexahedral zone is obtained by computing the volumetric-average over all the tetrahedra involved:

$$\dot{\varepsilon}^{[z]} = \frac{\sum_{k=1}^{n_t} \dot{\varepsilon}^{[k]} V^{[k]}}{\sum_{k=1}^{n_t} V^{[k]}} \tag{4-36}$$

where $V^{[k]}$ is the volume of tetrahedron k and n_t is the total number of subzones. Finally, the strain-rate tensor components of each tetrahedron is redefined as:

$$\dot{\varepsilon}_{ij}^{[l]} = \dot{e}_{ij}^{[l]} + \frac{\dot{\varepsilon}^{[z]}}{3}\delta_{ij} \tag{4-37}$$

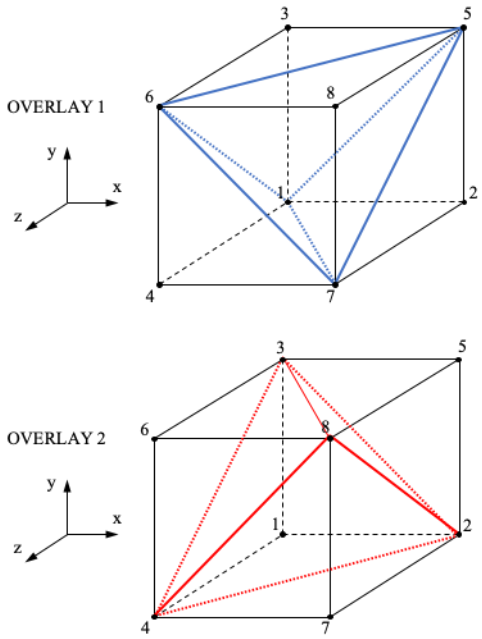

Figure 4.7: Hexahedral zone with two overlays of five elements each.

Similarly, the mixed discretization technique is applied to the stress tensor. First, the stress tensor of each tetrahedral zone is initially estimated and divided as follows:

$$\sigma_{ij}^{[l]} = S_{ij}^{[l]} + \sigma^{[l]}\delta_{ij} \tag{4-38}$$

where $\sigma^{[l]}$ is the mean normal stress and $S^{[l]}$ is the deviatoric stress tensor. Consequently, the first invariant of the stress tensor that corresponds to the hexahedral zone is determined in a similarly as the strain-rate first invariant. Thus, volumetric-average value over all the tetrahedra is obtained:

$$\sigma^{[z]} = \frac{\sum_{k=1}^{n_t} \sigma^{[k]} V^{[k]}}{\sum_{k=1}^{n_t} V^{[k]}} \tag{4-39}$$

and, finally, the tetrahedron stress tensor components are redefined by considering the expression below:

$$\sigma_{ij}^{[l]} = s_{ij}^{[l]} + \sigma^{[z]}\delta_{ij} \tag{4-40}$$

4.3.4 Critical time step in FLAC 3D

Time dependent behavior is numerically taken into account by elasto-viscoplastic constitutive models by the implementation of the time step in their equations. The estimation of a maximum creep time step can be calculated as the ratio of the material viscosity to the shear modulus as shown in the following expression:

$$\Delta t_{max}^{cr} = \frac{\eta}{G} \tag{4-41}$$

Considering that the estimation of creep time step is important to ensure numerical accuracy, Itasca – FLAC 3D (2017) recommended an initial creep time step of two or three orders of magnitude smaller than the maximum creep time step. In FLAC 3D, a constant value of time step can be adopted; however, an automatic option can be used as well following a criteria where the time step can be decreased if the maximum out-of-balance criteria exceeds some threshold and increased it goes below another level.

4.3.5 Creep material models in FLAC 3D

At this time, nine creep models have bee implemented in FLAC 3D. They all are differenced by their complexity and applicability. The first creep model is the classical viscoelastic formulation known as the Maxwell substance, which describe materials with both viscous and elastic behaviors. The second model is two-component power law most know as the Norton power law. This model is used for mining applications that involve the creep behavior od salt. The third model is known as the WIPP-reference creep law, which was developed for thermomechanical analyses for nuclear waste associated with studies for underground isolation of nuclear waste in salt. The fourth model is the Burgers-Creep viscoplastic model, which consists of the classical formulation of the Burgers substance combined with the Mohr-Coulomb model. The fifth model is an extension of the second implemented model by including the Mohr-Coulomb component. The sixth model refers to the power-law viscoplastic model with ubiquitous joints. This model is capable of simulating the visco-elasto-plastic mechanical behavior of ubiquitous joint rock with creep occurring in a rock matrix. The seventh model is the WIPP-Creep viscoplastic model, which combines the viscoelastic WIPP-reference creep law with the Drucker-Prager plasticity component. The eighth model is also an adaption of the third and includes volumetric and deviatoric compaction behavior. Finally, the last model is the soft-soil-creep model.

4.3.6 Implementation procedure

The implementation of a constitutive model has the objective of computing the stress increment that corresponds to a strain increment and its procedure varies depending on the integration algorithm to be adopted. In this section, the used implementation procedure is presented as a flowchart in Fig. 4.8, which adopts a

Forward Euler integration method by means of a routine written in C++ language, compiled as DLL (dynamic link library) file. The DLL file is loaded into FLAC 3D and it returns updated stresses, parameters and kelvin strains for each given strain increment.

Since the constitutive law is written for each sub-zone (depending on the geometry of the element), the hardening or softening parameters for each zone are determined through a volumetric-average of these quantities.

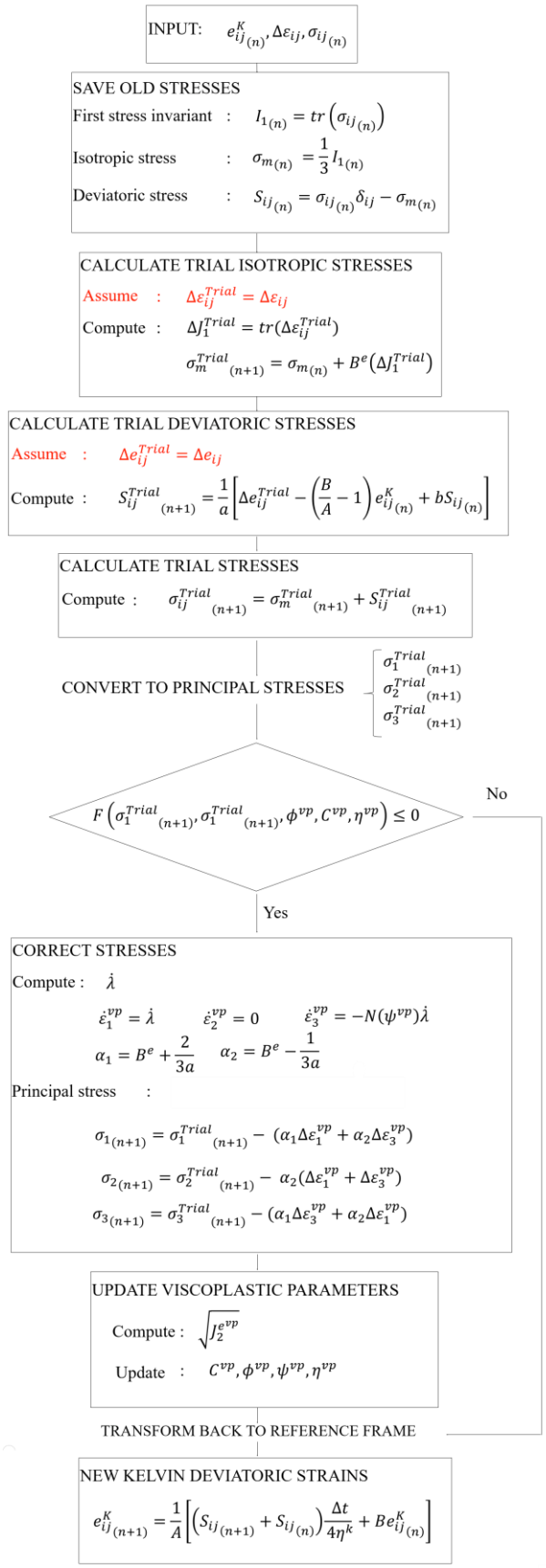

Figure 4.8: Conceptual scheme of the implementation procedure of the Sterpi and Gioda model in FLAC 3D.

5 Numerical validation

5.1 Introduction

This chapter provides a series of numerical analyses of uniaxial creep tests on schist samples to prove the well implemented elastic-viscoplastic model in FLAC 3D. In addition, a series of triaxial creep tests on halite samples taken from wells located in the Northeast of Brazil (Sergipe State) are presented to determine parameters associated with the elasto-viscoplastic model. The overall process of parameter identification involves calibration and recommendation of these values in order to obtain a better agreement when comparing computed numerical results with experimental data from triaxial tests.

5.2 Implementation validation

The validation of a well implemented constitutive model was made through uniaxial creep tests that can be also be considered diagnostic tests, which reveal the time-dependent properties exhibited by intact schist rocks from Palazu Mare presented by Cristescu and Hunsche, 1998 (57).

5.2.1 Uniaxial creep test on schist

Experimental results for five different specimens of schist sample is presented in Fig. 5.1. It is observed that for the three smallest loading axial stresses, it is only developed transient creep stage, i.e., creep deformation stops after a determined time. Regarding the two experimental curves with the largest axial deformations, the three stages of creep are observed before reaching failure (last point of the curve). It is important to mention that although these curves are referred to different specimens, these are subjected to the same axial stress value.

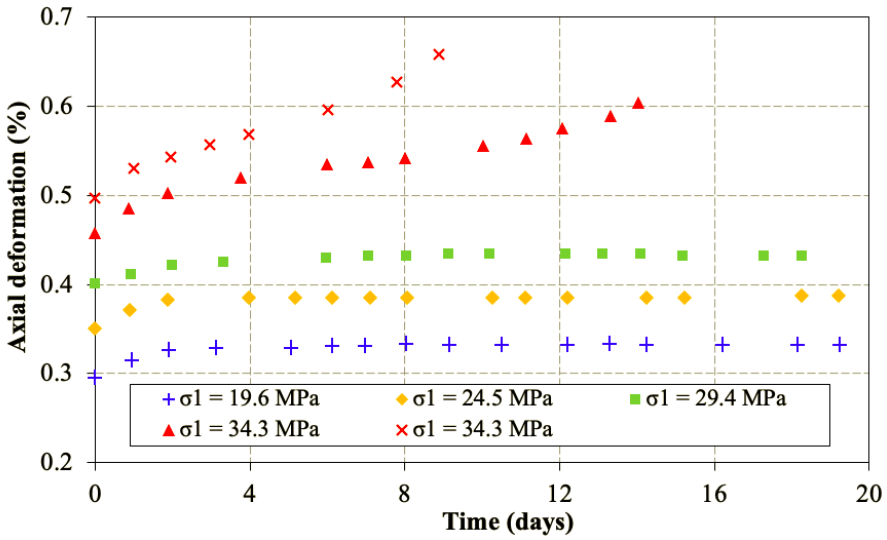

Figure 5.1: Uniaxial experimental creep curves for schist obtained with various loading stresses (Cristescu and Hunsche, 1998 (57)).

5.2.2 Parameters identification

Determination and calibration of the mechanical parameters are accomplished through experimental tests such as uniaxial, biaxial or triaxial creep test carried out at different stress levels to ensure that samples reach the three stages of creep.

In reference to the parameters associated with the time-independent response of the schist samples, Sterpi and Gioda, 2007 (53) present the corresponding parameters of shear and bulk modulus, see Table 5.1. On the other hand, the visco-elastic parameters are estimated by assuming that for a low deviatoric stress, only the Kelvin unit takes place in addition to the elastic unit. It is considered that deviatoric strains are only developed by the visco-elastic unit, i.e., volumetric strains as negligible. The kelvin shear modulus G^K is obtained through Eq. 5-1, which considers a completely relaxed dashpot for a long time span, and the Kelvin viscosity is determined with Eq. 5-2, which results from solving the first order non-homogeneous differential Eq. 4-7 considering the initial condition $e^K_{1(t=0)} = 0$.

$$e^K_{1(t\to\infty)} = \frac{S_1}{2G^K} \tag{5-1}$$

$$e^K_{1(t)} = \frac{S_1}{2G^K}\left[1 - \exp\left(-\frac{G^K t}{\eta^K}\right)\right] \tag{5-2}$$

As listed in the following table, the shear modulus of the elastic unit is smaller in comparison with the corresponding of the visco-elastic unit, which is manifested in major values of elastic strains than the visco-elastic strains.

Table 5.1: Mechanical parameters referred to the intact rock from the experimental results (Sterpi and Gioda, 2007 (53)).

	Elastic and visco-elastic parameters			
	B^e (MPa)	G^e (MPa)	η^K (MPa.d)	G^K (MPa)
	5880	2714	49470	23390
	Visco-plastic parameters			
	η^{vp} (MPa.d)	c^{vp} (MPa)	ϕ^{vp} (°)	ψ^{vp} (°)
Peak values	4800	7.88	37.6	20
Residual values	2400	0	20	0

The parameters that define the viscoplastic yield surface were calculated by considering the following steps given by Sterpi and Gioda, 2007 (53). The parameters c^{vp} and ϕ^{vp} are not determined at the instantaneous failure, but estimated once the viscoplastic threshold (σ^{vp}) is attained, i.e., secondary creep stage is experimentally determined. Based on results of biaxial tests that are not

available, Sterpi and Gioda, 2007 (53) define the Hoek-Brown failure criterion with help of the unconfined compression strength ($\sigma_c = 54\ MPa$) of the intact (RMR=100) schist rock sample (Fig. 5.2). The obtained parameters of the Mohr-Coulomb condition were $c = 13.3\ \ MPa$ and $\phi = 37.6°$. Furthermore, experimental data reports an uniaxial stress of 32 MPa that activates the viscoplastic threshold (Sterpi and Gioda, 2007 (53)) with the viscoplastic parameters of $c^{vp} = 7.88\ \ MPa$ and $\phi^{vp} = 37.6°$ determined in the Hoek-Brown envelope.

It is noted that friction angle at the failure remains unchanged to the calculated in the viscoplastic threshold; nevertheless, for the cohesion parameter, the difference between the thresholds of visco-plasticity and of instantaneous failure is due only to a reduction factor that approximately corresponds to a ratio $R_{CS} = 0.6$ between the uniaxial stress that activates the viscoplastic threshold and the unconfined compression strength (Sterpi and Gioda, 2007 (53)).

Since the viscoplastic unit includes the dilation angle (ψ^{vp}) and viscosity coefficient (η^{vp}), both are calibrated through the viscoplastic strain rate expressed in Eq. 5-3. Parameters referred to the tertiary creep are determined by a numerical back analysis in order to provide a better agreement between experimental and numerical results.

$$\dot{\varepsilon}_1^{vp} = \dot{\lambda} \tag{5-3}$$

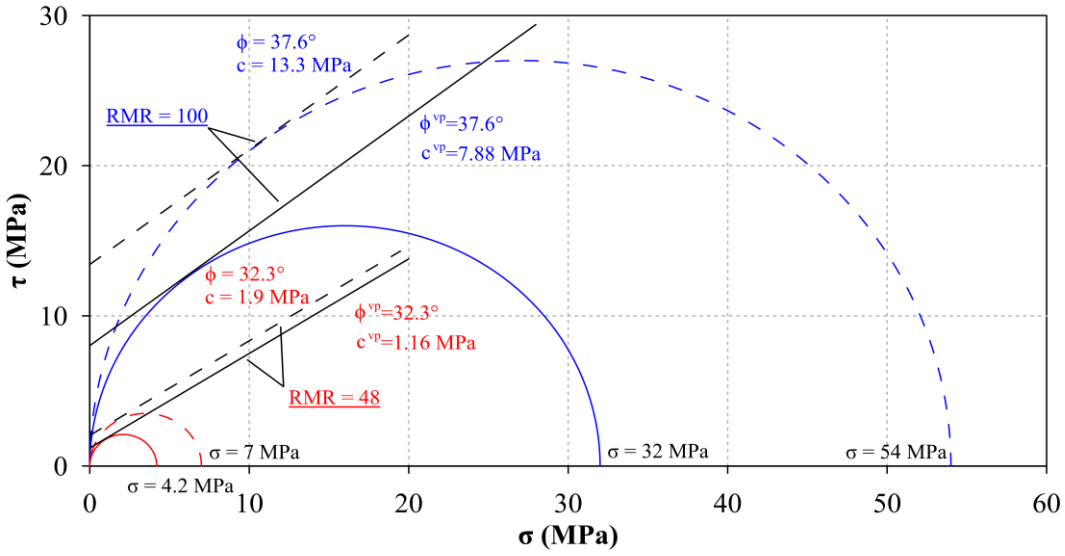

Figure 5.2: Mohr-Coulomb yield functions (dashed lines) and visco-plastic functions (solid lines) for intact rock (RMR = 100) and rock mass (RMR = 48) (Sterpi and Gioda, 2007 (53)).

5.2.3 Comparison of uniaxial results

In Fig. 5.3, it is shown a comparison between experimental (dots) and numerical results (discontinuous lines) of a finite element code by use of Sterpi and

Gioda model. In addition, validation of the well implemented elasto-viscoplastic model in FLAC 3D was proved by reproducing the experimental results of the schist sample. As can be observed, both numerical results fit each other and are in good agreement with experimental results in the three stages of the creep curve.

5.3 Triaxial creep test on halite

In general, the oil industry's experience mentions salt sections of 2000-3000 m thick that overlay targets at depths of 3000-4000 m below mudline in water depth of 2000-2500 m (Maia et al., 2005 (60)). Therefore, it is necessary to understand the behavior of these rock salt sections in order to increase the probability of success regarding oil exploration and avoid operational problems and collapse when drilling these salt layers.

Parameters associated to the implemented elasto-viscoplastic model in FLAC 3D were obtained with help of the experimental data from triaxial tests on halite samples (Maia et al., 2005 (60), Poiate et al., 2006 (62)) taken from wells that have been drilled through thick salt intervals and are located in the Northeast of Brazil (Sergipe State).

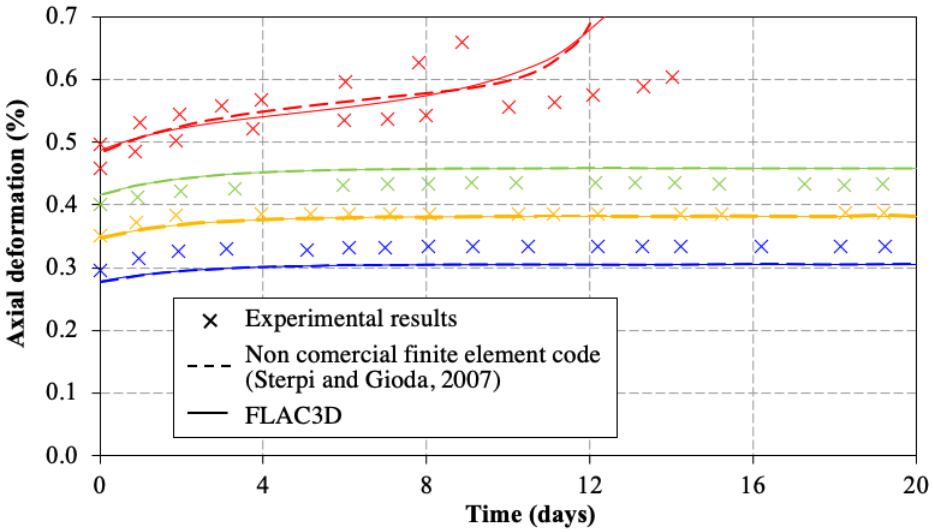

Figure 5.3: Uniaxial creep tests on schist: experimental results (Cristescu and Hunsche, 1998 (57)) and numerical results of a finite element code (Sterpi and Gioda, 2007 (53)) and FLAC 3D by use of Sterpi and Gioda model.

5.3.1 Halite samples

The experimental tests in salt samples were performed in specimens with a length/diameter ratio of 2 according to the ISMR Standards in a Laboratory of Rock Mechanics and Rock Hydraulics from IPT - Institute for Technological Research of the State of Sao Paulo â€“ Brazil. To preserve halite samples, they were stored in places with humidity control due to the high hygroscope of the salts. Furthermore, in order to avoid a wrong prediction of halite samples behavior, they were prepared and submitted to a quality control to verify its structural integrity by

the measurement of compressional velocity (PUNDIT instrument). Thus, samples that presented a compressional velocity below 4300 m/s were rejected.

As evaporitic rock, the porosity of the halite is negligible, being its permeability smaller than 1 μD, what turns the compressional velocity a constant mechanical property independent of the depth. This fact can be observed in a sonic profile of an exploratory well that crosses thick layers of pure halite (Maia et al., 2005 (60)).

5.3.2 Experimental tests

Poiate et al., 2006 (62) presented three triaxial creep tests on carnallite, tachyhydrite and halite samples (Fig. 5.4) that were submitted to a confining pressure of 10 MPa and an axial stress of 20 MPa held constant along the duration of the tests.

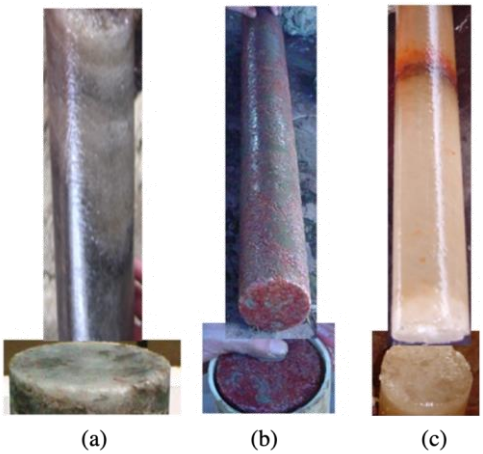

Figure 5.4: Specimens for the triaxial creep tests: (a) Halite, (b) Carnallite and (c) Tachyhydrite (Poiate et al., 2006 (62)).

In Fig. 5.5 is shown the variation of axial strain with time for the three rock salt samples, where carnallite and tachyhydrite exhibit a higher creep rate than halite. Halite specimen was tested for 350 h and it presented an axial strain of 0.0014 before 160 h. Furthermore, it is observed that the halite sample develops a low value of an instantaneous axial strain response and apparently the creep curve only describes the primary stage.

In addition, Maia et al., 2005 (60) also reported triaxial creep tests on halite rock. The specimens were submitted to a confining pressure of 10 MPa and induced to a differential stress. The halite samples before and after the test, in which axial and confined stresses were held constant, are shown in Fig. 5.6.

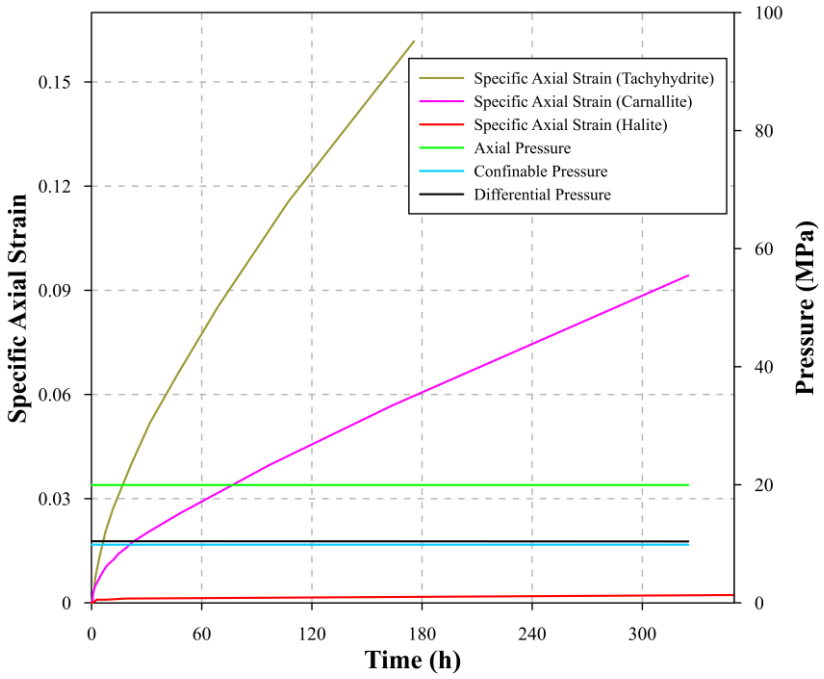

Figure 5.5: Salt creep test for an axial stress of 20 MPa (Poiate et al., 2006 (62)).

(a) (b)

Figure 5.6: Experimental halite specimen (a) before and (b) after test (Maia et al., 2005 (60)).

Halite samples strains were measured with time equal to 1 sec and the recorded results are in Fig. 5.7 and Fig. 5.8 for different axial stress but equal confined pressure. The first triaxial creep test result shown in Fig. 5.7 presents the specific strain when applying an axial stress of 24 MPa during 950 h. A specific axial strain of 0.031 is reproduced at the end of the test and instantaneous response, primary and secondary creep stage is reproduced. Finally, the sample submitted to 26 MPa developed the typical creep behavior of a rock salt showing primary creep

until 200 h, secondary creep between 200 h and 1600 h and tertiary creep thereafter, see Fig. 5.8.

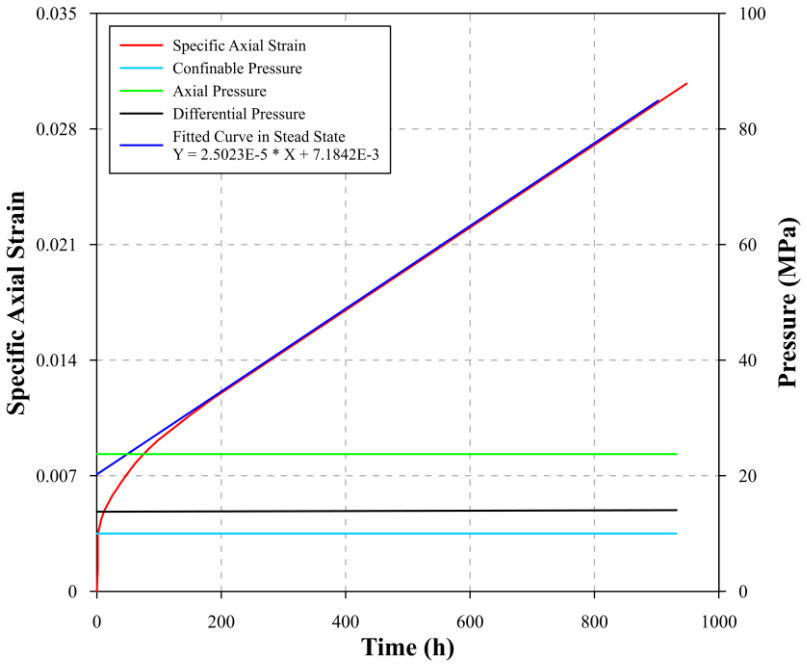

Figure 5.7: Salt creep test for an axial stress of 24 MPa (Maia et al., 2005 (60)).

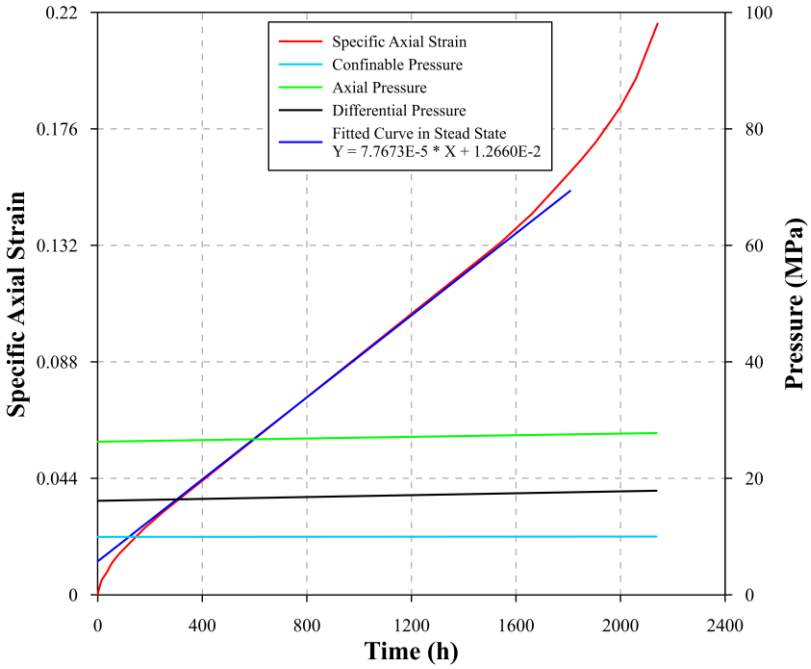

Figure 5.8: Salt creep test for an axial stress of 26 MPa (Maia et al., 2005 (60)).

5.3.3 Parameters identification

Determination and calibration of parameters associated to the elasto-viscoplastic model are carried out with reference to the experimental results of the triaxial creep test on halite samples and correlations presented in the literature. Parameters associated with the time-independent elasto-plastic behavior were reported by Maia et al., 2005 (60), see Table 5.2. The elastic parameters were extracted from tests performed on salt samples from the Taquari Vassouras mining in the State of Sergipe, which consisted only of halite. These parameters have been used in several studies related to creep in evaporites by Brazilian authors (Maia, op. cit.; Poiate Jr, op. cit.; Gonçalves, op. cit.; Costa, op. cit.; Botelho, op. cit.; Medeiros, op. cit.; Gravina, op. cit.).

Table 5.2: Elastic and shear strength parameters (Maia et al., 2005 (60)).

E (MPa)	ν	C (MPa)	ϕ ($^\circ$)
20400	0.36	3.0	43

On the other hand, parameters referred to the dependent behavior of Sterpi and Gioda model are estimated in the same way that was reported in section 5.2.2. Firstly, it is assumed that the rock salt experiments the primary stage of the creep under a deviatoric stress equal to 10 MPa. From Fig. 5.5, Kelvin parameters are determined by considering the volumetric strains as negligible. The shear modulus G^K is calculated through Eq. 5-1, which considers a completely relaxed dashpot for a long time span, and the Kelvin viscosity is determined with Eq. 5-2, which results from solving the first order non-homogeneous differential Eq. (4) considering the initial condition $e^K_{1(t=0)} = 0$.

The parameters that define the viscoplastic yield surface (Eq. 4-14) were calculated considering the recommendations given by Sterpi and Gioda, 2007 (53). The parameters C^{vp} and ϕ^{vp} were not determined at the instantaneous failure of the salt, but estimated once the viscoplastic threshold was experimentally attained. In case of limited experimental data, they proposed a viscoplastic friction angle equal to the estimated angle at failure ($\phi^{vp} = \phi$) and a viscoplastic cohesion affected by a reduction factor, which in the previous chapter was 0.6 for the schist rock. For this soft sedimentary rock, the range values of 25 $^\circ$-35 $^\circ$ for friction angle reported by Afrouz, 1992 (63) were considered.

At this point, it is important to mention that the Mohr-Coulomb viscoplastic parameters need to be calibrated in order to activate the secondary creep phase at a deviatoric stress of 10 MPa ($F^{vp} = 0$) for the tests available. Since the elasto-viscoplastic model considers the dilation angle ψ^{vp}, the suggested value for an average quality rock is 1/8 of the friction angle according to Hoek and Brown (64). Both viscosity coefficient and dilation angle were calibrated through the viscoplastic strain rate expressed in Eq. 5-3.

Finally, parameters associated to the Sterpi and Gioda model that describe halite behavior are presented in Table 5.3.

Table 5.3: Mechanical parameters associated to the Sterpi and Gioda model for the halite rock.

	Elastic and visco-elastic parameters			
	B^e (MPa)	G^e (MPa)	η^K (MPa.d)	G^K (MPa)
	24286	7500	29228	5500
	Visco-plastic parameters			
Peal values	η^{vp} (MPa.d)	c^{vp} (MPa)	ϕ^{vp} ($^\circ$)	ψ^{vp} ($^\circ$)
Residual values	236	0.7	20	5

5.3.4 Numerical triaxial creep test on halite

The three triaxial creep tests on halite reported in the previous section have been reproduced in the threeÂ--dimensional finite difference code FLAC 3D by use of the Sterpi and Gioda model. Although the experimental tests were performed in specimens with a length/diameter ratio of 2, a square brick unit with a side length of 1 m (one single zone) has been adopted for modeling since boundary conditions are simplified, see Fig. 5.9. Normal displacements are restricted in all surfaces but the top one. The four faces that surround the bottom one are subjected to stress boundary conditions that consist of a constant confining stress of 10 MPa. The creep test starts once the axial stress is applied on the top of the model.

Fig. 5.10 presents a comparison of the results obtained with experimental tests and numerical simulations using the elasto-viscoplastic model. It is also shown the numerical results calculated with the double mechanism model by Firme, 2013 (5). The specific axial strain in the primary and secondary creep conditions determined by the Sterpi and Gioda model are in close agreement with the experimental results, even, in the tertiary creep phase. On the other hand, when using the double mechanism model which is restricted to instantaneous response connected to a secondary creep phase only, differences are observed, especially for the test with the major applied axial stress.

5.4 Sensitivity analysis

In this section, a study of sensitivity around the set of parameters which influence the elasto-viscoplastic response of the model is made. The influence of the parameters variation is characterized by the comparison of experimental and numerical results for the same time duration. As showed in the previous section, parameters associated to elasto-viscoplastic model of Sterpi and Gioda for halite rock specimens were determined; however, due to the lack of more experimental tests, it is necessary to make a study of sensitivity around the different possible values of the parameters.

Starting from the set of parameters of Table 5.3, the parameters vary one after the another. The parameters can be divided in three groups: the elastic, viscoelastic and viscoplastic parameters.

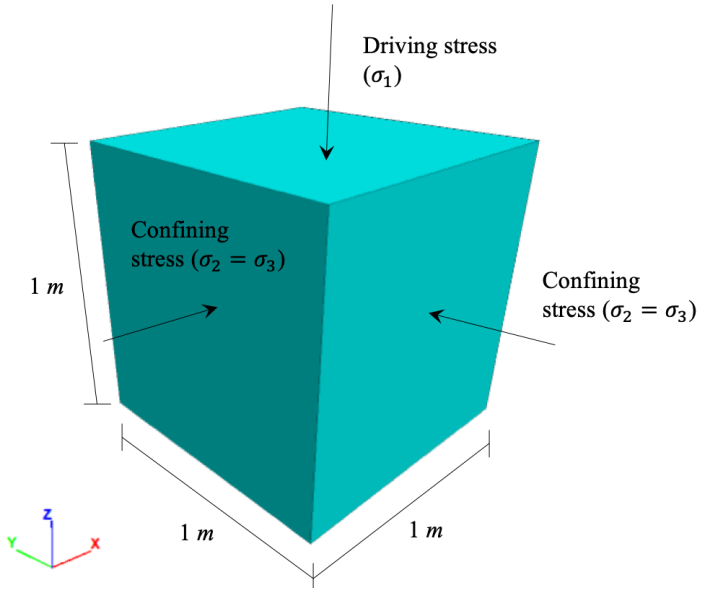

Figure 5.9: Numerical model of triaxial creep test on halite.

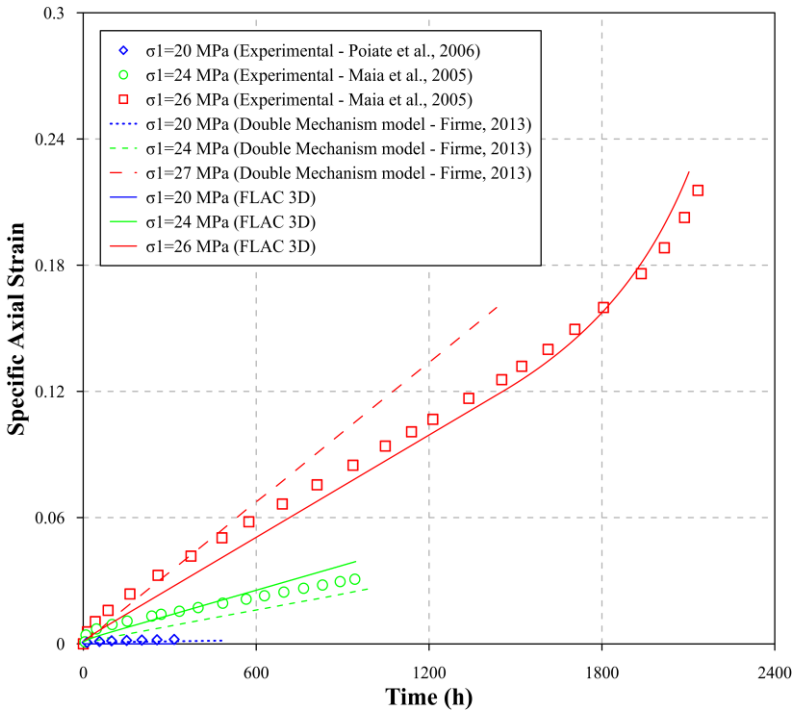

Figure 5.10: Comparison of experimental and numerical results considering the double mechanism and the Sterpi and Gioda models.

5.5 Influence of elastic parameters

In this part, the bulk and shear modulus influence the instantaneous strain developed by the halite rock sample. By observing the curves of axial strains vs time (Fig. 5.5, 5.7 and 5.8) in the experimental results of section 5.3.2, it is noted that elastic strains are much lower than creep strains, even for the other rock salt sample results. Therefore, for the stress state considered in the rock sample test, there will not be much more difference in terms of total strains or curve inclination.

5.6 Influence of viscoelastic parameters

The kelvin shear modulus and viscosity coefficient of kelvin correspond to the viscoelastic parameters, which contribute to the primary creep stage of the creep curve. In this stage, the viscoelastic strains increase over the time with a decreasing rate, thus leading to an asymptotic value of strains that depends on the value of the kelvin shear modulus. As can be observed in Fig. 5.11, it is plotted the experimental curves of three triaxial creep test on halite and the numerical curve when using the Sterpi and Gioda model with their associated parameters of Table 5.3 (Numerical result - 100% Gk).

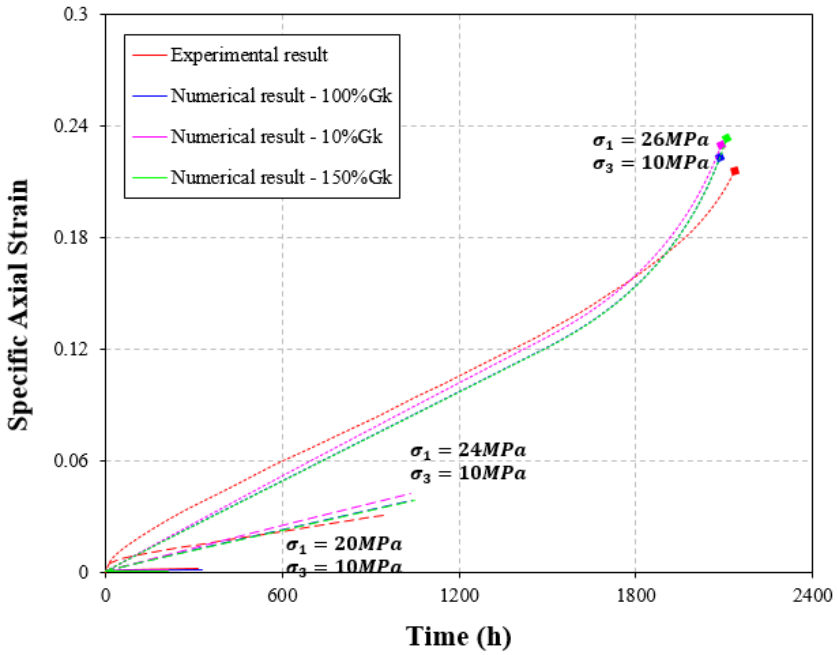

Figure 5.11: Influence of the kelvin shear modulus G^k by using the Sterpi and Gioda model.

Moreover, it is presented in Fig. 5.11 the numerical results when decreasing and increasing the kelvin shear modulus in 90% and 50%, respectively. According to this figure, the variations made in the kelvin shear modulus do not alter significantly the specific axial strain curve, even there is no difference for the numerical result that considers a 150% of the G^k when comparing with the original numerical curve presented (Numerical result - 100% Gk).

On the other hand, it is shown in Fig. 5.12 numerical curves for different

values of the viscosity coefficient of kelvin in reference with the value of Table 5.3 (Numerical result - 100% η^k) . Since the viscosity coefficient of kelvin influences on the decay of the viscoelastic strain rate, when reducing this parameter it is reproduced higher values of total axial strains in a determined time in comparison with the original numerical result (Numerical result - 100%). The higher the axial stress is, a more important difference will be noted.

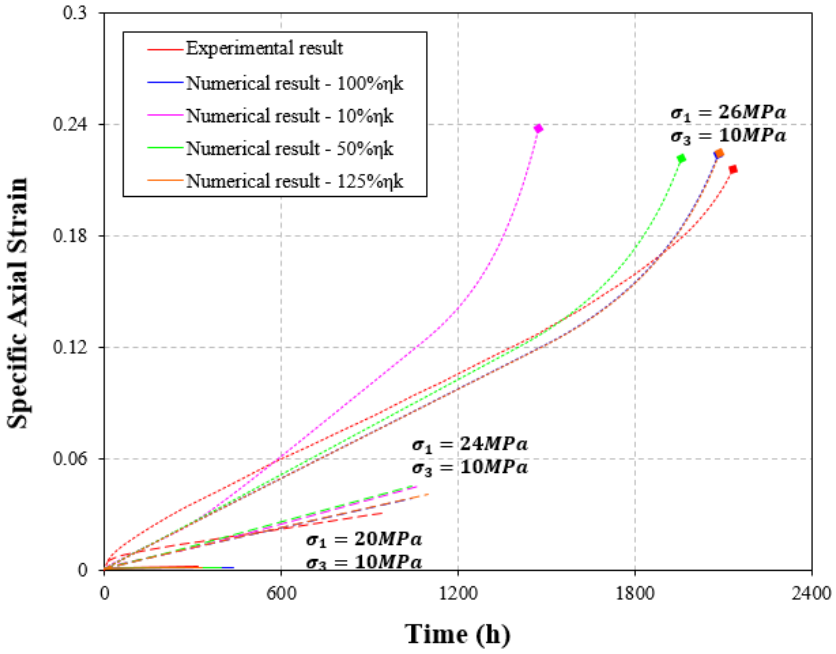

Figure 5.12: Influence of the viscosity coefficient of kelvin η^k by using the Sterpi and Gioda model.

5.7 Influence of viscoplastic parameters

Since the slope of the second stage of the curve (secondary creep) is defined by the viscoplastic viscosity coefficient η^{vp}, it is presented in Fig. 5.13 the influence of this parameter in the specific axial strain with time. As can be observed, secondary creep stage takes place in an early time, which is defined by the viscoplastic envelope $F^{vp} = 0$ that depends on the viscoplastic cohesion and friction angle ; therefore, it is more appreciable the differences reproduced when varying the viscoplastic viscosity coefficient. Then, it is shown in Fig. 5.13 that strain rate increases with the reduction of the viscoplastic viscosity coefficient, as expected. In addition, it is seen that tertiary creep takes place in an earlier time when this parameter is reduced.

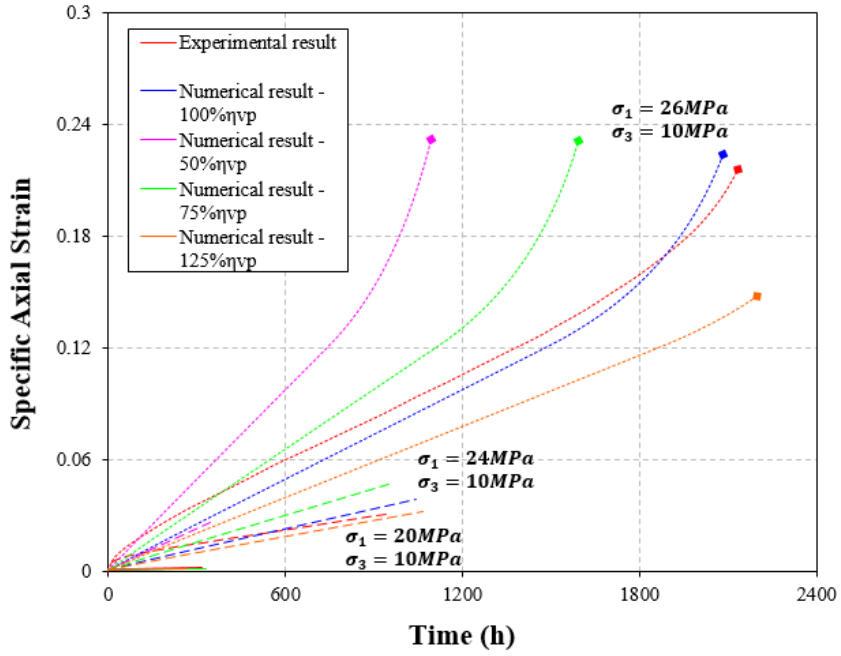

Figure 5.13: Influence of the viscoplastic viscosity coefficient η^{vp} by using the Sterpi and Gioda model.

6 Elasto-viscoplastic model application

6.1 Introduction

The implementation of the elasto-viscoplastic model has been verified through different experimental results in the last chapter, which gives us some confidence in simulating a tunneling and a wellbore closure problem in halite rock formation with the Sterpi and Gioda model. The first case of study introduces the application of Sterpi and Gioda model by simulating a tunneling problem in which deformations around the excavation are evaluated and compared with results provided in the literature. The second case of study has been presented by Gonçalves, 2011 (59) using the visco-elastic double mechanism model. This problem concerns the study of the gradual evolution of wellbore closure in a Brazilian offshore region of pure halite rock using the computer program Itasca – FLAC 3D finite volume solver. The excavation process in a wellbore of pure halite is simulated and the numerical results are compared with the obtained by Gonçalves, 2011 (59).

6.2 Tunneling problem

As a first case of application, a tunneling problem driven in a homogeneous rock mass subjected to an initial isotropic state of stress was evaluated. This application referred to a tunneling problem was also developed by Sterpi and Gioda, 2007 (53) and two analyses were performed. The first one is limited to a secondary creep stage (VP2) by using only peak values of the parameters for the viscoplastic unit and the second analysis involves the tertiary creep (VP3) that includes residual values of the parameters. Numerical results are focused in the tunnel face deformations over time and a comparison with Sterpi and Gioda, 2007 (53) work is executed.

6.2.1 Geotechnical consideration

The tunneling problem consists of a full face excavation of a circular tunnel at a rate of 6 m/day in a homogeneous and isotropic rock mass subjected to an isotropic state of stress $\sigma_0 = 10$ MPa. This corresponds to a tunnel depth of approximately 400m. The tunnel length and radius is 140 m and 4.5 m, respectively.

6.2.1.1 Mechanical parameters

By adopting the suggestion made by Hendron, 1968 (58) related to the reduction factor of 0.25 from laboratory elastic moduli to the field ones when the Rock Mass Rating (RMR) is equal to 48 (value considered for this rock in situ rock mass), and assuming the same reduction to the viscoelastic shear modulus and

remaining the viscoelastic viscosity coefficient unchanged (Sterpi and Gioda, 2007 (53)), parameters of the elastic and kelvin unit are the listed in Table 6.1.

The viscoplastic parameters of c^{vp} and ϕ^{vp} are determined in a similar way to the intact rock and even the reduction factor of $R_{CS} = 0.6$ remain unchanged. Furthermore, the unconfined compression strength of 7 MPa is the assigned according to the Hoek-Brown criterion (Sterpi and Gioda, 2007 (53)). A visualization of the determination of c^{vp} and ϕ^{vp} for the rock mass are presented in Fig. 5.2. For the viscoplastic viscosity coefficient, it is adopted the reduction factor already introduced for cohesion (Sterpi and Gioda, 2007 (53)). Therefore, the factor is calculated through the ratio of the cohesion for intact rock with the cohesion for rock mass, which is 0.147.

Table 6.1: Mechanical parameters referred to the in situ rock mass for the deep tunnel problem (Sterpi and Gioda, 2007 (53)).

	Elastic and visco-elastic parameters			
	B^e (MPa)	G^e (MPa)	η^K (MPa.d)	G^K (MPa)
	1470	678	49470	5848
	Visco-plastic parameters			
	η^{vp} (MPa.d)	c^{vp} (MPa)	ϕ^{vp} (°)	ψ^{vp} (°)
Peak values	706	1.16	32.3	14
Residual values	353	0	20	0

6.2.1.2 Three-dimensional analysis

Three-dimensional analyses were carried out to investigate the deformation developed in the tunnel section 20 m apart from the grid border. In this study, FLAC3D (Fast Lagrange Analysis of Continua in 3-dimensions), which is based on the finite volume method, was used for modeling. Due to the symmetry along the tunnel axis, a quarter of the ground is analyzed. Fig. 6.1 shows a 3D block model with the finite volume grid and relevant dimensions. The horizontal (x), longitudinal (y) and vertical (z) directions are 50, 140 and 50 m, respectively. It was employed a wedge type zone along the tunnel axis whereas hexahedral zones for the rest of the rock mass. Moreover, it was used 161280 zones to define the finite volume grid presented in Fig. 6.1.

The rock mass behavior is described with Sterpi and Gioda model through the mechanical parameters specified in Table 6.1. The length of the tunnel is divided into tunnel zones that are smaller in size once they are close to the control point that is located to 20 m from the border of the tunnel. There are three degrees of freedom describing displacements in each node of the solid element. Displacements in z direction are fixed at the bottom of the grid. In addition, no horizontal displacements are allowed on the x-z planes (i.e. y=0 and y=140) and y-z planes (i.e. x=0 and x=50). Since an approximated specific unit weight for schist rock is 26 kN/m ^{3}, it was applied at the top of the grid a load of 10 MPa.

The excavation process is modeled by gradually removing block zones inside the tunnel. Due to the fact that the excavation is at a rate of 6 m/day, a multistage excavation has been performed. A maximum timestep ($\triangle t_{max}^{cr}$) of 1e4 sec is taken into account for the analyses. This value is acceptable since an estimate for the maximum creep timestep for numerical accuracy may be calculated as the ratio of the material viscosity to the shear modulus according to Itasca - FLAC 3D, 2017.

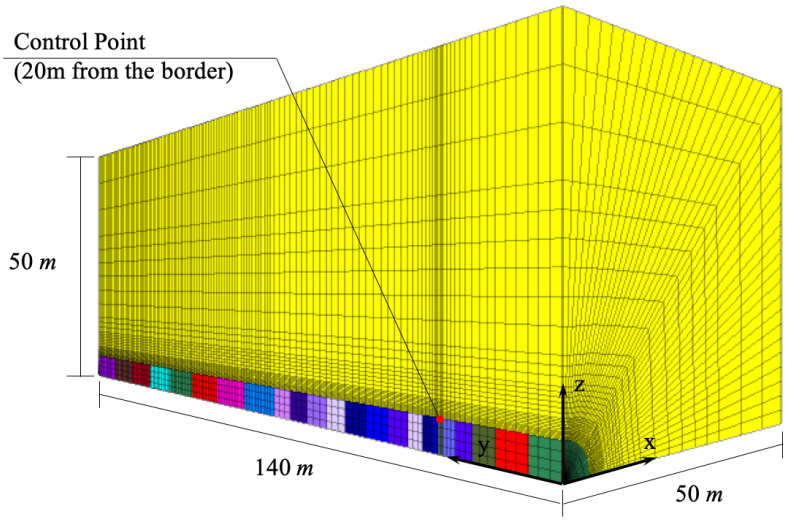

Figure 6.1: 3D block model with the finite volume grid for the tunneling problem.

6.2.2 Numerical results and comparison

Total displacements contours evolution over time for the first analysis (VP2), which is limited to the secondary creep stage, is presented in Fig. 6.2. As expected, major displacements are accumulated at the beginning of the tunnel during the excavation process. Sections of Fig. 6.2 (a), (b), (c), (d), (e) and (f) are reached by the tunnel face at a time t=0.83, 1.66, 3.3, 6.7, 11.7 and 23.3 days, respectively. Approximately, the maximum total displacement observed is 0.07 m, which is located in the tunnel face.

In Fig. 6.3 the final x and z displacements are observed when t=23.3 days (end of the excavation) for the VP2 analysis. In the case of the z displacements, a greater part of the rock mass is involved in comparison with the x displacements since these are concentrated closer to the tunnel.

Fig. 6.4 shows vertical stress distribution of the rock mass during the tunnel excavation for analysis VP2. Fig. 6.4 (a) represents the initial stress condition, which is an isotropic state of stress $\sigma_0 = 10$ MPa, Fig. 6.4 (b) shows the vertical stress condition at a time t=11.7 days, and Fig. 6.4 (c) the same after completion of the tunnel excavation. It is seen that the vertical stresses at the crown of the tunnel decreases due to the tunnel excavation and increases at some distance from the tunnel boundary, especially at the bottom of the model (middle horizontal plane of the tunnel).

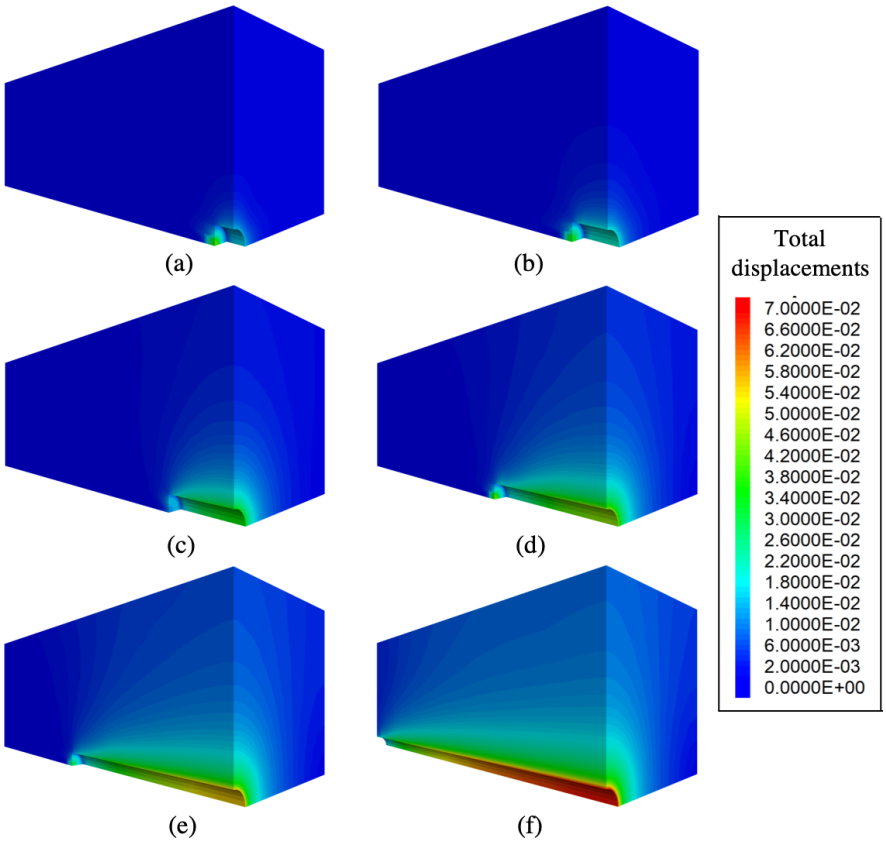

Figure 6.2: Total displacements in meters for (a) 5 m, (b) 10 m, (c) 20 m, (d) 40 m,(e) 70 m and (f) 140 m of tunnel excavation (VP2).

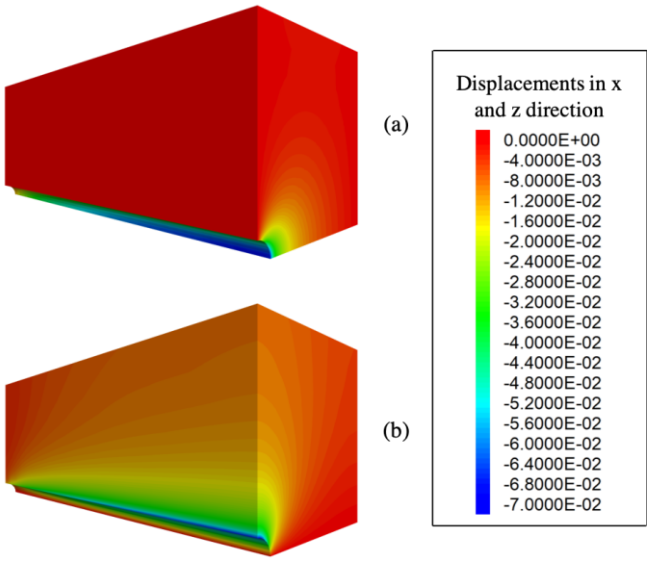

Figure 6.3: Displacements in meters at the end of the excavation process (t=23.3 days) in (a) x and (b) z direction (VP2).

Numerical results for the second analysis (VP3), which involves the tertiary creep by including residual values of the viscoplastic parameters, are presented up to a time t=11.7 $days$, i.e., 70 m of tunnel excavation (half tunnel excavation). Total displacements for this analysis are presented in Fig. 6.5. At a time t=11.7

$days$, it is observed in VP3 analysis major maximum displacement (0.085 m) than in the first analysis (VP2), since in the last one it is obtained a value of 0.057 m. Similarly to the first analysis, maximum displacements are located in the tunnel face.

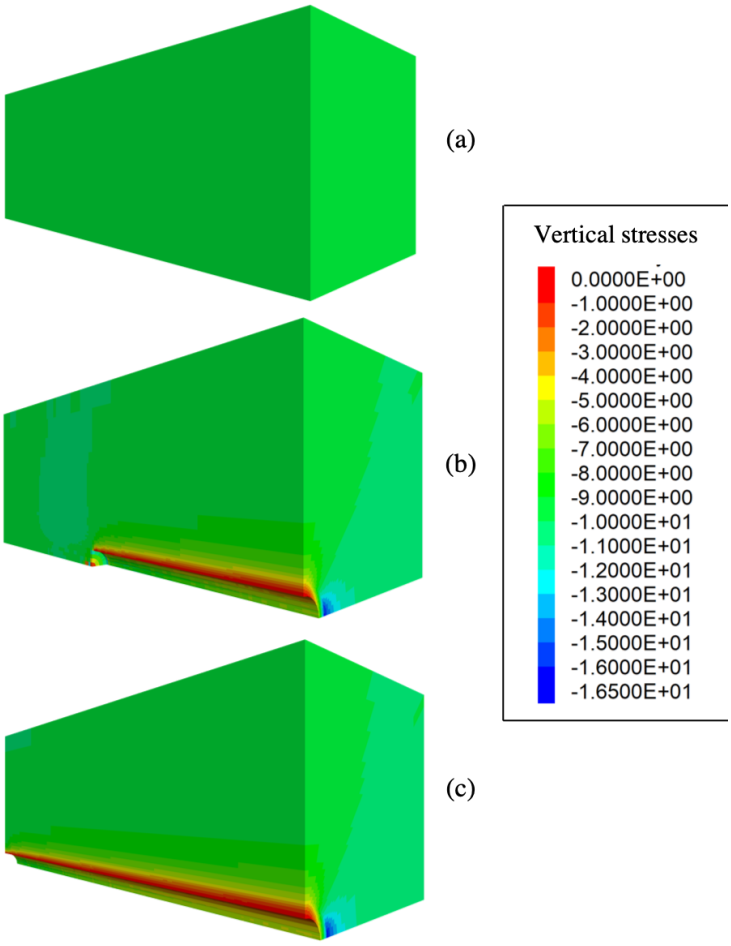

Figure 6.4: Vertical stress (MPa) distribution (a) Initial condition, (b) during excavation and (c) end of the excavation (VP2).

In Fig. 6.6 displacements in x,y and z direction are observed at a time t=11.7 $days$ for the VP3 analysis. It has been reported a x-displacement of 0.082 m and a z-displacement of 0.084 m located in the tunnel face, in contrast with the y-displacement of approximately 0.033 m that occurs at the end face of the excavation.

On the other hand, since this analysis is capable of reproducing tertiary creep, Fig. 6.7 shows the square of the second invariant of deviatoric visco-plastic strains obtained at the final evaluated time t=11.7 $days$. As can be observed, it is attained a maximum value of 0.028 on the wall of the tunnel. Moreover, the concentration of visco-plastic strains reaches up to 2.3 m out of the tunnel in the rock mass.

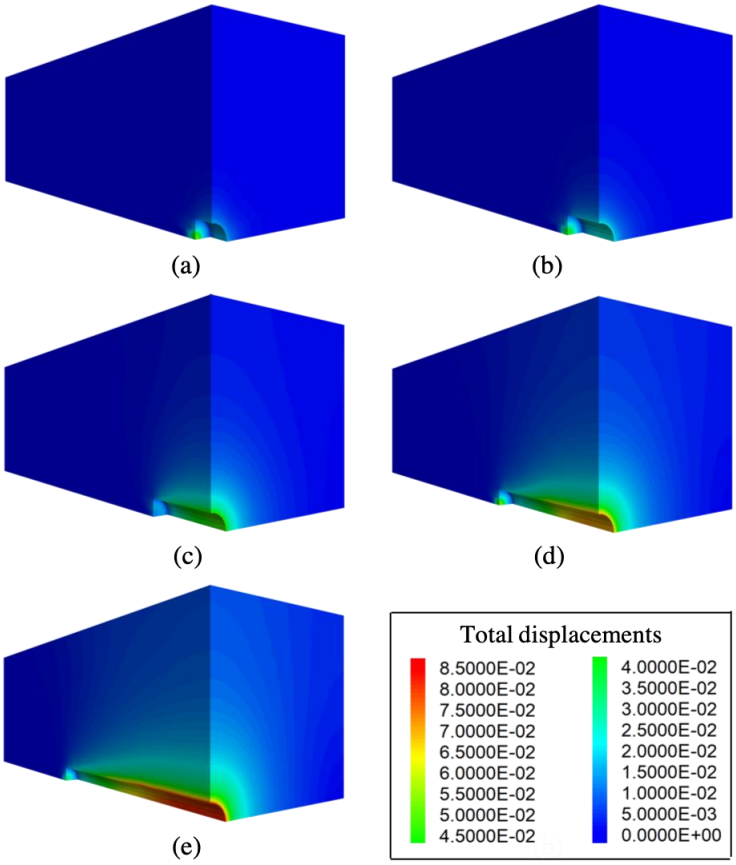

Figure 6.5: Total displacements in meters for (a) 5 m, (b) 10 m, (c) 20 m, (d) 40 m and (e) 70 m of tunnel excavation (VP3).

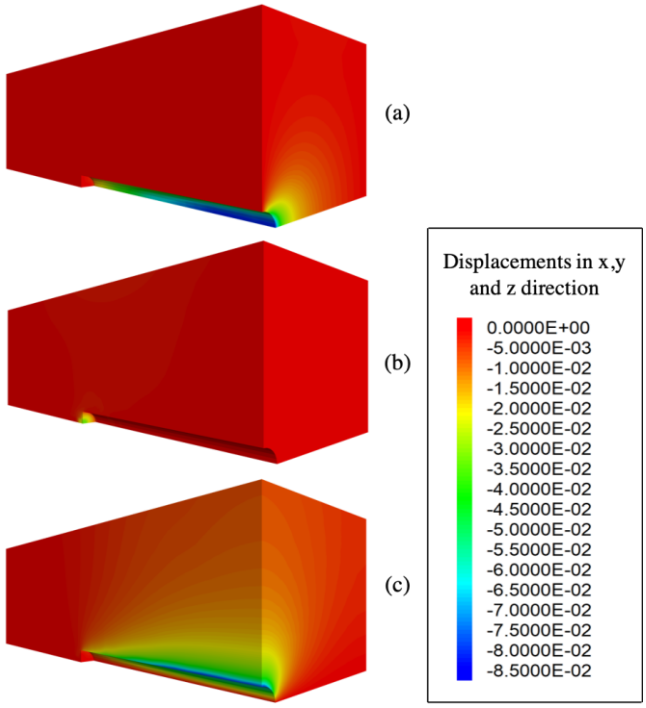

Figure 6.6: Displacements in meters at a time t=11.7 days (a) x, (b) y and (z) direction (VP3).

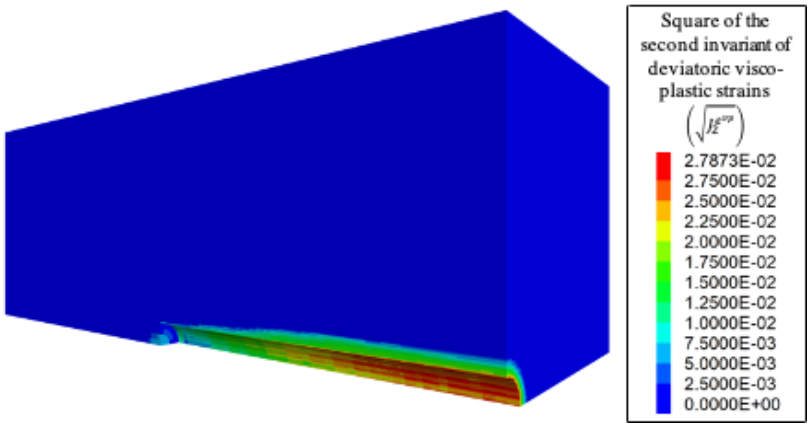

Figure 6.7: Square of the second invariant of deviatoric visco-plastic strains contours at a time t=11.7 days (VP3).

Results in Fig. 6.8 refer to the normalized vertical displacement over time of a tunnel section located 20 m apart from the grid border (control point specified in Fig. 6.1). The reason for this choice, from one hand, relies on the fact that it limits the boundary effects at the chosen section and, from the other hand, allows for a sufficient excavation length (and time) behind the grid border to observe the full development of visco-plastic effects (Sterpi and Gioda, 2007 (53))). Results of a finite element code (Sterpi and Gioda, 2007 (53)) and FLAC 3D by use of Sterpi and Gioda model are in close agreement although there is a discrepancy in the VP2 analysis during time t=4 and 10 days.

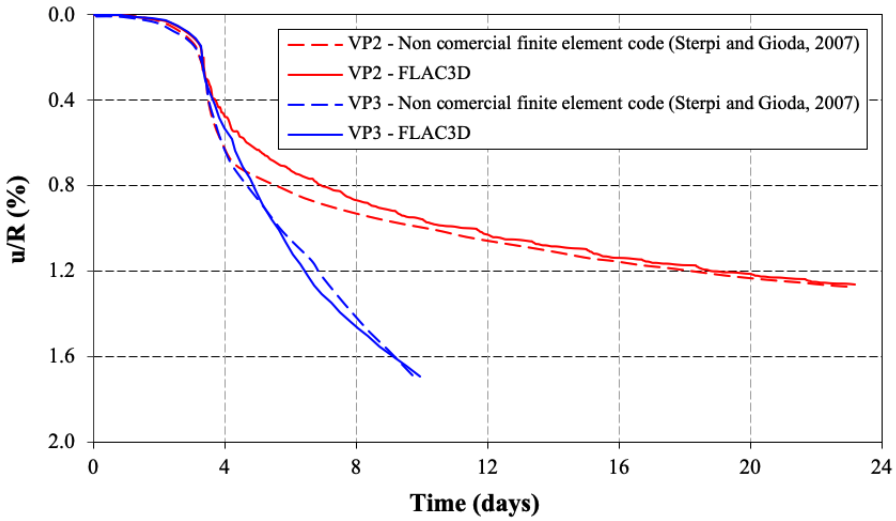

Figure 6.8: Tunnel closure with time results of a finite element code (Sterpi and Gioda, 2007 (53)) and FLAC 3D by use of Sterpi and Gioda model (VP3).

In reference with the maximum tunnel closure, the approximated value of u/R=1.5% indicates that major squeezing problems such as large tunnel closures

and high pressures exerted by the rock mass on the heading support should not be involved; however, it should be considered that the value reported corresponds to a radial convergence of about 7 cm, which could be larger than the gap existing between a possible tunnel boring machine and the perimeter of excavation (Sterpi and Gioda, 2007 (53)).

6.3 Wellbore closure analysis

Before 1990 in Brazil, it was difficult to describe rock salt behavior under high differential stresses causing stuck pipe and casing, drilling costs and even loss of wells. Campos Basin is one of the most active offshore regions in the world, currently providing some of the greatest challenges in scope and opportunity for the oil industry; nevertheless, the complex salt tectonics and the extreme water and reservoir depths require not only high development costs, but also innovative technology to bring these fields on stream (Maia et al., 2005 (60)).

The evolution of a wellbore closure in a Brazilian offshore region of halite rock formation has been studied using FLAC 3D, the finite difference analysis commercial program. Two cases were investigated (cases A and B) in the numerical analysis, which were presented by Gonçalves, 2011 (59). It is considered a 100 m-thick rock salt of pure halite layer located at different depths (Table 6.2). The unit weights were considered 10 kN/m^3 for the water, 22.56 kN/m^3 for the post-salt layer and 21.60 kN/m^3 for the halite. The well was drilled with a diameter of 0.155 m using a drilling mud of unit weight equal to 11.75 kN/m^3.

Figure 6.9 schematically illustrates the models in the typical stratification of the Brazilian pre-salt, demonstrating the representativeness of the analyzes.

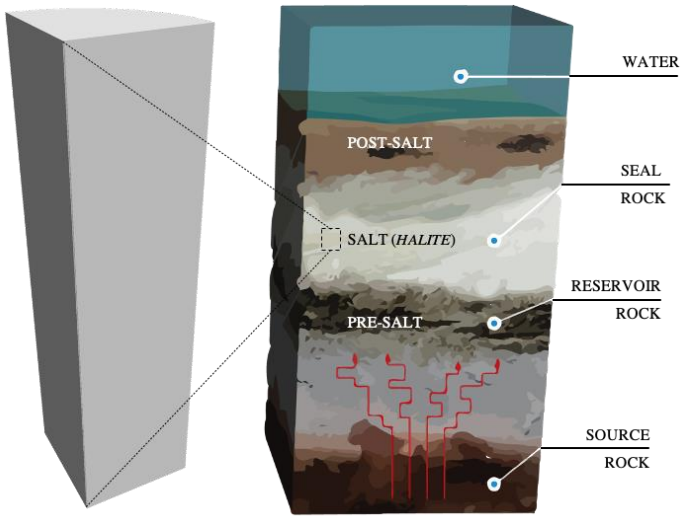

Figure 6.9: Overview of the wellbore in the typical stratification of the Brazilian pre-salt (adapted from Christante, 2009 61=).

Table 6.2: Lithologies for case A and B.

Layer	Case A	Case B
Water	750 m	1125 m
Overburden	1000 m	1750 m
Halite	100 m	100 m

6.3.1 Numerical analysis

With the identified parameters associated to the constitutive model of Sterpi and Gioda in section 5.3.3 (Table 5.3), it was applied the constitutive equation in the numerical simulation of the creep salt behavior to predict the evolution of wellbore closure with time for case A and B. Moreover, the evaporite zone of the chosen scenario for the study is a thick pure halite layer to be drilled as an instantaneous and multistage drilling procedure.

6.3.1.1 Numerical model

The 3D numerical model for both cases consists of a quarter cylinder with 25 m of radius and considers the well situated along its longitudinal axis. This lateral boundary is far enough from the borehole to avoid boundary effects (Gravina, 1997 (1), Firme, 2013 (5)). The region was discretized into 47,600 zones (hexahedron and wedge), with a greater refinement around the borehole (Fig. 6.10). Furthermore, the represented lithology simulated was divided into 10 layers of 10 m thick, totaling 100 m. This division aims to make drilling in stages feasible, considering the typical drilling for rock salt at a rate of 10 m/h. The input parameters of the Sterpi and Gioda model are given in Table 5.3.

6.3.1.2 Boundary condition

In the 3D models, non-displacement conditions are imposed at the outer boundary (edges of the models away from the well) along the radial direction, see Fig. 6.10). Moreover, normal displacements are restricted on the x-z plane (i.e. y=0) and y-z plane (i.e. x=0) at the boundaries of the grid. For z-direction, displacements are not allowed at the bottom of the grid. In case of the top boundary configuration of the model, restricted vertical displacements are assumed since some Brazilian authors (Costa, op. cit.; Poiate Jr, op. cit.; Gonçalves, op. cit.; Firme, op. cit.) adopt this configuration for geomechanical analyses due to the fact that the numerical model represents a part of the rock mass; therefore, the top of the model makes reference to the overlying lithology.

In addition, on the upper model boundary, a load equivalent to the sum of the sea water and post salt layer load is applied which represents the overburden load at the top of the model.

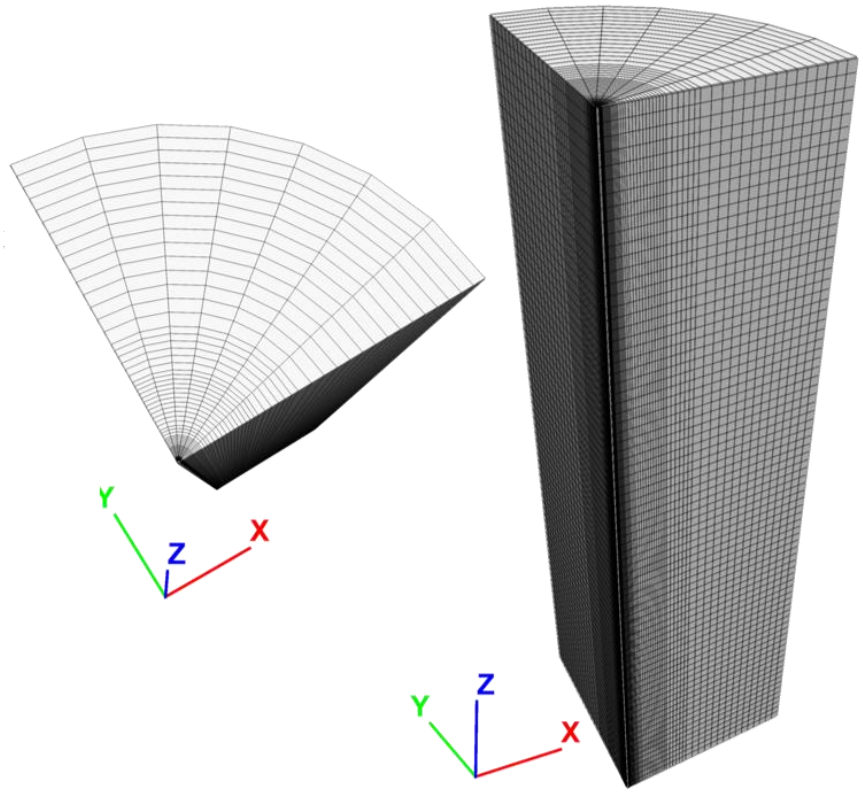

Figure 6.10: Finite difference grid discretization of the numerical model for both cases of study.

6.3.1.3 Initial condition

In the geomechanical model, gravitational loads define the in situ stress field condition before any disturbance. It is assumed sea water with a unit weight of 10 kN/m^3 and a lithology overlying the salt with 22.56 kN/m^3 of unit weight; i.e. post-salt, in a homogeneous condition in terms of mechanical properties.

By considering no compaction effect in the halite layer of 21.60 kN/m^3 of unit weight, vertical stress at any point in the formation is equivalent to the accumulated weight of the formation materials above. Since salt layer does not account with the presence of pore pressure, effective and total stresses are equals, (Firme, 2013 (5)). Moreover, the initial stress at field is assumed to be isotropic (i.e. $\sigma_{xx} = \sigma_{yy} = \sigma_{zz}$).

In Fig. 6.11 are presented the initial stress state in x,y and z-direction for case A and B.

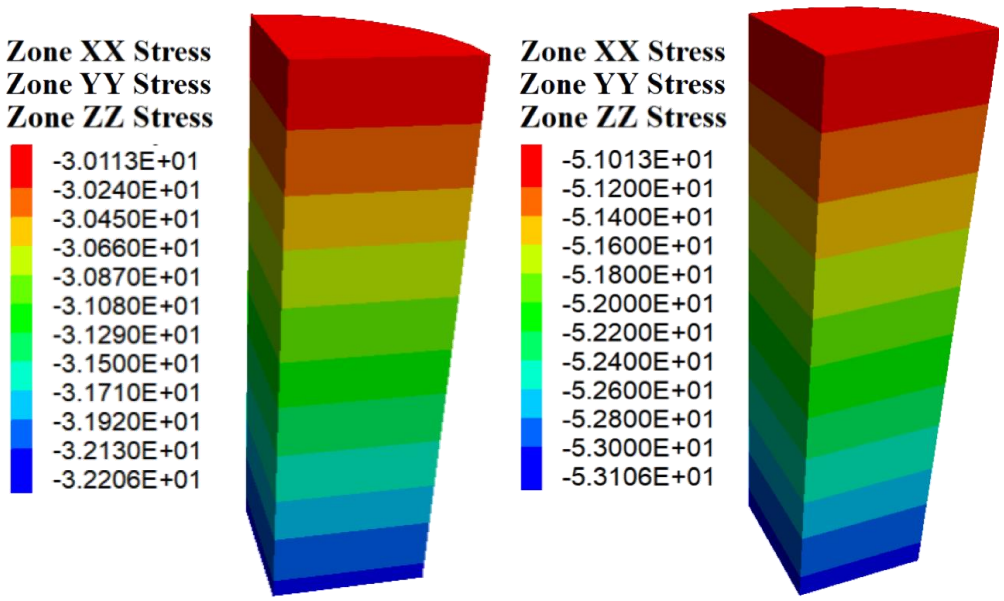

Figure 6.11: Initial conditions (total stresses in MPa) for: (a) case A and (b) case B.

6.3.2 Numerical results and discussion

The numerical simulations involve the study of wellbore closure for both cases of study (case A and B), for both single stage and multistage of drilling. Firstly, for the multistage of drilling, the procedure velocity depends on the type of rocks; therefore, it is adopted the value of 10 m/s, proposal provided by Costa et al., 2011 (65) for rock salt. Secondly, in order to simulate numerically the geomechanical problem in the most realistic condition, a group of zones is removed simulating the drilling section at each drilling step. There are 10 group sections to be drilled for the case A and B models. Finally, the unit weigh of the drilling mud, equivalent to 11.75 kN/m^3, imposes a pressure on the internal borehole wall that varies linearly along the wall. Moreover, it is important to mention that it was necessary to use a volume difference grid with a good level of discretization, in order to adequately represent the instantaneous response in the wall of the borehole.

Once the drilling process was simulated by deactivating zones that represent the removed material and applying the pressure due to the drilling mud on the well wall, the instantaneous elastic displacements for cases A and B within a radial distance of 4 m are sketched in Fig. 6.12 and 6.13.

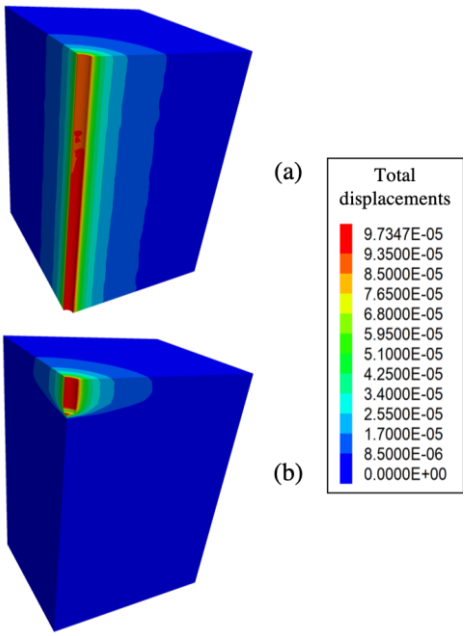

Figure 6.12: At t = 0, instantaneous displacements (m) for case A in a region of radius 4 m: (a) single stage of drilling and (b) multistage of drilling.

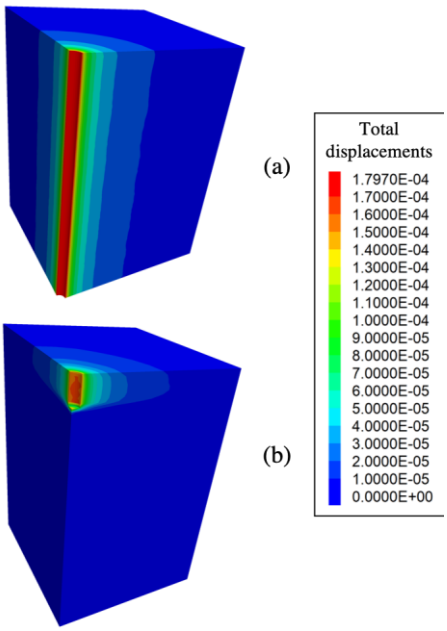

Figure 6.13: At t = 0, instantaneous displacements (m) for case B in a region of radius 4 m: (a) single stage of drilling and (b) multistage of drilling.

It was shown that the maximum instantaneous elastic displacements presented in the wall of the borehole for cases A and B are 0.000097 m and 0.000180 m, respectively. For both cases, displacements developed when drilling in a single stage or multistage are equal; however, close to the base of the drilled section, the differences are observed.

Fig. 6.14 presents the distribution of Von Mises stress within the simulated region. It can be noticed that the maximum Von Mises stress always occurs in the

wellbore wall at t=0. Besides, similarly to the instantaneous elastic displacements results, differences between a single stage and multistage of drilling are only observed on the base of the drilled zone.

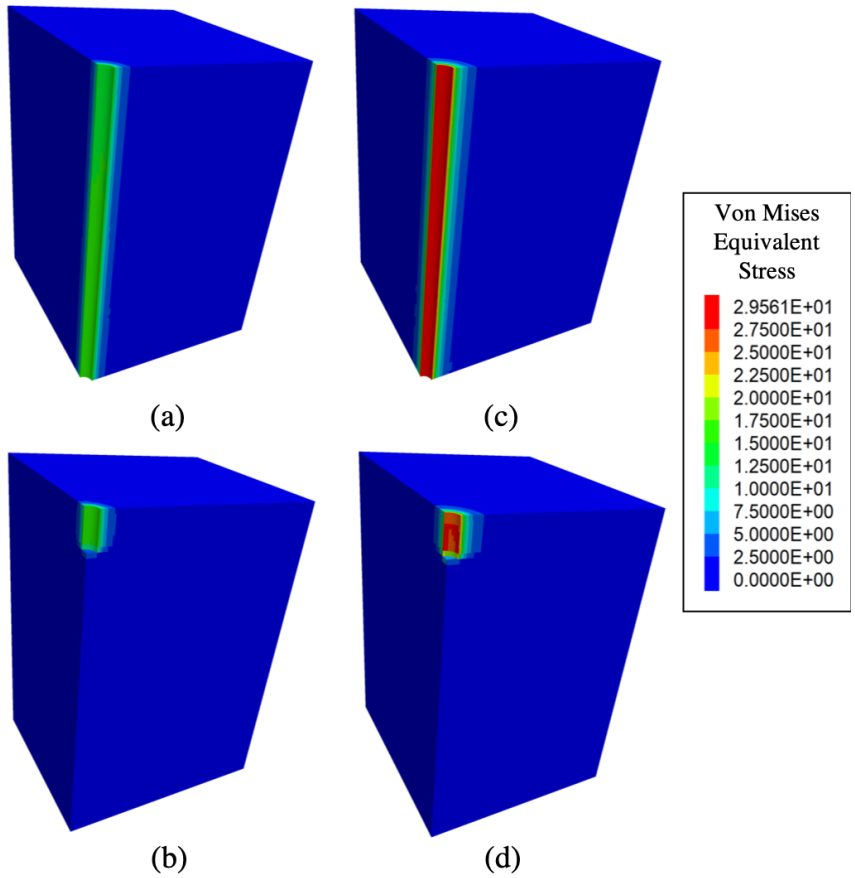

Figure 6.14: At t = 0, Von Mises equivalent stress (MPa) for the elastic response in a region of radius 4 m: (a) single stage of drilling (Case A), (b) multistage of drilling (Case A), (c) single stage of drilling (Case B) and (d) multistage of drilling (Case B)

Fig. 6.15 shows the tangential and radial stresses along line AB at time t = 0 for both cases, obtained through numerical and analytical solutions. It can be observed that in case A, the stresses return to their initial condition in a shorter distance from the wellbore when compared to the stresses for case B.

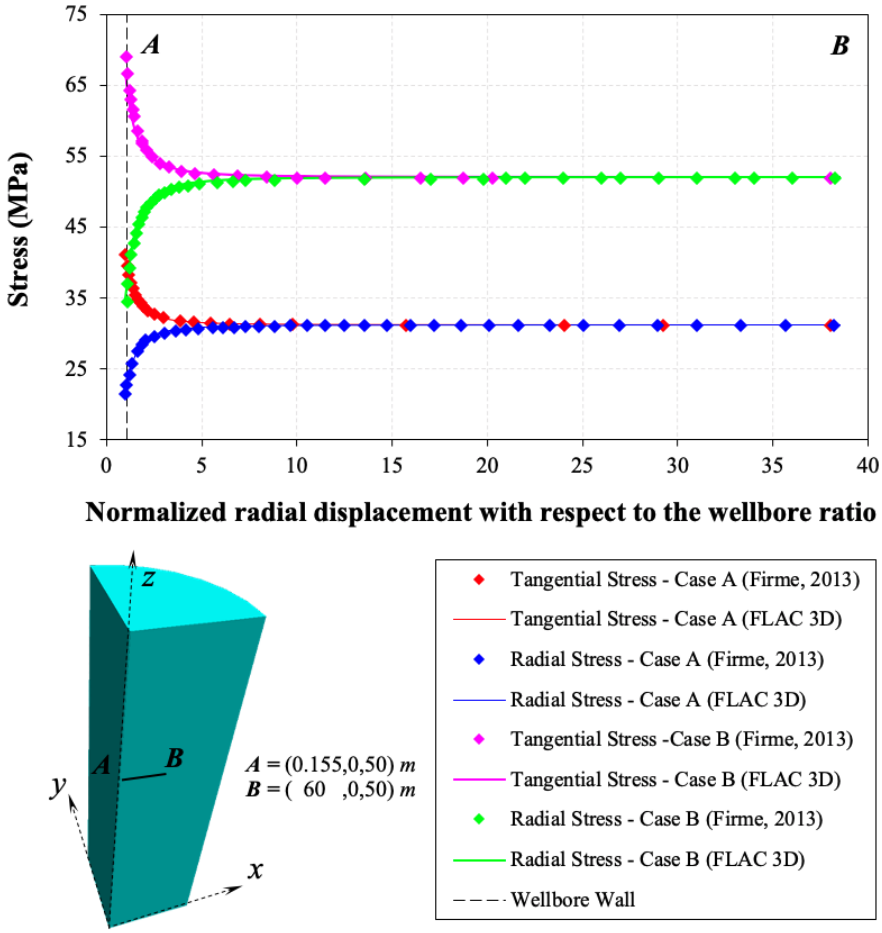

Figure 6.15: Instantaneous stresses (t=0) along line AB for cases A and B (single stage of drilling).

Once the initial response is achieved, the creep behavior in the halite is activated and the evolution of the radial closure is tracked over time in the two wells. A maximum timestep ($\triangle t_{max}^{cr}$) of 2.5e3 sec is taken into account for both cases of study. This value is acceptable since an estimate for the maximum creep timestep for numerical accuracy may be calculated as the ratio of the material viscosity to the shear modulus according to Itasca - FLAC 3D, 2017.

In Fig. 6.16, it is presented the wellbore total displacements evolution in meters for case A within a region of radius equal to 4 m by considering a single stage of drilling. It is shown total displacements at a time t= 0 h, 10 h, 100 h, 200 h and 480 h. It is observed that in the first 10 h after drilling procedure finishes, minimum displacements are developed at the lower side of the borehole wall; however, when observing displacements after 100 h, a considerable variation of total displacement are generated. The final maximum total displacement achieved at t=480 h is 0.000257 m.

Similarly, Fig. 6.17 illustrates the wellbore total displacements evolution in meters for case B within a region of radius equal to 4 m by considering a single stage of drilling at a time t= 0 h, 10 h, 100 h, 200 h and 480 h. There is no appreciable evolution of displacements within the first 10 hours after the drilling

process finished. At a time of 100 hours, displacements become larger as time goes on. Moreover, it is attained a maximum total displacement of 0.000470 m.

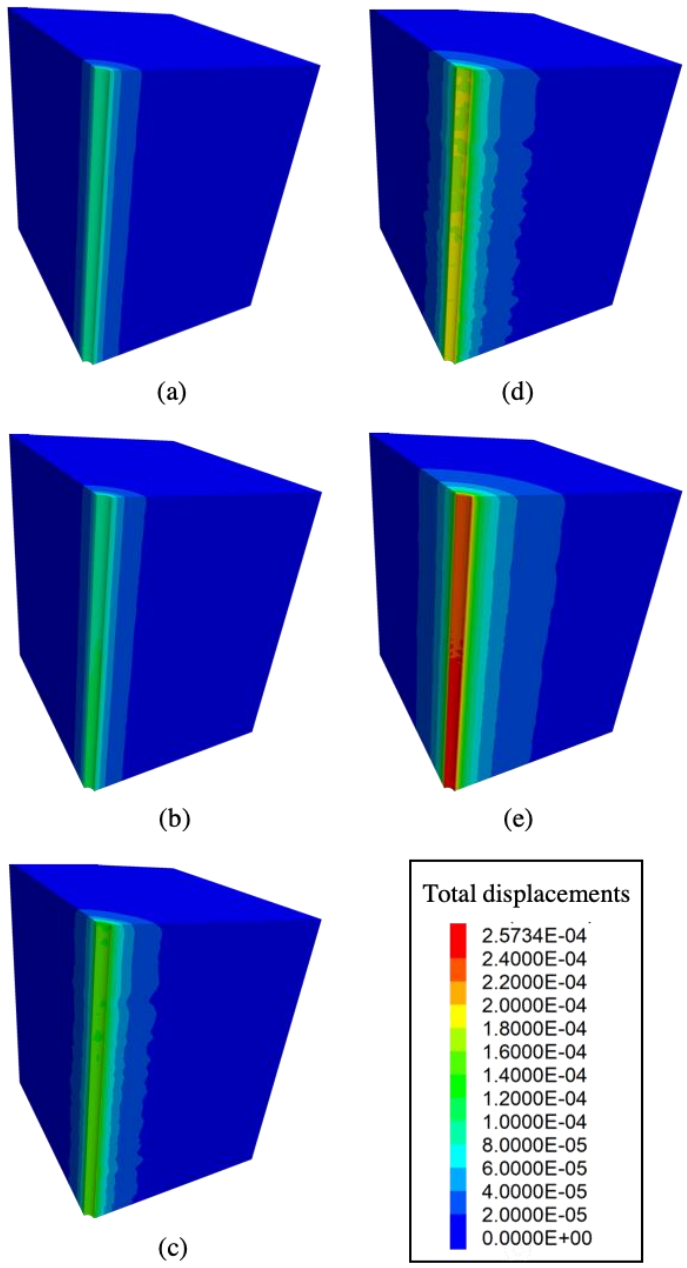

Figure 6.16: Wellbore total displacements (m) evolution for case A (single stage of drilling) within a region of radius 4 m: (a) t=0 h, (b) t=10 h, (c) t=100 h, (d) t=200 h and (e) t=480 h.

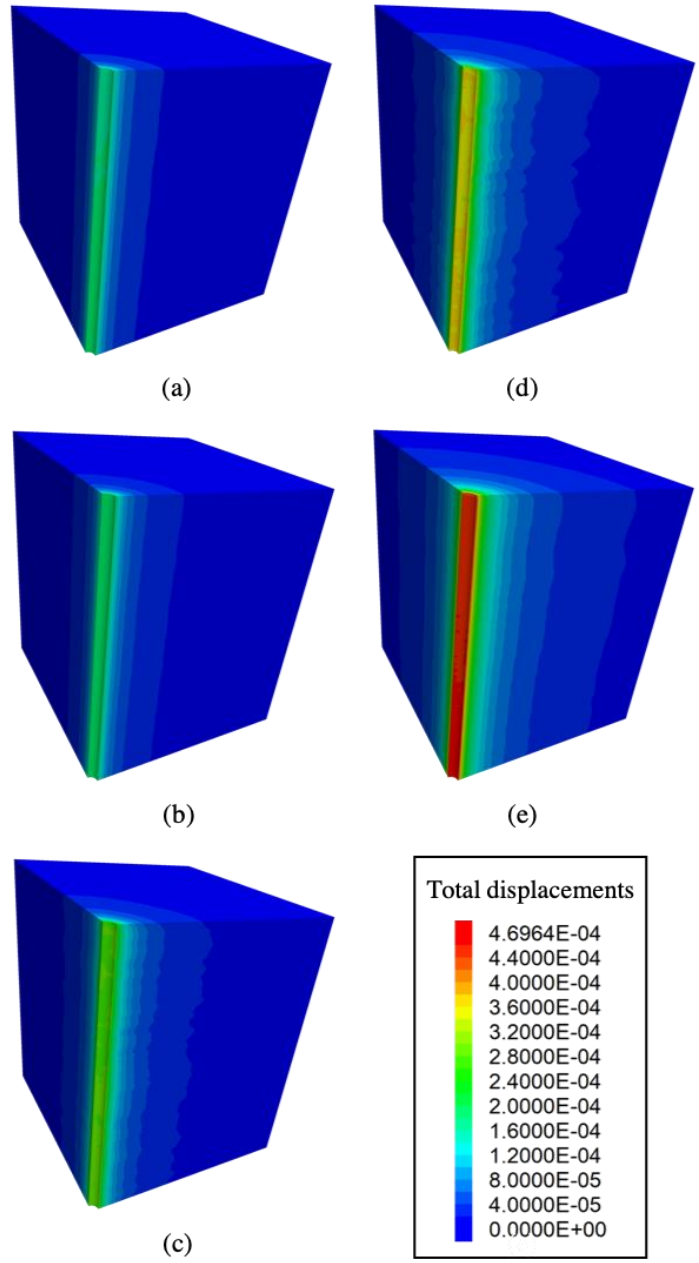

Figure 6.17: Wellbore total displacements (m) evolution for case B (single stage of drilling) within a region of radius 4 m: (a) t=0 h, (b) t=10 h, (c) t=100 h, (d) t=200 h and (e) t=480 h.

Fig. 6.18 and 6.19 show the distribution of Von Mises stress within the 4m of the simulated region for cases A and B, respectively. It is observed that the maximum Von Mises stress always occurs in the wellbore wall, but its value declines in the first 100 hours after the drilling process and increases after that time.

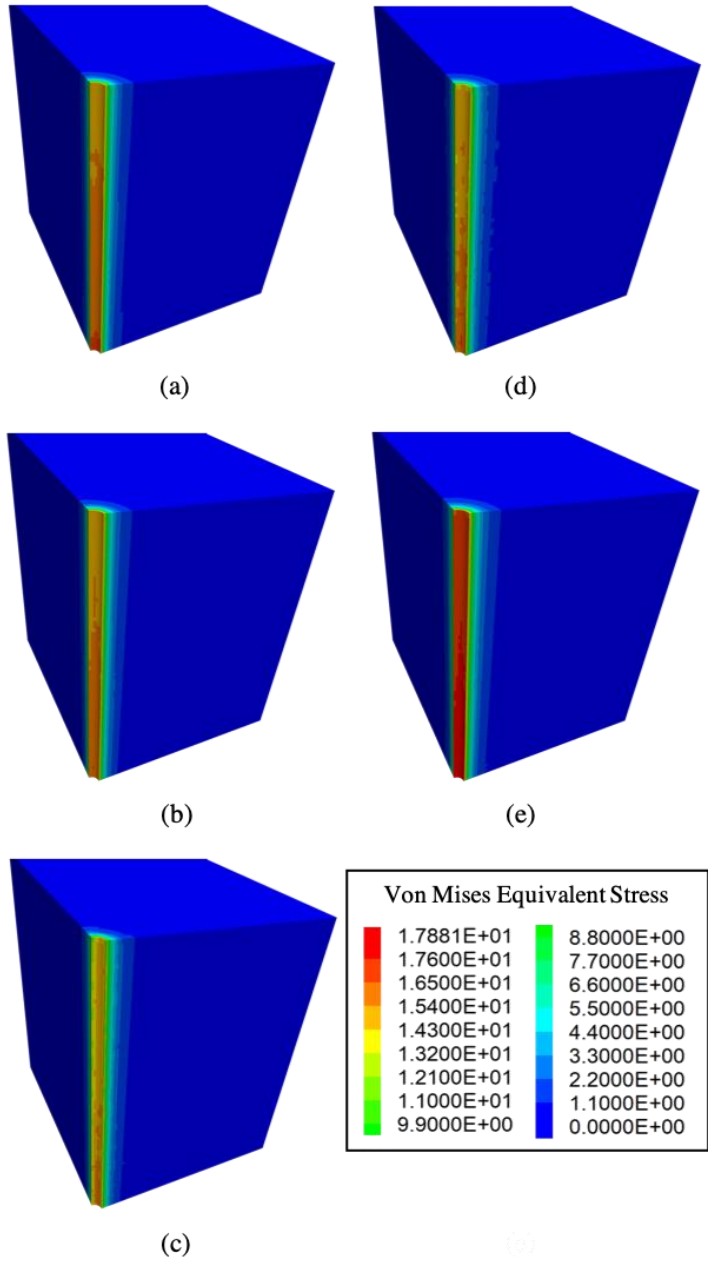

Figure 6.18: Von Mises Equivalent Stress (MPa) evolution for case A (single stage of drilling) within a region of radius 4 m: (a) t=0 h, (b) t=10 h, (c) t=100 h, (d) t=200 h and (e) t=480 h.

Furthermore, Fig. 6.20 presents, for case A, the wellbore final displacements at time t = 480 h within a radial distance of 4 h when performing a single and a 10-stage of drilling procedure. The largest radial closure displacement corresponds to 85 % of the displacement computed when considering a single drilling procedure. Only primary creep strains were observed in case A.

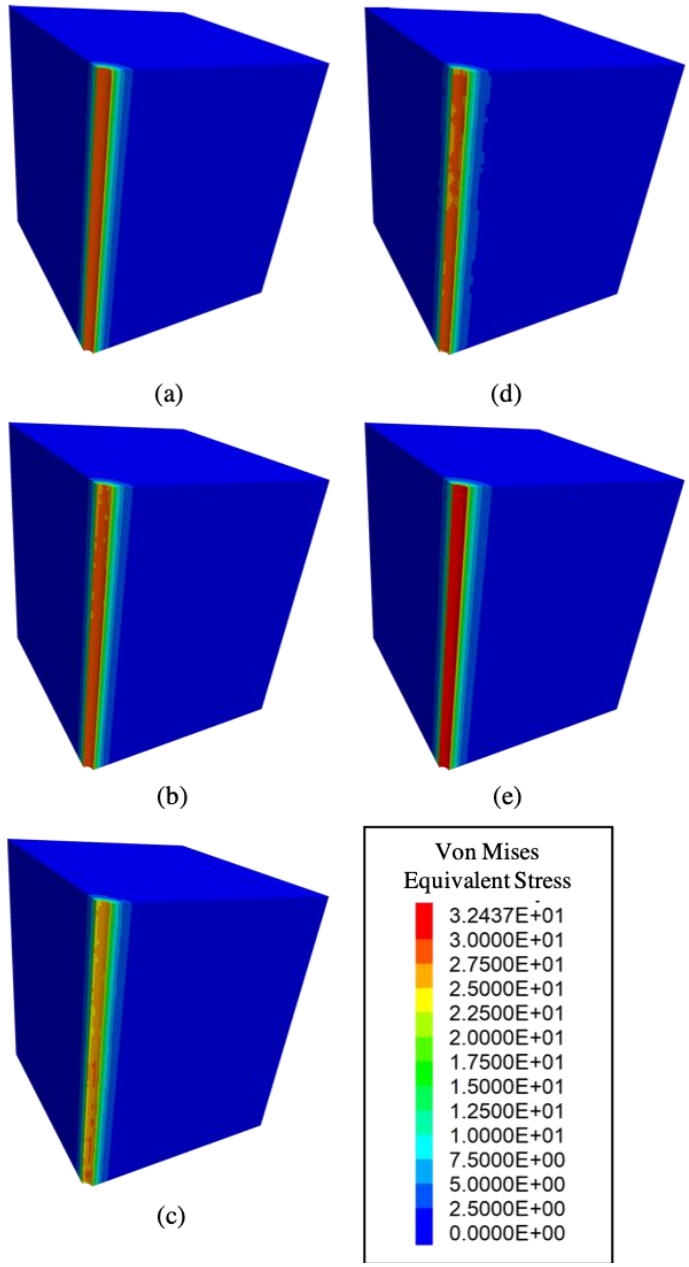

Figure 6.19: Von Mises Equivalent Stress (MPa) evolution for case B (single stage of drilling) within a region of radius 4 m: (a) t=0 h, (b) t=10 h, (c) t=100 h, (d) t=200 h and (e) t=480 h.

Similarly, wellbore displacements for case B at time t = 480 h are illustrated in Fig. 6.21. Again, the largest radial closure displacement obtained with 10 stages of drilling is about 88% of the maximum displacement determined in a single step. Primary creep strains were computed for the multi-step of drilling procedure while primary and secondary creep strains occurred when the wellbore was simulated as a single step.

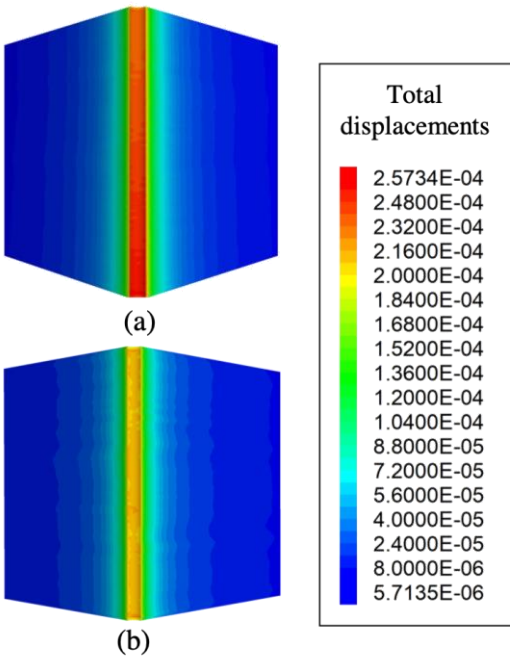

Figure 6.20: Wellbore total displacements (m) for case A at t = 480 h for a region of radius 4 m: (a) single stage and (b) 10 stages of drilling with rate of 10 m/s.

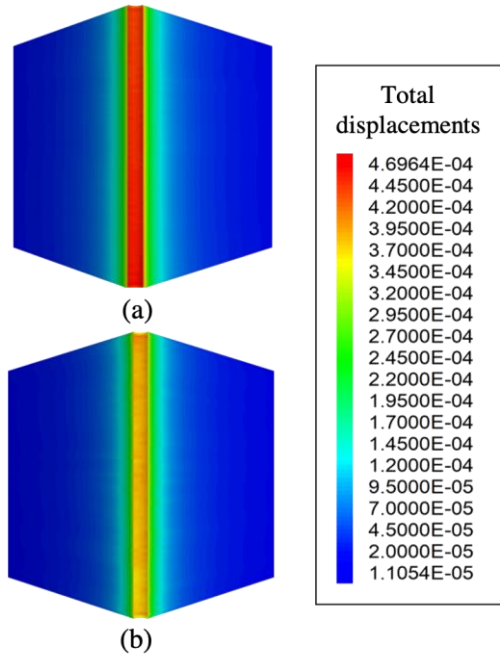

Figure 6.21: Wellbore total displacements (m) for case B at t = 480 h for a region of radius 4 m: (a) single stage and (b) 10 stages of drilling with rate of 10 m/s.

Finally, in Fig. 6.22, it is presented the radial closure evolution in time computed with the elasto-viscoplastic model implemented in FLAC 3D and the visco-elastic double mechanism model (Gonçalves, 2011 (59)) for cases A and B when performing a single stage of drilling procedure. The creep curves refer to the displacement on the wellbore wall at a point located in the middle of the salt rock layer in order to avoid influence from the upper and lower boundaries. It may be observed that although instantaneous radial displacements are equal to the values calculated with the double mechanism model, both curves exhibit significant discrepancy in the creep response stage. Such differences are more pronounced when the evaporitic rock is subjected to a lower overburden (case A).

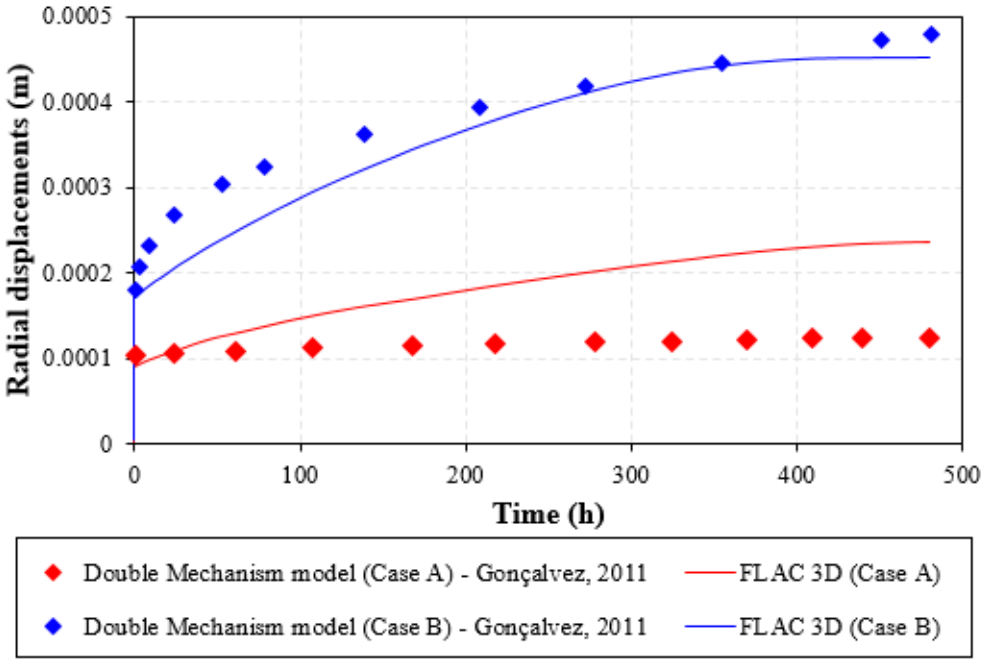

Figure 6.22: Wellbore total displacements (m) for case A at t = 480 h for a region of radius 4 m: (a) single stage and (b) 10 stages of drilling with rate of 10 m/s.

Since the transient creep is not accounted for by the double mechanism model, the steady-state creep is coupled directly to the initial elastic strain. The creep curve (strain vs. time) remains lagged, although good fittings for the steady-state creep rate (curve inclination) can be often obtained. However, whenever early creep deformation estimates are needed, the contribution of transient creep is relevant: for instance, early-stage creep prediction to monitor pre-salt borehole closure, once a minimum diameter to allow casing running and minimum cement sheath thickness are mandatory. In salt caverns for hydrocarbon storage or waste disposal, the medium tightness is a key property, and comprehensive creep modeling is fundamental to forecast stress states prone to cause damage by dilatancy. These aforementioned situations clearly show the importance of applying a more powerful constitutive model for predicting the time-dependent behavior of salt rocks, such as the elasto-viscoplastic model used in this work.

7 Conclusions and recommendations

An elasto-viscoplastic model has been implemented in the finite volume code Itasca-FLAC 3D in order to predict and analyze the wellbore closure in evaporitic rocks. It was employed the Forward Euler explicit algorithm for the integration of the constitutive equations varying in time and written in C++ programming language in order to generate a dynamic link library (DLL). The constitutive model consists of an instantaneous response defined by the Hooke's law, a viscoelastic Kelvin unit accounting for primary creep and a viscoplastic Bingham model, in which the frictional component is governed by the Mohr Coulomb yield condition with a non-associated flow rule, accounting for secondary creep. Furthermore, the elasto-viscoplastic model adopts a softening behavior by variating viscoplastic parameters from their peak to their residual values, which guarantees the tertiary creep. The implementation procedure has been validated by comparing a group of experimental uniaxial creep tests with the computed ones by using the Sterpi and Gioda model. On the other hand, parameters that define the elasto-viscoplastic model of halite samples have been estimated with help of triaxial creep test results in order to carry out a numerical analysis that studies the time-dependent behavior of a wellbore on halite formation considering a single and multistage of drilling procedure.

7.1 Conclusions

The following main conclusions have been accomplished in the present dissertation.

(a) The adopted explicit integration scheme is based on the numerical algorithm presented by Itasca, which considered the theory of plasticity. Despite this fact, the adopted integration scheme was modified in order to take into account Perzyna's theory, which allowed to conclude that the adaptation of the algorithm and the implementation of the model were accomplished successfully.

(b) Considering that FLAC 3D relies on a discretization approach where the grid is conformed by constant strain-rate elements a fine discretization was needed in order to obtain acceptable results. Moreover, the mixed discretization technique allowed to obtain smooth results regarding displacements after a finer discretization was applied near the area of study.

(c) The implementation of the elasto-viscoplastic model has been verified for

different problems (uniaxial creep test on schist and tunneling problem) giving some confidence in simulating a wellbore closure problem in halite rock formation with the Sterpi and Gioda model.

(d) This study has shown that numerical and experimental results on halite samples under different stress levels matched with a good approximation once the material parameters were determined and calibrated. The importance and the difficulty of an accurate calibration of the rheological model parameters is a great concern, since in situ creep tests are seldom performed and the interpretation of data from monitored works is often difficult.

(e) Furthermore, the results obtained by numerical simulations to predict the evolution of the well closure with time, when performing a 10-stage drilling procedure, generated lower displacements than a single stage of excavation.

(f) Regarding the comparison between radial displacements computed with the elasto-viscoplastic and the double mechanism models, the observed differences can be attributed to the limited performance of the double mechanism model whenever early creep deformation estimates are needed.

(g) Numerical analysis incorporating the elasto-viscoplastic model Sterpi and Gioda (2007) can be a powerful tool for geotechnical engineers in engineering projects involving rocks with a time-dependent mechanical behavior.

7.2 Suggestions for further investigations

Further research are needed and some questions remain to be specified for the study of the time-dependent behavior of evaporites in relation to wellbore stability.

(a) Further triaxial creep test on halite are needed in order to confirm the parameters that define the elastoviscoplastic model.

(b) Additional scenarios of wellbore where the formation of evaporite is more realistic and contribution of the tertiary creep is involved need to be studied by use of the Sterpi and Gioda model.

(c) A longer term behavior of halite rock (few years) is still an open question and needs to be studied by means of laboratory tests, in situ measurements and numerical analyses.

(d) Different global salt structures such as gallery or cavern can be analyzed in order to measure Sterpi and Gioda model capability.

Bibliography

[1] GRAVINA, C. C.. **Simulação numérica do comportamento mecânico do sal em poços de petróleo**, 1997.

[2] TOMANOVIC, Z.. **Rheological model of soft rock creep based on the tests on marl**. Mechanics of Time-Dependent Materials, 10(2):135– 154, 2006.

[3] FAHIMIFAR, A.; KARAMI, M. ; FAHIMIFAR, A.. **Modifications to an elasto-visco-plastic constitutive model for prediction of creep deformation of rock samples**. Soils and Foundations, 55(6):1364–1371, 2015.

[4] BOTELHO, F.. **Análise numérica do comportamento mecânico do sal em poços de petróleo**. Master's thesis, Department of Civil Engineering—Pontifícia Universidade Católica de Rio de Janeiro, 2008.

[5] POIATE JR, E.. **Mecânica das rochas e mecânica computacional para projeto de poços de petróleo em zonas de sal**. PhD thesis, Department of Civil Engineering—Pontifícia Universidade Católica de Rio de Janeiro, 2012.

[6] FIRME, P.. **Constitutive modeling and probabilistic analysis applied to wells in salt zones**. Master's thesis, Department of Civil Engineering—Pontifícia Universidade Católica de Rio de Janeiro, 2013.

[7] HUNSCHE, U.; HAMPEL, A.. **Rock salt—the mechanical properties of the host rock material for a radioactive waste repository**. Engineering geology, 52(3-4):271–291, 1999.

[8] WEEKS, L. G.. **Habitat of Oil**. American Association of Petroleum Geologists, 1958.

[9] KHALEDI, K.. **Constitutive modeling of rock salt with application to energy storage caverns**. 2018.

[10] HEARD, H. C.. **Steady-state flow in polycrystalline halite at pressure of 2 kilobars**. Flow and fracture of rocks, 16:191–209, 1972.

[11] MUNSON, D. E.. **Preliminary deformation-mechanism map for salt (with application to wipp)**. Technical report, Sandia Labs., 1979.

[12] JEREMIC, M. L.. **Rock mechanics in salt mining**. CRC Press, 1994.

[13] WAWERSIK, W. R.; HANNUM, D. W.. **Mechanical behavior of New Mexico rock salt in triaxial compression up to 200 c**. Journal of Geophysical Research: Solid Earth, 85(B2):891–900, 1980.

[14] MATEI, A.; CRISTESCU, N.. **The effect of volumetric strain on elastic parameters for rock salt**. Mechanics of Cohesive-frictional Materials: An International Journal on Experiments, Modelling and Computation of Materials and Structures, 5(2):113–124, 2000.

[15] HANSEN, F.; MELLEGARD, K. ; SENSENY, P.. **Elasticity and strength of ten natural rock salts, the mechanical behavior of salt**. In: PROC. OF THE FIRST CONFERENCE, HARDY, H. R. JR. AND LANGER, M.(EDS.), volumen 53, p. 70, 1984.

[16] HÖFER, K.; THOMA, K.. **Triaxial tests on salt rocks**. In: INTERNATIONAL JOURNAL OF ROCK MECHANICS AND MINING SCIENCES & GEOMECHANICS ABSTRACTS, volumen 5, p. 195–196. Elsevier, 1968.

[17] SRIAPAI, T.; WALSRI, C. ; FUENKAJORN, K.. **Effect of temperature on compressive and tensile strengths of salt**. ScienceAsia, 38(2):166– 174, 2012.

[18] VAN SAMBEEK, L. L.; RATIGAN, J. L. ; HANSEN, F. D.. **Dilatancy of rock salt in laboratory tests**. In: INTERNATIONAL JOURNAL OF ROCK MECHANICS AND MINING SCIENCES & GEOMECHANICS ABSTRACTS, volumen 30, p. 735–738. Elsevier, 1993.

[19] THOMAS, J. E.. **Fundamentos de engenharia de petróleo**. Interciência, 2001.

[20] MILANI, E. J.; BRANDÃO, J.; ZALÁN, P.; GAMBOA, L.. **Petróleo na margem continental brasileira: geologia, exploração, resultados e perspectivas**. Revista Brasileira de Geofísica, 18(3):352–396, 2000.

[21] DUSSEAULT, M.. **Analysis of borehole stability**. In: INTERNATIONAL CONFERENCE ON COMPUTER METHODS AND ADVANCES IN GEOME- CHANICS, p. 125–137, 1994.

[22] XU, G.. **Wellbore stability in geomechanics**. PhD thesis, University of Nottingham, 2007.

[23] FARMER, P.; MILLER, D.; PIEPRZAK, A.; RUTLEDGE, J. ; WOODS, R.. **Exploring the subsalt**. Oilfield Review, 8(1):50–64, 1996.

[24] AMER, A.; DEARING, H.; JONES, R.; SERGIACOMO, M. ; OTHERS. **Drilling through salt formations: A drilling fluids review**. In: SPE DEEPWATER DRILLING AND COMPLETIONS CONFERENCE. Society of Petroleum Engineers, 2016.

[25] GAMBOA, L.; MACHADO, M.; DA SILVEIRA, D.; DE FREITAS, J.; DA SILVA, S.. **Sal: Geologia e tectônica, exemplos nas basicas brasileiras**. 2008.

[26] GIAMBASTIANI, M.. **Comportamento dependente do tempo de rochas sulfáticas de anidrita e gipso**. PhD thesis, Universidade de São Paulo, 2005.

[27] BELTRÃO, R.; SOMBRA, C.; LAGE, A.; FAGUNDES NETTO, J.; HENRIQUES, C.. **Challenges and new technologies for the development of the pre-salt cluster, santos basin, brazil**. In: OFFSHORE TECHNOLOGY CONFERENCE, volumen 4, 2009.

[28] CHEATHAM JR, J.; MCEVER, J. ; OTHERS. **Behavior of casing subjected to salt loading**. Journal of Petroleum Technology, 16(09):1– 069, 1964.

[29] HUDSON, J. A.; HARRISON, J. P.. **Engineering rock mechanics: an introduction to the principles**. Elsevier, 2000.

[30] HAGROS, A.; JOHANSSON, E. ; HUDSON, J. A.. **Time dependency in the mechanical properties of crystalline rocks. a literature survey**. Technical report, Posiva Oy, 2008.

[31] JAEGER, J. C.; COOK, N. G. ; ZIMMERMAN, R.. **Fundamentals of rock mechanics**. John Wiley & Sons, 2007.

[32] GHOSH ROY, M.; RAO, K.. **Analysis of creep behaviour of soft rocks in tunneling**. 2015.

[33] PENG, S.; PODNIEKS, E.. **Relaxation and the behavior of failed rock**. In: INTERNATIONAL JOURNAL OF ROCK MECHANICS AND MINING SCIENCES & GEOMECHANICS ABSTRACTS, volumen 9, p. 699– 700. Elsevier, 1972.

[34] PENG, S.. **Time-dependent aspects of rock behavior as measured by a servocontrolled hydraulic testing machine**. In: INTERNATIONAL JOURNAL OF ROCK MECHANICS AND MINING SCIENCES & GEOMECHANICS ABSTRACTS, volumen 10, p. 235–246. Elsevier, 1973.

[35] PARASKEVOPOULOU, C.; PERRAS, M.; DIEDERICHS, M.; AMANN, F.; LÖW, S.; LAM, T.; JENSEN, M.. **The three stages of stress relaxation-observations for the time-dependent behaviour of brittle rocks based on laboratory testing**. Engineering geology, 216:56–75, 2017.

[36] GIODA, G.. **A finite element solution of non-linear creep problems in rocks**. International Journal of Rock Mechanics and Mining Sciences & Geomechanics, 18(1):35–46, 1981.

[37] XU, T.; ZHOU, G.; HEAP, M. J.; YANG, S.; KONIETZKY, H. ; BAUD, P.. **The modeling of time-dependent deformation and fracturing of brittle rocks under varying confining and pore pressures**. Rock Mechanics and Rock Engineering, 51(10):3241–3263, 2018.

[38] PHIENWEJ, N.; THAKUR, P. ; CORDING, E.. **Time-dependent response of tunnels considering creep effect**. International Journal of Geomechanics, 7(4):296–306, 2007.

[39] OBERT, L.. **Creep in mine pillars: Report of investigation**. Rep, 6703, 1965.

[40] SINGH, D.. **A study of creep of rocks**. In: INTERNATIONAL JOURNAL OF ROCK MECHANICS AND MINING SCIENCES & GEOMECHANICS ABSTRACTS, volumen 12, p. 271–276. Elsevier, 1975.

[41] DE ORELLANA, A. C.. **Pressure solution creep and non-associated plasticity in the mechanical behaviour of potash mine openings**. In: INTERNATIONAL JOURNAL OF ROCK MECHANICS AND MINING SCIENCES & GEOMECHANICS ABSTRACTS, volumen 33, p. 347–370. Elsevier, 1996.

[42] SEMPLE, R. M.; HENDRON, A.; MESRI, G.. **Effect of time-dependent properties of altered rock on tunnel support requirements.** Dep of Transp, Fed Railroad Adm, Final Rep FRA-ORDD-74-30, 1973.

[43] FEBRES-CORDERO, E.; MESRI, G.. **Influence of testing conditions on creep behaviour of clay**. Technical report, 1974.

[44] MESRI, G.; FEBRES-CORDERO, E.; SHIELDS, D. ; CASTRO, A.. **Shear stress-strain-time behaviour of clays**. Geotechnique, 31(4):537–552, 1981.

[45] LIN, H.; WANG, C.. **Stress-strain-time function of clay**. Journal of Geotechnical and Geoenvironmental Engineering, 124(4):289–296, 1998.

[46] DUSSEAULT, M. B.; ROTHENBURG, L.; MRAZ, D. Z. ; OTHERS. **The design of openings in saltrock using a multiple mechanism viscoplastic law**. In: THE 28TH US SYMPOSIUM ON ROCK MECHANICS (USRMS). American Rock Mechanics Association, 1987.

[47] FIRME, P. A.; BRANDAO, N. B.; ROEHL, D.; ROMANEL, C.. **Enhanced double-mechanism creep laws for salt rocks**. Acta Geotechnica, 13(6):1329–1340, 2018.

[48] HUDSON, J.. **Comprehensive rock engineering, principals, practice and projects, volume 3, rock testing and site characterization**. Ed. Pergamon Press. Oxford, 1993.

[49] KAISER, P. K.. **Time-dependent behaviour of tunnels in jointed rock masses**. 1979.

[50] LIINGAARD, M.; AUGUSTESEN, A. ; LADE, P. V.. **Characterization of models for time-dependent behaviour of soils**. volumen 4, p. 157–177. American Society of Civil Engineers, 2004.

[51] HASHIGUCHI, K.; OKAYASU, T.. **Time-dependent elastoplastic constitutive equation based on the subloading surface model and its application to soils**. Soils and Foundations, 40(4):19–36, 2000.

[52] PERZYNA, P.. **The constitutive equations for rate sensitive plastic materials**. Quarterly of applied mathematics, 20(4):321–332, 1963.

[53] STERPI, D.; GIODA, G.. **Visco-plastic behaviour around advancing tunnels in squeezing rock**. Rock Mechanics and Rock Engineering, 42(2):319–339, 2007.

[54] GIODA, G.; CIVIDINI, A.. **Numerical methods for the analysis of tunnel performance in squeezing rocks**. Rock mechanics and rock engineering, 29(4):171–193, 1996.

[55] PERZYNA, P.. **Fundamental problems in viscoplasticity**. In: ADVANCES IN APPLIED MECHANICS, volumen 9, p. 243–377. Elsevier, 1966.

[56] MARTI, J.; CUNDALL, P.. **Mixed discretization procedure for accurate modelling of plastic collapse**. International Journal for Numerical and Analytical Methods in Geomechanics, 6(1):129–139, 1982.

[57] CRISTESCU, N.; HUNSCHE, U.. **Time effects in rock mechanics**, volumen 350. Wiley New York, 1998.

[58] HENDRON, A.. **Mechanical properties of rock**. Rock mechanics in engineering practice, p. 21–53, 1968.

[59] GONÇALVES, G. D. G.. **Parametric study of the influence of temperature in the thermomechanical analysis during salt rock excavation**, 2011.

[60] MAIA, C.; POIATE, J.; FALCAO, J.; COELHO, L.; OTHERS. **Triaxial creep tests in salt applied in drilling through thick salt layers in campos basin-brazil**. In: SPE/IADC DRILLING CONFERENCE. Society of Petroleum Engineers, 2005.

[61] CHRISTANTE, L.. **Pré-sal: desafios científicos e ambientais**. Unespciência. São Paulo, (3), 2009.

[62] POIATE JR, E.; MAIA, A.; FALCAO, J. L. ; OTHERS. **Well design for drilling through thick evaporite layers**. In: IADC/SPE DRILLING CONFERENCE. Society of Petroleum Engineers, 2006.

[63] AFROUZ, A.. **Practical handbook of rock mass classification systems and modes of ground failure**. CRC Press, 1992.

[64] HOEK, E.; BROWN, E. T.. **Practical estimates of rock mass strength**. International journal of rock mechanics and mining sciences, 34(8):1165– 1186, 1997.

[65] COSTA, A.; POIATE, E.; AMARAL, C.; PEREIRA, A.; MARTHA, L.; GAT- TASS, M.; ROEHL, D.. **Geomechanics applied to the well design through salt layers in brazil: A history of success**. In: MULTI- SCALE AND MULTIPHYSICS PROCESSES IN GEOMECHANICS, p. 165–168. Springer, 2011.